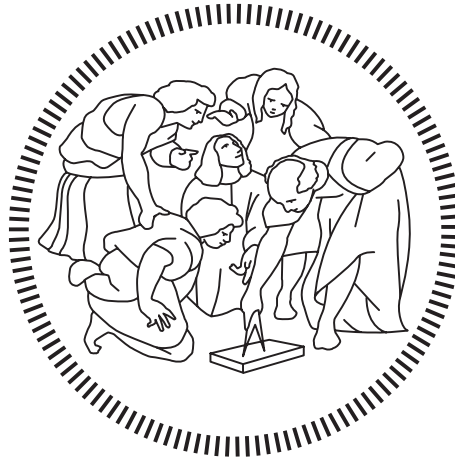


Politecnico di Milano

SCHOOL OF INDUSTRIAL AND INFORMATION ENGINEERING

Master of Science – Energy Engineering



Design and Off-Design Analysis of a Multistage Centrifugal Compressor for an A-CAES Plant

Supervisor

Prof. Marco ASTOLFI

Co-Supervisor

Prof. Paolo GAETANI

Candidate

Dario VALSESIA – 916716

Academic Year 2019 – 2020

Ringraziamenti

Ringrazio innanzitutto il prof. Marco Astolfi e il prof. Paolo Gaetani per la loro costante disponibilità e i loro fondamentali consigli. Il loro supporto si è rivelato indispensabile per lo sviluppo del programma di calcolo ex novo e per la stesura della tesi. Apprezzo molto la loro dedizione, nonostante tutti i problemi relativi alla pandemia ed allo smart working.

Ringrazio i miei genitori per la vicinanza ed il supporto, non solo durante la scrittura di questa tesi, ma da sempre. Ogni mio successo è e sarà sempre dedicato a loro.

Ringrazio tutti gli amici e tutte le persone che mi sono state vicine, migliorandomi la vita ogni giorno, nonostante la pandemia ed i vari lockdown.

Sommario

Le energie rinnovabili non programmabili, come l'eolico ed il fotovoltaico, stanno aumentando rapidamente la loro potenza installata a livello globale. La rete elettrica necessita di impianti di accumulo di energia per sostenere questa celere crescita. Le tecnologie più adatte per l'accumulo di energia su larga scala sono l'idroelettrico ad accumulo con pompaggio (PHES) e gli impianti di accumulo tramite aria compressa (CAES). Nel presente lavoro, un compressore impiegato in un impianto di accumulo adiabatico tramite aria compressa (A-CAES) dotato di un serbatoio isobaro di aria compressa (CAS) è progettato e la sua operazione fuori progetto è analizzata. Le peculiarità di questo compressore sono l'alta temperatura raggiunta alla fine della compressione (fino a 625°C in condizioni di progetto), l'elevato rapporto di compressione (pari a 80) e la pressione in uscita costante anche in condizioni di fuori progetto. I risultati di questo lavoro suggeriscono che il compressore è fattibile, ma i problemi maggiori sono lo stallo a basse portate massiche dovuto alla pressione in uscita costante ed i fenomeni di scorrimento viscoso (creep) causati dalle alte temperature.

Abstract

The non-programmable renewable energies, such as wind power and photovoltaic power, are experiencing a rapid increase in their installed power around the world. The electric system needs energy storage plants to sustain this fast growth. The most suitable systems for the large-scale energy storage are the pumped hydroelectric energy storage (PHES) and the compressed air energy storage (CAES). In the present work, a compressor employed in an adiabatic compressed air energy storage (A-CAES) plant with an isobaric compressed air storage (CAS) system is designed and its off-design operation is analysed. The peculiarities of this compressor are the high temperature reached at the end of the compression (up to 625°C in design conditions), the high compression ratio (equal to 80) and the outlet pressure fixed even in off-design conditions. The results of this work suggest that the compressor is feasible, but the biggest problems are the stall at low mass flow rates due to the constant outlet pressure constraint and the creep issues due to the high temperature reached.

Extended Abstract

I. CAES

At the beginning of the 21st century, the increased awareness in the threat that global warming poses on humanity pushed the adoption of renewable energy sources. Some types of renewable source, such as hydroelectricity and geothermal power, are programmable and some others, such as wind power and photovoltaic power, are non-programmable. A non-programmable energy source produces power only when the conditions are favourable and not when it is requested by the energy demand. For this reason, an energy storage system is the only feasible solution to have a big share of the electricity market supplied by non-programmable energy sources. The installed wind and photovoltaic power are growing fast and this growth is forecasted to continue in the near future, as reported in Figure 0.1 .

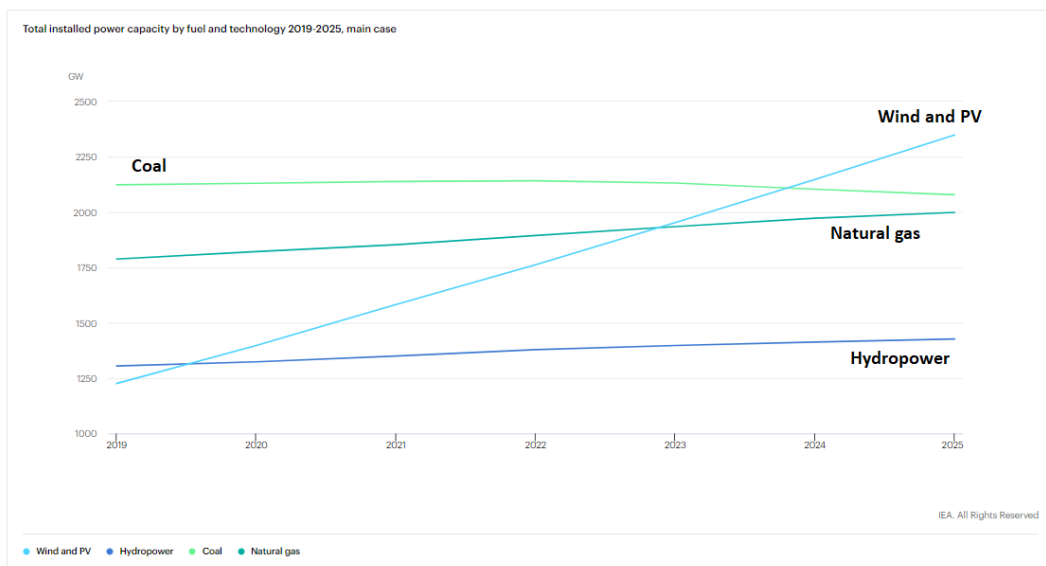


Figure 0.1 – Total installed power capacity by fuel and technology globally in 2019-2025 [1].

This increasing trend generates an interest in the energy storage systems. There are a huge number of energy storage technologies, but the only solutions that are suitable for large-scale commercial applications are the pumped hydroelectric energy storage (PHES) and the compressed air energy storage (CAES) [2]. The PHES is the leading and the most mature energy storage technology, however its further exploitation is limited due to the saturation

of potential locations. Moreover, it has long construction cycles, high maintenance costs and it affects the local environment [2].

So, a technology suitable to be exploited in the near future for large-scale applications is the CAES. In general, it consists in compressing air through a compressor, storing it in a compressed air storage (CAS) and expanding it using a turbine. The compression phase and the expansion phase are shifted in time to allow the system to store energy. The CAES technology has multiple versions, depending on how the air thermal energy generated by the compression is managed. These different types of CAES are the diabatic CAES (D-CAES), the isothermal CAES (I-CAES) and the adiabatic CAES (A-CAES) [3].

The D-CAES dissipates the thermal energy after the compression until the air is cooled down to approximately ambient temperature. This allows to have a simple system because there is no need of dealing with hot air, but the heat dissipation involves a big exergy loss. In fact, to expand the compressed air when the power needs to be produced, a fuel must be burnt to increase the temperature of the air entering the turbine. So, a D-CAES system is not a proper storage system because it needs to use a fuel source [3].

The I-CAES dissipates the thermal energy during the compression. In fact, an isothermal compression and expansion are the target of this technology. The expansion process absorbs the thermal energy needed to maintain the air temperature constant from the ambient, so no external energy sources are necessary and this type of CAES can be considered a proper energy storage system. However, this technology is mainly confined to small applications, since it must work with piston machinery to leave enough time for the heat exchange process to happen [3].

The A-CAES stores the thermal energy to use it during the expansion phase. This thermal energy can be stored in a dedicated thermal energy storage (TES) using a liquid or a solid or simply in the CAS itself as hot air. This last solution would require highly temperature-resistant storage volumes to sustain the high temperature already reached at relatively low pressure ratios, so no commercial applications are realized or expected in the near future. For this reason, the solution of an A-CAES equipped with a TES is more interesting. It works cooling down the air to approximately ambient temperature using heat exchangers and storing the thermal energy into the dedicated TES. This allows to store the cold air using cheaper materials for the CAS system. Moreover, a higher energy density is reached due to the higher density of cold air. The maximum storage temperature is the most important parameter for this type of plant because it highly influences the energy density, even if it does not affect much the cycle efficiency [3].

There are three versions of the A-CAES technology, depending on the storage temperature: low-temperature A-CAES, medium-temperature A-CAES and high-temperature A-CAES. The first two solutions have the advantages of working with off-shelf compressors and cheaper thermal liquids, but the high-temperature A-CAES has a higher energy density due to the higher storage temperature.

A high-temperature A-CAES plant needs a specially designed compressor due to the high pressure ratio and the high temperatures involved. This is exactly the subject of this thesis.

i. Case Study

The present work has the target of studying the compression system needed in the thesis of Marco Belloli and Adriano Hirn “Underwater Compressed Air Energy Storage (CAES): system design optimization, economics and simulation” [4]. In this work, the entire CAES plant is analysed and it is suggested to improve the study of the compression system. A scheme of the plant proposed by Belloli and Hirn is shown in Figure 0.2. The main characteristics of its compression system are an outlet pressure of about 80 bar, an overall design compression power of 75 MW and an outlet temperature of 625°C. Their proposed configuration is based on four parallel compression trains, each of them equipped with two shafts that rotate at different rotational speeds.

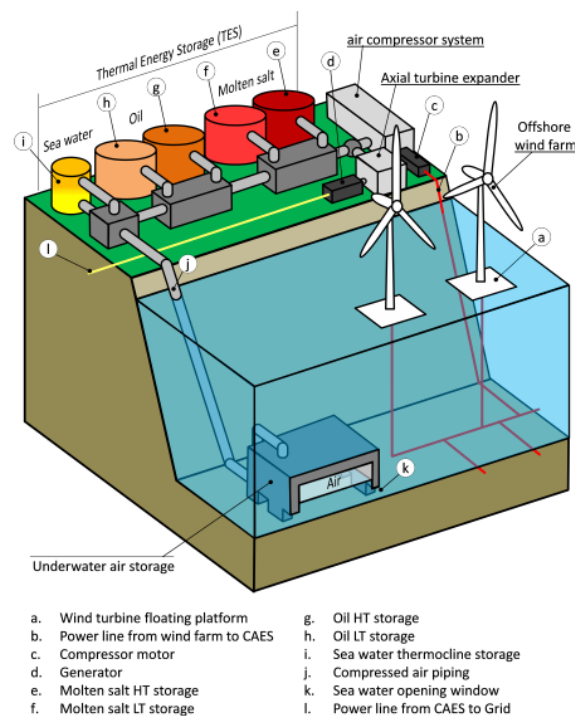


Figure 0.2 – Scheme of the CAES plant proposed by Belloli and Hirn [4].

II. Multistage Centrifugal Compressor

The best solution to fulfil the compression requirements of the previously described A-CAES plant is a multistage centrifugal compressor. The flexibility advantage and the higher compression ratios per stage of a centrifugal compressor with respect to an axial one are key

factors for the A-CAES plant since it works often in off-design conditions and the required compression ratio is very high.

In the present work, the air is considered an ideal gas and the isobaric specific heat c_p and the dynamic viscosity μ are calculated as function of temperature at the inlet of each stage and then kept constant during the stage compression. The deviation from the ideal gas model is big at high pressure and low temperature [3]. Since during the compression phase this situation does not happen, the ideal gas model is a good approximation. However, it is suggested to consider the real gas effects when dealing with the components of the plant that work at high pressure and low temperature (i.e., the heat exchangers and the CAS system).

In the present work, each centrifugal compressor stage is composed by an impeller, a vaneless diffuser and a volute or a return channel, depending on the position of the stage. If the stage is followed directly by another one on the same shaft and the air flow does not leave the inline configuration, a return channel is implemented. If the stage is the last one of its shaft or if the air flow needs to leave the inline configuration for some other reason (in the present work, this happens only if the air flow must go in an intercooler), that stage is equipped with a volute. The variable inlet guide vanes (VIGV) are another component that can be applied on a stage. They can be used only in the first stage of each shaft due to the lack of space [5].

There are two main types of impellers: the covered (or shrouded or closed) impellers and the uncovered (or unshrouded or open) impellers. For an inline multistage centrifugal compressor, the covered impellers are more used due to the high assembly tolerances [6].

i. Computational Procedure

The main target of the present work is a preliminary design of the compressor. This is obtained optimizing the efficiency of each stage using the software MATLAB. The optimization is based on a 0D method that analyses the thermodynamic and fluid dynamic conditions in all the points of the stage, using empirical correlations to estimate the energy losses.

A 0D method is adopted instead of a CFD simulation because the optimization process requires a lot of evaluations. A 0D method is less accurate than a CFD simulation, but it is way less computationally expensive. For this reason, the preliminary design of a complex machine is often realized using a 0D method, then the CFD simulation is used to improve the results.

ii. Loss Correlations

For the study of each stage of the compressor, an original set of correlations is realized using the work of multiple authors. Then, all the losses are converted into total specific enthalpy changes to obtain a homogeneous set.

The loss correlations adopted in this work are reported in the following list:

- VIGV loss: Original correlation derived from the experimental work of Coppinger [7].
- Impeller losses:
 - Incidence loss: Galvas correlation [8].
 - Blade loading loss: Coppage correlation [9].
 - Skin friction loss: Jansen correlation [9].
 - Clearance loss: Jansen correlation [9].
 - Mixing loss: Johnston and Dean correlation [9].
 - Leakage loss: Aungier correlation (for uncovered impellers) [10] and Osnaghi correlation (for covered impellers) [11].
 - Disk friction loss: Aungier correlation based on the work of Daily and Nece [10].
 - Recirculation loss: Coppage correlation [8].
- Vaneless diffuser loss: Coppage correlation [8].
- Volute losses:
 - Meridional velocity loss: Aungier correlation [10].
 - Tangential velocity loss: Aungier correlation [10].
 - Skin friction loss: Aungier correlation [10].
 - Exit cone loss: Aungier correlation [10].
- Return channel losses:
 - First bend losses: diffusion loss and curvature loss evaluated with the Aungier correlations [10].
 - Vaned channel losses: incidence loss evaluated with the Galvas correlation [8] and skin friction loss, blade loading loss and mixing loss evaluated with the Aungier correlations [10].
 - Second bend losses: diffusion loss and curvature loss evaluated with the Aungier correlations [10].

III. Code

i. Design

The preliminary design of the compressor is divided into two parts: the initial design and the design obtained through the MATLAB code. The initial design is necessary to limit the

computational cost of the process. In fact, the number of degrees of freedom in the design process of a multishaft multistage centrifugal compressor is extremely high and it is not feasible to leave all the decisions to the code.

In the initial design, the following quantities are chosen using a statistical approach: the number of stages, their division into the shafts, their compression ratios, their type (covered or uncovered impeller), the rotational speed of the shafts, the mass flow rate needed to absorb the design power and the position of the intercooler.

The code starts the optimization from the results of the initial design. It is used an optimization method called *patternsearch*, which is available in the Optimization Toolbox of MATLAB. This method is a trade-off between the computational cost and the problem of local minima. In fact, the method called *fmincon* is faster, but it suffers too much of local minima issues and other methods (i.e., the genetic algorithm *ga* and the *particleswarm*) are much more robust, but they are too computationally expensive [12]. The design process selects the optimum combination of some variables, which are called design variables. They are reported in Table 0.1 and Table 0.2 with their respective boundaries. The optimum design is defined as the most efficient design.

Component	Impeller					Vaneless diffuser
Design variable	D_2 [m]	N_b [-]	$\frac{D_{1,hub}}{D_{1,tip}}$ [-]	$\frac{D_{1,tip}}{D_2}$ [-]	α_2 [°]	$\frac{D_3}{D_2}$ [-]
Min value	$0.3 \cdot D_{2,stat}$	6	0.3	0.5	50	1.2
Max value	$D_2(u_{2,max})$	30	0.7	0.7	70	1.8

Table 0.1 – Design variables and their optimization interval for the impeller and the vaneless diffuser.

Component	Return channel		Volute	
Design variable	$N_{b,rc}$ [-]	$\frac{D_5}{D_{1,tip}}$ [-]	v_6 [m/s]	$\frac{A_6}{A_5}$ [-]
Min value	10	0.5	25	1
Max value	40	1.5	40	3

Table 0.2 – Design variables and their optimization interval for return channel and the volute.

In addition to the boundaries of the design variables, the optimization process must respect constraints on the results of the calculations. The stages must be subsonic, since the target of this work is to achieve a compression with high efficiency and there is no need to load a lot the machine. It is imposed to the stages to be flexible and to not stall easily at low mass flow rates. The shaft diameter is checked to assure that it is able to sustain the torque necessary. Finally, the temperature and the pressure exiting the whole compressor must be

close to the values indicated by Belloli and Hirn, which are respectively 625°C and about 80 bar.

ii. Off-Design

Once the entire compressor is designed, its geometry is fixed (with the exception of the VIGV) and the off-design conditions are studied. The particular aspect of a compressor for a CAES plant with an isobaric CAS is that the compression ratio must remain constant for every value of mass flow rate. Moreover, the outlet temperature is a critical parameter for the plant, so it must be controlled carefully even in off-design operation. To actively regulate the machine, three degrees of freedom are available: two VIGV (one at the inlet of each stage) and the rotational speed of the electric motor.

The off-design analysis is another optimization process, in which the power consumed by the whole compressor is minimized and the outlet pressure and temperature are constrained. The optimization is executed on MATLAB using the method *fmincon*. This time, this method does not present any major problem of local minima and the *patternsearch* method would be too computationally expensive. In fact, this optimization runs on the whole compressor and not on one stage at the time as for the design process. This implies that each iteration requires way more computations, so the only method that is reasonably fast is the *fmincon* method. Moreover, the off-design conditions must be computed for an interval of mass flow rates and not only in one point, so the computational cost is even bigger.

IV. Results

i. Design

The results of the optimization process executed with the code are reported in Table 0.3. The final design involves seven stages, two shafts and one intercooler. The first stage is divided into two identical parallel stages, so only one of them (with a mass flow rate that is half of the total one) is considered for the calculations. The first two stages are equipped with uncovered impellers, while all the other ones employ covered impellers. The reasons for this are that the first stage requires a fairly high compression ratio (uncovered impellers can rotate faster, so they can provide higher compression ratios) due to the position of the intercooler and that the volumetric flow rate in the first two stages is still high enough so that the tip clearance gap (which is quite high due to the high axial tolerances present in multistage compressors) does not affect the performances too much. The rotational speed of the low-pressure shaft is 16000 RPM and the one of the high-pressure shaft is 28000 RPM. The compression ratio of the whole compressor is equal to 80. The design power absorbed by the compressor is 18.761 MW and the average efficiency of the stages weighted on the isentropic work is 0.823.

Stage number	1	2	3	4	5	6	7
Rotational speed [RPM]	16000	16000	16000	28000	28000	28000	28000
Impeller type	Uncovered	Uncovered	Covered	Covered	Covered	Covered	Covered
β	2.800	2.700	1.950	1.700	1.570	1.480	1.402
$\eta_{is,ss}$	0.834	0.842	0.813	0.817	0.819	0.824	0.806
ω_s	0.955	0.841	0.659	0.941	0.787	0.677	0.607
ψ	0.430	0.463	0.538	0.525	0.527	0.526	0.543
$T_{tot,out}$ [K]	413.45	407.53	511.69	611.30	709.04	803.99	896.16
$p_{tot,out}$ [Pa]	283727	750776	1464067	2489017	3907841	5783679	8108891
$W_{is,ss}$ [$\frac{J}{kg}$]	100763	96676	86002	84001	84242	84133	81546

Table 0.3 – Main quantities for each stage.

It can be noticed that the specific speed ω_s remains between 0.6 and 1. According to the statistical data, the highest efficiency compressor stages work in this interval [13]. The head coefficient ψ is almost equal for the stages of the same type (for covered or uncovered impellers) so that the load is evenly distributed between them. The same compression ratio could be achieved with less than seven stages, but the flexibility and the efficiency would suffer. Since the compression train of a CAES plant does not have any specific need of being a compact machine, the less loaded solution with seven stages is preferred in this work. The temperature and pressure exiting the compressor satisfy the plant requirements.

The geometry of the compressor is illustrated in Figure 0.3. The two parallel stages composing the first compression stage are installed in a back-to-back configuration and the dimension of the stages reduces as the compression proceeds. All the stages on the high-pressure shaft almost reach the limit on the impeller tip speed u_2 . So, since they work at the same rotational speed, their outlet impeller diameter D_2 is almost equal for all of them.

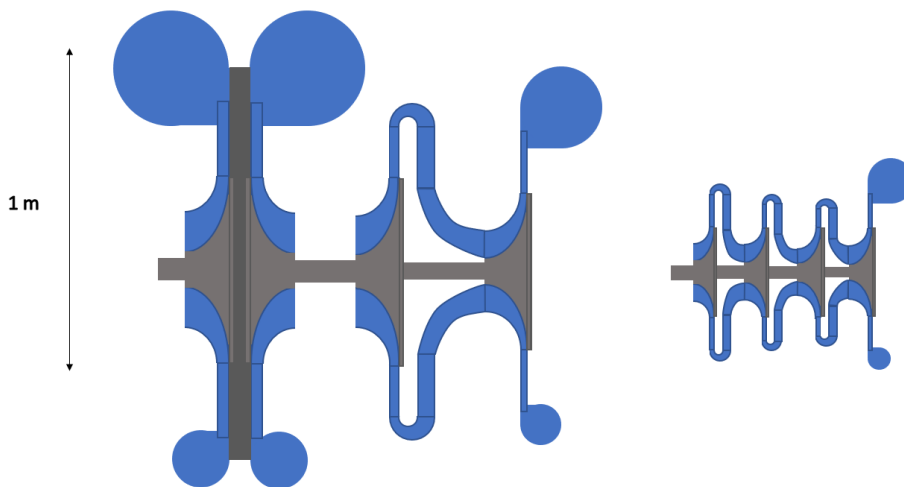


Figure 0.3 – Scale section of the multistage compressor. The stage number increases from left to right.

The loss mechanisms on each stage are reported in Figure 0.4. It can be noticed that the leakage loss has a higher impact on the smaller stages. This happens because that loss mechanism is linked to the leakage seal gap, which is the same for every stage due to technological limits. So, it has a higher effect on the small stages.

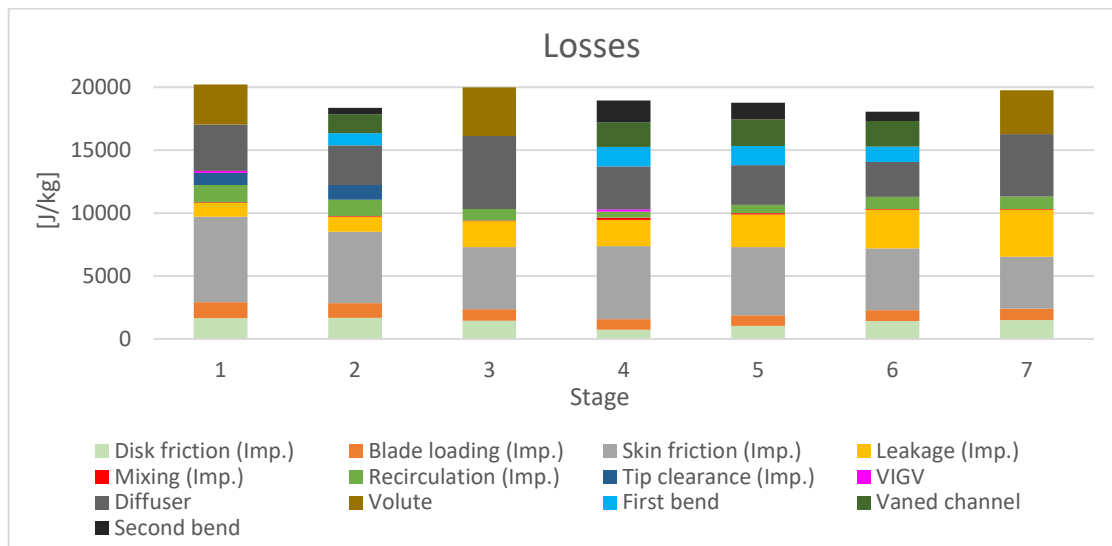


Figure 0.4 – Types of losses for each stage.

ii. Off-Design

The off-design analysis is conducted between 50% and 100% of the nominal flow rate, running the code every 10%. The graphs of the power, the efficiency and the outlet temperature of the entire compressor in off-design operation are reported, respectively, in Figure 0.5, Figure 0.6 and Figure 0.7. It can be noticed that the efficiency decreases as the mass flow rate decreases because the more the machine works far from the design conditions, the worse its performances are.

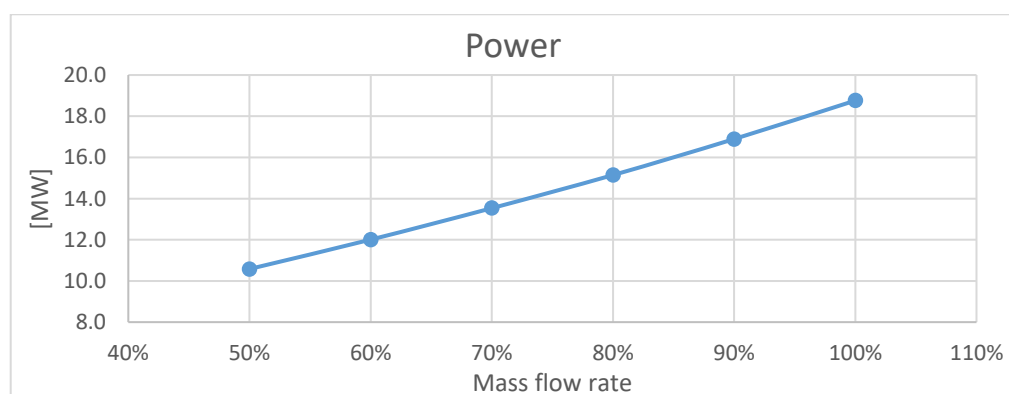


Figure 0.5 – Compression power in off-design operation.

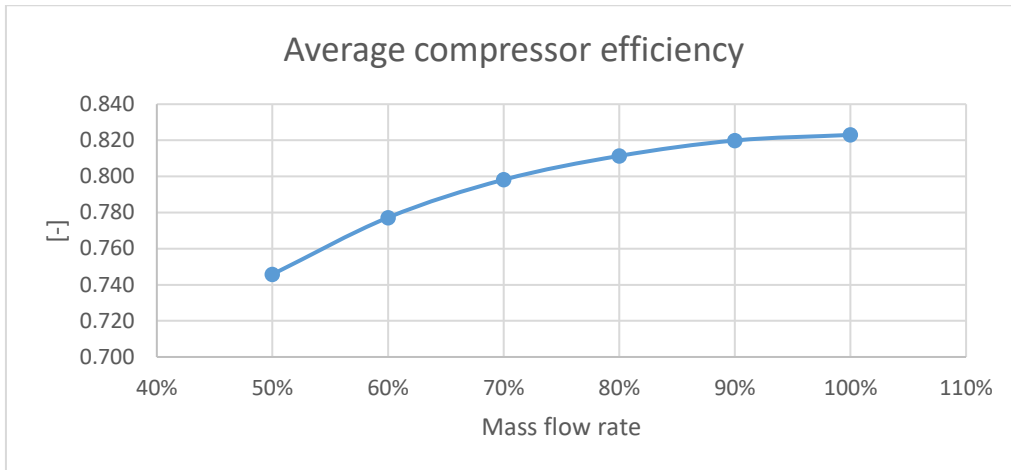


Figure 0.6 – Average compressor efficiency in off-design operation.

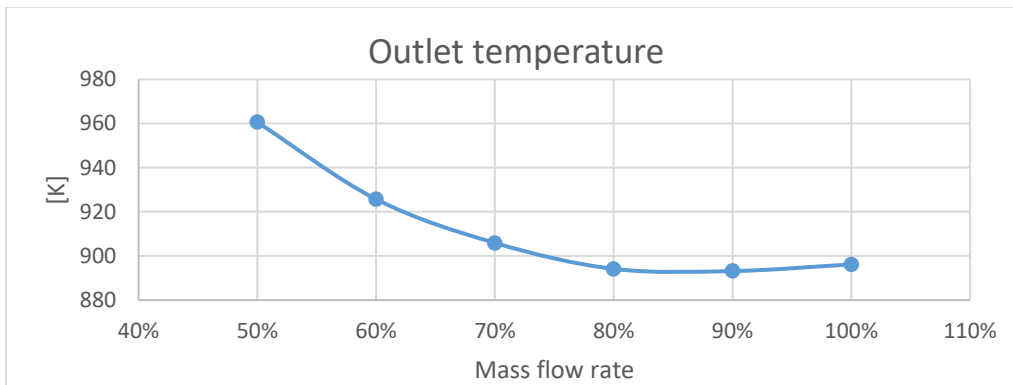


Figure 0.7 – Temperature at the outlet of the compressor in off-design operation.

The compression ratio and the efficiency of each stage in off-design conditions are reported, respectively, in Figure 0.8 and Figure 0.9. The compression ratio of the first stage increases because the code exploits the intercooler to compensate for the increase in temperature caused by the reduction in efficiency. Doing so, the temperature at the outlet can be controlled for the region at high mass flow rate (above 80%), but when the mass flow rate reduces too much, it is not possible to compensate anymore and the outlet temperature must increase. This behaviour is shown in Figure 0.7. The code wants to minimize the temperature (remaining into the constraints) because a colder compression requires less power. Since the compression ratio of the first two stages increases, the one of all the other stages must decrease to maintain the global compression ratio constant, as needed by the plant.

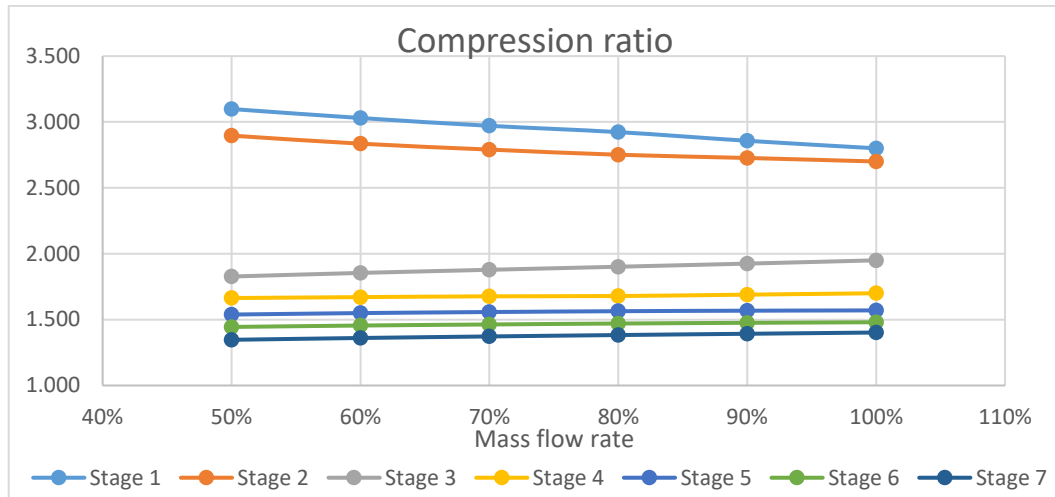


Figure 0.8 – Compression ratio for each stage in off-design operation.

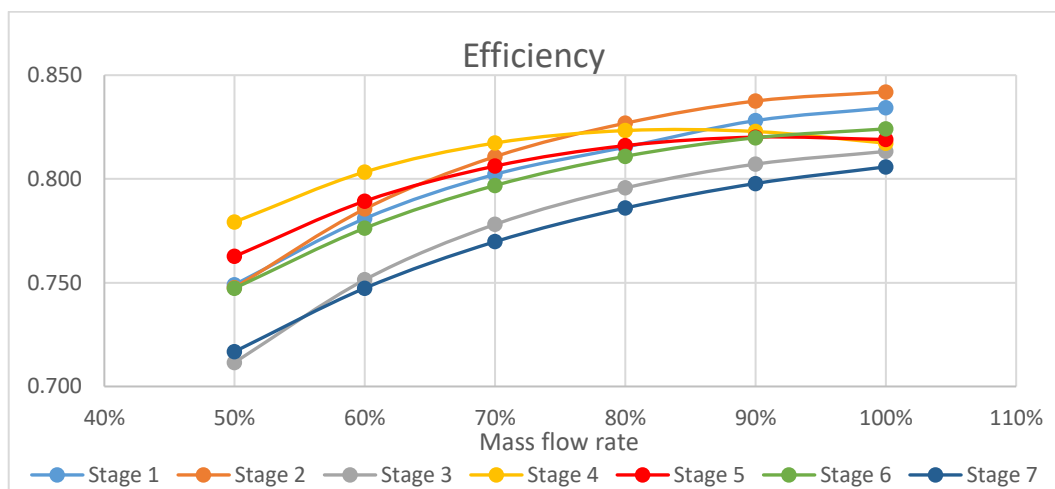


Figure 0.9 – Efficiency for each stage in off-design operation.

For the drivetrain, it is selected the configuration described in Figure 0.10. The variable-frequency drive (VFD) is necessary to have a variable rotational speed during the off-design operation. The induction motor is preferred over the alternatives because it is a robust and cheap solution to work at rotational speeds close to the design one.



Figure 0.10 – Conceptual scheme of the electrical and mechanical system.

V. Conclusions

The solution proposed in the present work is a preliminary design and off-design analysis of a multistage centrifugal compressor employed in an A-CAES plant equipped with an isobaric CAS. The computational procedure is very detailed, considering that it is based on a 0D method.

The results are very reasonable both for the design part and for the off-design part. It must be noticed that there could be stall problems at very low mass flow rates (below 60% of the nominal one).

To improve this work, a few suggestions are listed. The splitter blades can be modelled to improve the performances of the impeller. The diffuser can be equipped with variable vanes that change their geometry in off-design operation. This should help with the design efficiency (a vanned diffuser is more efficient than a vaneless one) and with the flexibility [14]. The pre-swirl could be used even in design conditions, optimizing the VIGV angle. The isobaric specific heat and the dynamic viscosity could be considered variable during each stage compression (even if this would increase the computational cost). A different optimization method could be applied to reduce the local minima problems.

Table of Contents

Ringraziamenti	III
Sommario	V
Abstract	VII
Extended Abstract	IX
I. CAES	IX
i. Case Study	XI
II. Multistage Centrifugal Compressor	XI
i. Computational Procedure	XII
ii. Loss Correlations	XII
III. Code	XIII
i. Design	XIII
ii. Off-Design	XV
IV. Results	XV
i. Design	XV
ii. Off-Design	XVII
V. Conclusions	XX
Table of Contents	XXI
List of Figures	XXV
List of Tables	XXIX
List of Symbols	XXXI
Chapter 1 CAES	1
1.1 Storage Technologies	2
1.2 CAES Technologies	3
1.2.1 D-CAES	4
1.2.2 I-CAES	5
1.2.3 A-CAES	6
1.2.4 UW-CAES	8
1.3 Case Study	9
Chapter 2 Multistage Centrifugal Compressor	11
2.1 Theoretical Overview	11
2.1.1 Compression Thermodynamics	11
2.1.2 Air Properties	14
2.1.3 Dimensionless Statistical Parameters	16

2.2	Centrifugal Compressor Components	18
2.2.1	Variable Inlet Guide Vanes	18
2.2.2	Impeller	19
2.2.3	Diffuser.....	21
2.2.4	Volute	21
2.2.5	Return Channel.....	23
2.3	Computational Procedure	23
2.3.1	Stage Solution	24
Chapter 3	Loss Correlations.....	28
3.1	Variable Inlet Guide Vanes Loss.....	28
3.2	Impeller Losses.....	30
3.2.1	Incidence Loss.....	31
3.2.2	Blade Loading Loss.....	31
3.2.3	Skin Friction Loss	32
3.2.4	Clearance Loss	33
3.2.5	Mixing Loss.....	34
3.2.6	Leakage Loss.....	34
3.2.7	Disk Friction Loss	36
3.2.8	Recirculation Loss.....	38
3.3	Vaneless Diffuser Loss	39
3.4	Volute Losses	39
3.4.1	Meridional Velocity Loss.....	40
3.4.2	Tangential Velocity Loss	40
3.4.3	Skin Friction Loss	41
3.4.4	Exit Cone Loss	41
3.5	Return Channel Losses	42
3.5.1	First Bend Losses	42
3.5.2	Vaned Channel Losses	44
3.5.3	Second Bend Losses.....	46
Chapter 4	Code	48
4.1	Design.....	48
4.1.1	Initial Design	49
4.1.2	Optimization Method	51
4.1.3	Assumptions	52
4.1.4	Design Variables	54
4.1.5	Non-Linear Constraints	56
4.1.6	Shaft Torque	58
4.1.7	Starting Values	59
4.1.8	Intercooler	60
4.2	Off-Design	60
4.2.1	Optimization Method	61
4.2.2	Control Variables	62
4.2.3	Non-linear Constraints	62
Chapter 5	Results	64
5.1	Initial Design	64
5.2	Design.....	66

5.2.1	Geometry	68
5.2.2	Loss Mechanisms	72
5.2.3	Velocity Triangles	73
5.3	Shaft Torque	77
5.4	Off-Design	79
5.4.1	Control Variables and Stage Analysis	81
5.4.2	Loss Mechanisms	85
5.4.3	Stall analysis	89
5.5	Drivetrain	90
Chapter 6	Conclusions	95
6.1	Future Improvements	97
Bibliography	99

List of Figures

Figure 0.1 – Total installed power capacity by fuel and technology globally in 2019-2025 [1].....	IX
Figure 0.2 – Scheme of the CAES plant proposed by Belloli and Hirn [4].	XI
Figure 0.3 – Scale section of the multistage compressor. The stage number increases from left to right.	XVI
Figure 0.4 – Types of losses for each stage.	XVII
Figure 0.5 – Compression power in off-design operation.....	XVII
Figure 0.6 – Average compressor efficiency in off-design operation.	XVIII
Figure 0.7 – Temperature at the outlet of the compressor in off-design operation.	XVIII
Figure 0.8 – Compression ratio for each stage in off-design operation.....	XIX
Figure 0.9 – Efficiency for each stage in off-design operation.....	XIX
Figure 0.10 – Conceptual scheme of the electrical and mechanical system.	XIX
Figure 1.1 – Total installed power capacity by fuel and technology globally in 2019-2025 [1].....	2
Figure 1.2 – Scheme of the C-HyPES (left) and of the O-HyPES (right) [3].....	6
Figure 1.3 – Block diagram of a high-temperature A-CAES as it was designed in the AA-CAES project [3].....	7
Figure 1.4 – Scheme of the CAES plant proposed by Belloli and Hirn [4].	10
Figure 2.1 – Difference between ideal gas and real gas models. The cp is used as an example for other thermodynamic properties. [3]	15
Figure 2.2 – Cordier diagram with the type of machine suggested [24]. Ns is the same quantity as the ωs indicated in this work.	17
Figure 2.3 – An example of a VIGV system [7].	19
Figure 2.4 – Covered 3D-impeller with twisted backward-curved blades. The photo was taken before the cover was brazed on the impeller [5].....	20
Figure 2.5 – Vaneless diffuser geometry [5].	21
Figure 2.6 – Volute geometry [10].	22
Figure 2.7 – Volute cross section with secondary flow pattern [10].	22
Figure 2.8 – Return channel geometry [10].	23
Figure 3.1 – Pressure loss coefficient in function of the VIGV average outlet flow angle [7]. In this work, the experimental results for the flat plate shape are used.	29
Figure 3.2 – Third-degree polynomial that interpolates the Coppinger’s results. The $R2$ parameter shows that the experimental data are really close to the model.	29
Figure 4.1 – Flow chart of the design algorithm.	49
Figure 4.2 – CD as function of the seal geometry and the Reynolds number [11].	53
Figure 4.3 – Statistical values of efficiency as function of ωs [13].	59
Figure 4.4 – Illustrative compressor performance map [8].	61
Figure 5.1 – Actual impeller tip speed and maximum impeller tip speed for each stage.....	68
Figure 5.2 – Scale section of the multistage compressor. The stage number increases from left to right.	69
Figure 5.3 – Impeller and vaneless diffuser diameters for each stage.	70

Figure 5.4 – Diffuser outlet diameter to impeller outlet diameter ratio for each stage.....	71
Figure 5.5 – Inlet and outlet impeller blade heights for each stage.	71
Figure 5.6 – Number of blades present in the impeller and in the vaned channel of the return channel for each stage.	72
Figure 5.7 – Types of losses for each stage.	72
Figure 5.8 – Impeller velocity triangles of stage 1.	74
Figure 5.9 – Impeller velocity triangles of stage 2.	74
Figure 5.10 – Impeller velocity triangles of stage 3.	75
Figure 5.11 – Impeller velocity triangles of stage 4.	75
Figure 5.12 – Impeller velocity triangles of stage 5.	75
Figure 5.13 – Impeller velocity triangles of stage 6.	76
Figure 5.14 – Impeller velocity triangles of stage 7.	76
Figure 5.15 – Relative Mach number at the tip diameter at the inlet of the impeller for each stage.	77
Figure 5.16 – Comparison between the mechanical requirements and the actual values for the hub diameter of each stage of the low-pressure shaft.	78
Figure 5.17 – Comparison between the mechanical requirements and the actual values for the hub diameter of each stage of the high-pressure shaft.	78
Figure 5.18 – Temperature at the outlet of the compressor in off-design operation.	79
Figure 5.19 – Thermal power dissipated by the intercooler in off-design operation.	80
Figure 5.20 – Compression power absorbed by the whole compressor in off-design operation....	80
Figure 5.21 – Average compressor efficiency in off-design operation.	81
Figure 5.22 – VIGV off-design regulation for stage 1.	82
Figure 5.23 – VIGV off-design regulation for stage 4.	82
Figure 5.24 – Rotational speed off-design regulation for the low-pressure shaft.	82
Figure 5.25 – Rotational speed off-design regulation for the high-pressure shaft.	83
Figure 5.26 – Compression ratio for each stage in off-design operation.	84
Figure 5.27 – Efficiency η_{is} , η_{ss} for each stage in off-design operation.	84
Figure 5.28 – Loss distribution for stage 1 in off-design operation.	85
Figure 5.29 – Loss distribution for stage 2 in off-design operation.	86
Figure 5.30 – Loss distribution for stage 3 in off-design operation.	86
Figure 5.31 – Loss distribution for stage 4 in off-design operation.	87
Figure 5.32 – Loss distribution for stage 5 in off-design operation.	87
Figure 5.33 – Loss distribution for stage 6 in off-design operation.	88
Figure 5.34 – Loss distribution for stage 7 in off-design operation.	88
Figure 5.35 – Impeller outlet absolute flow angle for each stage in off-design operation.	89
Figure 5.36 – De Haller parameter for each stage in off-design operation.	90
Figure 5.37 – Example of a mechanical system for an IGC. Usually, more than one pinion is connected [39].	91
Figure 5.38 – Conceptual scheme of the electrical and mechanical system.	92
Figure 5.39 – High speed induction motor capability curve (10000 HP = 7.46 MW). The vertical lines represent four different rotor sizes, the oblique lines are just conservative interpolations [40].	92
Figure 5.40 – Technical data about the ACS5000 drives produced by ABB [41].	93
Figure 5.41 – Technical data specific for the model ACS5000-069-W03A-E6-010 [41].	93

Figure 5.42 – Technical data about the MV Motors TM21-G induction motor produced by TMEIC [42]. 94

List of Tables

Table 0.1 – Design variables and their optimization interval for the impeller and the vaneless diffuser.	XIV
Table 0.2 – Design variables and their optimization interval for return channel and the volute... ..	XIV
Table 0.3 – Main quantities for each stage.	XVI
Table 2.1 – Air composition by volume adopted in this work.	16
Table 2.2 – Values for the reference temperature, for the reference dynamic viscosity at the reference temperature and for the Sutherland constant [23].	16
Table 2.3 – Points and their position for a stage with a volute and for a stage with a return channel.	25
Table 4.1 – Design variables and their optimization interval for the impeller and the vaneless diffuser.	54
Table 4.2 – Design variables and their optimization interval for return channel and the volute... ..	55
Table 5.1 – Values used in the initial design.	65
Table 5.2 – Results of the initial design.....	65
Table 5.3 – Main quantities for each stage.	67

List of Symbols

Roman Symbols

A	Area	m^2
b	Passage height	m
c_f	Friction coefficient	–
c_p	Isobaric specific heat	$J/kg/K$
c_v	Isochoric specific heat	$J/kg/K$
D	Diameter	m
h	Specific enthalpy	J/kg
L	Length	m
M	Mach number	–
MM	Molar mass	$kg/kmol$
N	Number of elements	–
p	Pressure	Pa
P	Power	W
Q	Volumetric flow rate	m^3/s
r	Radius	m
R	Gas constant	$J/kg/K$
R_a	Average roughness	μm
Re	Reynolds number	–
T	Temperature	K
v	Absolute flow velocity	m/s
w	Relative flow velocity	m/s
W	Specific work	J/kg

Greek Symbols

α	Absolute angle from the meridional direction	<i>rad</i>
β	Relative angle from the meridional direction	<i>rad</i>
γ	Specific heat ratio	—
Δ	Difference in the value of a quantity	
ε	Gap	<i>m</i>
η	Efficiency	—
κ	Curvature	<i>m</i> ⁻¹
μ	Dynamic viscosity	<i>Pa · s</i>
ρ	Fluid density	<i>kg/m</i> ³
φ	Flow coefficient	—
ψ	Head coefficient	—
ω	Rotational speed	<i>rad/s</i>

Subscript Symbols

0	Point in the inlet duct
0a	Point at the VIGV inlet
0b	Point at the VIGV outlet
1	Point at the impeller inlet
2	Point at the impeller outlet
3	Point at the vanless diffuser outlet
4	Point at the 1 st bend outlet
5	Point at the vaned channel outlet / volute outlet
6	Point at the 2 nd bend outlet / conical diffuser outlet
ax	Relative to the axial direction
b	Relative to the blades
closed	Relative to a covered impeller
deg	Angle expressed in degrees instead of radians
eul	Eulerian
f	Relative to the flow
g	Relative to the blade direction or to any metallic surface
hub	Relative to the hub diameter (the smallest one)
imp	Relative to the impeller
m	Relative to the meridional direction
max	Maximum value
mid	Relative to the mid diameter (mathematical average)
min	Minimum value
open	Relative to an uncovered impeller
opt	Optimal
rad	Relative to the radial direction
th	Relative to the throat
tip	Relative to the tip diameter (the biggest one)
tot	Total quantity
u	Tangential component
vc	Relative to the vaned channel of the return channel

Superscript Symbols

- * Molar quantity
- Average quantity
- Per unit of time quantity

Chapter 1

CAES

The energy storage has existed since the industrial revolution. When the main energy sources were fossil fuels, the energy storage consisted in the chemical energy contained in the fuel itself. The coal, oil and natural gas were burnt when there was a need for energy and they were stored for later use when the demand was not present. Until the 1960s, all the energy storage needed for the energy system was in the chemical energy of the fuels and in the potential energy of the water in the hydroelectric power plants, so it was not a problem at all.

Then, starting in the late 1960s, baseload generation with nuclear power plants and even larger lignite coal fired power plants was introduced. Suddenly, there was an economic case to store inexpensive off-peak power from baseload generation capacities and transfer it to peak-load hours [3]. Nowadays, at the beginning of the 21st century, the energy storage is developed for a completely different reason, which to allow the integration in the energy mix of a big share of non-programmable renewable energy sources. A non-programmable energy source is characterized by the fact that it produces power only when the conditions are favourable and not when it is requested by the energy demand.

The amount of carbon dioxide (CO_2) in the atmosphere has changed substantially since the industrial revolution, due to human activities. Future projections are that, in the absence of controlling factors, the rate of increase in atmospheric carbon dioxide will accelerate and that its atmospheric concentration will double from its pre-industrial value within the next hundred years. The majority of scientists agree that the growing CO_2 concentration in the atmosphere is responsible for the increase in the average global temperature [15]. This phenomenon is usually called global warming and it is recognized to be dangerous for humanity, even if there is no agreement in the scientific community on its precise consequences. In order to fight global warming, numerous nations around the world have signed agreements to limit their emissions of greenhouse gas (GHG), the most important of which are the Kyoto Protocol (1997) and the Paris Agreement (2015). It is recognized that the use of fossil fuels as energy sources is one of the main causes of the increase in the carbon dioxide atmospheric concentration. In this work, the focus is on the electricity sector and the strategies to decrease its emissions.

There are several ways to limit the carbon dioxide emissions linked to the electricity generation without affecting the economic growth: increasing the energy efficiency,

implementing CCS (carbon capture and storage) systems, increasing the share of renewable sources in the energy mix and others.

Among the various renewable sources, photovoltaic and wind energy are two examples of non-programmable power generation. They are very interesting because they have a lot of potential to be exploited in the coming years, in contrast to the hydropower, as shown by Figure 1.1. In fact, even if hydropower is a cheap programmable renewable source used for centuries, its new installed power is expected to reduce in the coming years due to the lack of suitable locations [1].

The forecasted growth that wind and photovoltaic power are experiencing represents a challenge for the electric system. As already discussed, these sources are non-programmable. So, to allow a higher percentage of them into the energy mix, the energy storage is needed to maintain the power network stable and reliable: it can be used to store the non-programmable energy to make it dispatchable. This means that the energy production can be decoupled from the energy demand: the energy is produced when the ambient conditions are favourable but it is dispatched when needed, thanks to the storage. So, it is clear the different reason why energy storage is needed nowadays with respect to the 1960s.

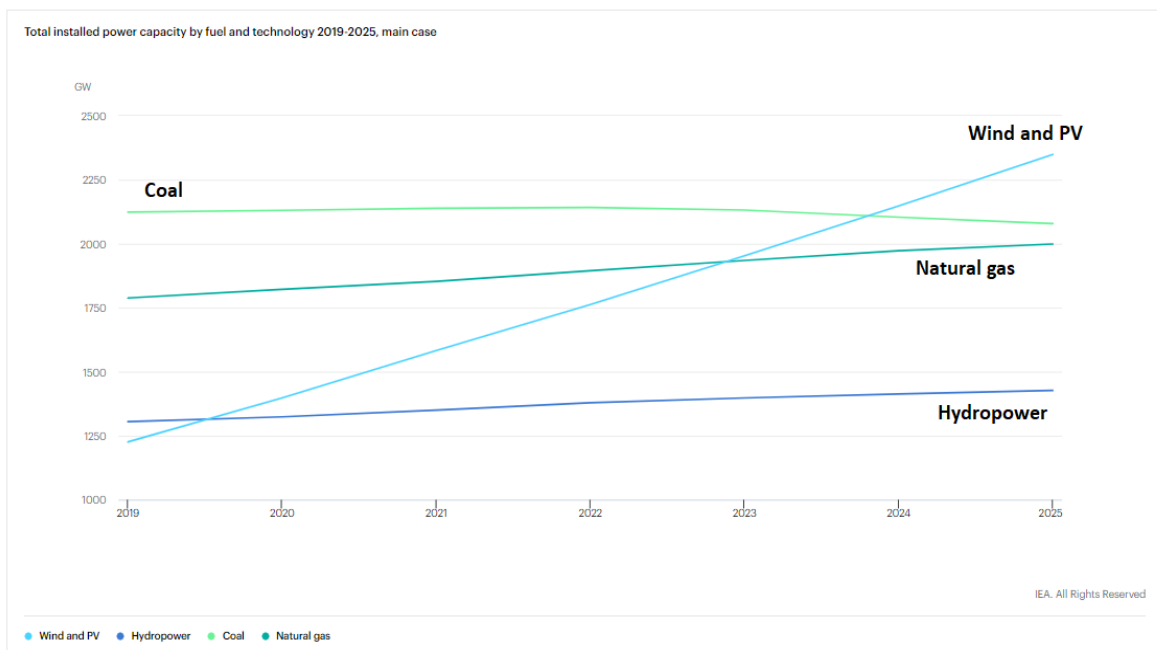


Figure 1.1 – Total installed power capacity by fuel and technology globally in 2019-2025 [1].

1.1 Storage Technologies

There are multiple storage technologies available, each of them is more suitable for some applications and less for others. These technologies are pumped hydroelectric energy storage (PHES), flywheels, compressed air energy storage (CAES), capacitors, superconducting

magnetic energy storage (SMES), thermal energy storage (TES), solar fuels, hydrogen fuel cells, Li-ion batteries, lead-acid batteries. Comparing the investment cost, capacity, lifetime, energy density and storage duration, PHES and CAES are the most suitable to be used in large-scale commercial applications [2].

PHES is one of the most widely used energy storage systems, which has demonstrated its merits in terms of technological maturity, high cycle efficiency, high rated power, long service life and low operating cost. The problems with this technology are that the location choices are highly restricted, construction cycles are long, maintenance costs are high and it impacts the local environment, so the further utilization of PHES is limited. In addition to PHES, CAES is another feasible way to realize large-scale power storage. In comparison with PHES, CAES has relatively low impact on the environment and construction cost [2].

The fundamental idea to store electrical energy by means of compressed air dates back to the early 1940s. However, until the late 1960s, when the need of energy storage became real, the development of CAES was pursued neither in science nor in industry. In 1969, the need for storage capacity in northern Germany led to the decision of developing a CAES plant in this region, which was the Huntorf plant. The decision was supported by suitable geological formations for storing large amounts of compressed gas in available underground salt domes. Furthermore, there was a need for black start capability for the northern German grid, which could be provided by CAES [3].

1.2 CAES Technologies

The CAES system works compressing air through a compressor, storing it in a compressed air storage (CAS) and expanding it using a turbine. The compression phase and the expansion phase are shifted in time: the compression phase is the charging phase of the system and the expansion one is the discharging phase. When there is abundance of electricity production and it is decided to charge the CAES plant, electrical power is provided to the electrical motor of the compressor and a flow of air is compressed and stored in the CAS. When there is a demand of electricity and the CAES plant needs to be discharged to provide electrical power, the compressed air in the CAS is expanded inside the turbine that generates electrical power through the generator. This is the main working mechanism of a CAES plant.

The CAS system can be isobaric or isochoric. Some examples of isochoric CAS are underground caverns or man-made vessels. In this case, the pressure indicates the state of charge. A method to have an isobaric CAS is to use a hydrostatic head. In this case, the volume represents the state of charge of the CAS [3].

Since compressing the air involves its increment in temperature, it is important how the air thermal energy is managed. This management generates three different types of CAES: the diabatic CAES (D-CAES), the isothermal CAES (I-CAES) and the adiabatic CAES (A-CAES) [3].

1.2.1 D-CAES

The first two CAES plants to be put into operation were the Huntorf plant (Germany) and the McIntosh plant (USA). To the present date (2021), these two plants are the only realized and in operation CAES projects. They started operating, respectively, in 1978 and in 1991. Both of them are of the D-CAES type [3]. With the D-CAES technology, the air is cooled down to approximately ambient temperature after the compression and all its heat is dissipated into the environment. The cold compressed air is then stored into the CAS. When the CAS is discharged, the air has to increase its temperature before expanding in the turbine to prevent the icing of the machine. This is usually done bringing the cold compressed air in a combustor and burning it with natural gas. The dissipation of the thermal energy of the compressed air involves a big waste of exergy that damages the plant performances and produces a big irreversibility, but it is the simplest technology for a CAES plant and this is why it was chosen for the early plants. The D-CAES technology avoids dealing with hot air, which would require a more expensive system. The simplest way is to cool it down after the compression and to store it at low temperature.

The discharging process involves the introduction of fuel inside the D-CAES plant, so it cannot be considered anymore a storage plant but it has to be considered a hybrid plant: it is partially a peak generating technology and partially an electrical energy storage [3].

The purpose of the early CAES plant was different from the ones studied nowadays. At the time of Huntorf and McIntosh, aspects such as black start capability and economic optimization by transferring cheaper baseload power toward peak hours were important. Today, balancing the intermittent renewable energy power feed-in can be considered the main driver toward CAES [3]. The motivation for developing CAES technology is to achieve energy sustainability and to reduce emissions, so the current technology development aims to avoid using fossil fuel in CAES systems [2].

Both the Huntorf plant and the McIntosh plant have some concepts that improve their performances. In the Huntorf plant, ambient air is compressed in an intercooled process by two separate compressor units. The intercooling limits the exergy losses of the diabatic process, but still more than 25% of the exergy supplied as electrical energy during compression is wasted due to cooling. Even the expansion process is divided into two separate turbines and before each of them a combustor is present. In the more recent McIntosh plant, some new improvements were made. A multiple stage intercooling is introduced, which reduces exergy losses during compression even further. However, the usage of an exhaust-heat recuperator is the main difference and advancement compared to the Huntorf plant: during the expansion phase, the still hot exhaust gases exiting the low-pressure expander are used to preheat the compressed air entering the high-pressure turbine [3].

Both the Huntorf plant and the McIntosh plant use as CAS a salt cavern, which is isochoric. To improve the reliability of the turbine, the compressed air is commonly throttled to a constant pressure before it is expanded in the turbine. A throttling valve is placed at the outlet

of the isochoric CAS [16]. This process implies a further exergy loss, which degrades the plants performances even more.

1.2.2 I-CAES

The I-CAES technology works trying to prevent an increase in the air temperature in the compressor during charging and a temperature drop in the expansion device during discharging. This concept improves the performances with respect to the D-CAES type: the compression does not generate big irreversibilities when the heat is released into the environment because the process is achieved with low temperature differences. Also, there is no need to burn fuel in the plant because the heat necessary to avoid icing during the expansion is provided by the ambient surroundings. So, the I-CAES is a proper storage plant that does not require any additional source of energy.

All the I-CAES concepts known so far are based on piston machinery since these machines can perform a comparably slow compression or expansion process, which leaves enough time for the heat transfer phenomena [3].

The concept of I-CAES was first implemented in the so called hydro-pneumatic energy storage. In these devices a liquid is used to compress the gas. In the case of closed cycle hydro-pneumatic energy storage (C-HyPES), this is achieved by pumping a liquid, for example hydraulic oil, directly into the CAS, where the gas volume is reduced, which causes the gas compression. When electricity is needed, the gas is expanded by letting the liquid flow in reverse direction through the pump-turbine (P/T), which now acts as a turbine driving the generator. The major drawback of C-HyPES is their low energy density. For this reason, these systems have not been built commercially yet. To overcome this problem, an open cycle concept (O-HyPES) combines the higher energy densities of air-air systems with the advantages of applying a liquid as working medium. In an O-HyPES system, air is compressed by a liquid piston before entering the CAS at high pressure. This concept requires at least two alternating cylinders, where a liquid can be pumped into and out of, and a system of valves allowing a cyclic air supply and release. In contrast to the closed cycle system, O-HyPES has been realized not only at laboratory scale but it has been further developed to a utility scale [3]. A scheme of these two concepts is represented in Figure 1.2.

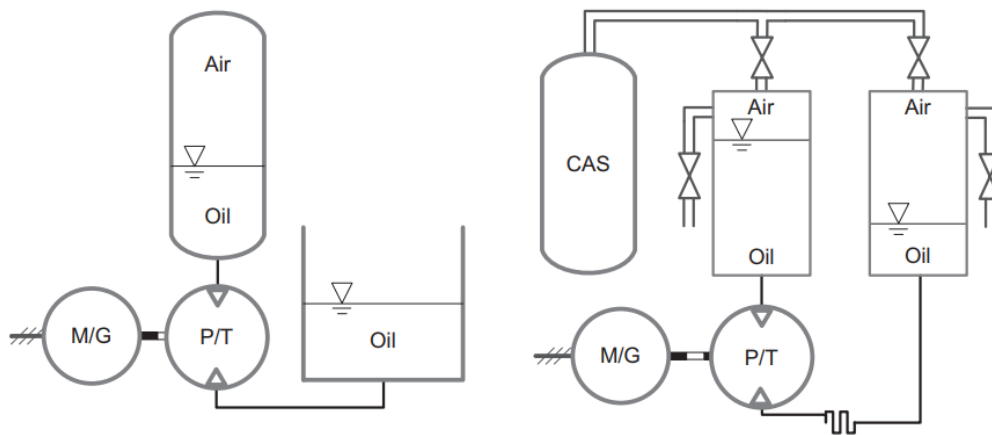


Figure 1.2 – Scheme of the C-HyPES (left) and of the O-HyPES (right) [3].

The use of hydraulic pumps and motors enables precise compression and expansion of air. Moreover, it leaves enough time for the heat transfer with the surroundings of the CAS to occur, so that a high level of thermal and overall system efficiency is reached [17]. In both concepts, the charging and discharging power is limited by the heat exchange area formed by the liquid surface in contact with the gas. At high power, the temperature gradients increase so the efficiency of the no longer isothermal process decreases. This limitation can be overcome by spraying water into the compression chamber, which results in a huge water surface in contact with the gas. In this way, an efficient heat transfer is reached and the use of common piston technology becomes possible. Of course, these pistons must be modified to withstand the water content inside. The latest researches propose the compression of a pre-mixed foam to further improve the heat transfer [3].

1.2.3 A-CAES

The A-CAES technology is based on the concept of storing the heat generated from the compression process to use it during the expansion. In theory, there are two ways of doing this: with a dedicated thermal energy storage (TES) or without it.

The simplest way to reuse the temperature-related part of the exergy of the compressed air is to store the hot air itself inside a combined thermal energy and compressed air storage volume. Doing so, the complication of a dedicated TES is avoided. This type of A-CAES has only been realized at laboratory scale so far and a commercial application cannot be expected in the near future due to considerable material requirements for the CAS device. In fact, the high temperatures already reached at rather low pressure ratios require highly temperature-resistant storage volumes, so A-CAES without TES are restricted to rather low storage pressures and consequently to low energy densities as well. Moreover, as a consequence of the relatively low density of hot compressed air, a huge surface has to be protected against heat losses. Both issues imply a high investment cost [3].

These problems lead to the use of a dedicated TES device in most of the A-CAES concepts. By removing the temperature related part of the exergy from the air stream, the cooled pressurized air can be stored in a CAS of any kind. Additionally, much higher final pressures can be addressed and higher energy densities can be reached due to the higher density of cold air. Typical final pressures of A-CAES with TES are at least equal to 60 bar. The maximum storage temperature is the most important parameter of this type of plant because it highly influences the energy density, even if does not affect much the cycle efficiency [3].

The low-temperature A-CAES with TES works with storage temperatures below 200°C. It has the advantages of being able to use cheaper liquids as heat storage medium, to use off-shelf compressor technology and to have a faster start-up time, which is important in a storage plant. However, to have a good energy density, it needs to have heat transfer after every compression or expansion stage. The medium-temperature A-CAES with TES maintains the advantage of using off-shelf compressors and it does not need so many heat-exchange processes as the low temperature one [3].

The high-temperature A-CAES with TES can reach maximum storage temperatures of 600°C [4]. This technology was the subject of a European research project in which a new design was developed, called advanced adiabatic compressed air energy storage (AA-CAES) [18]. In the AA-CAES there is an intercooler after the first compression stage with a compression ratio of 2.4. Then, the compression is adiabatic and the final pressure is equal to 65 bar. A scheme of the AA-CAES project is shown in Figure 1.3.

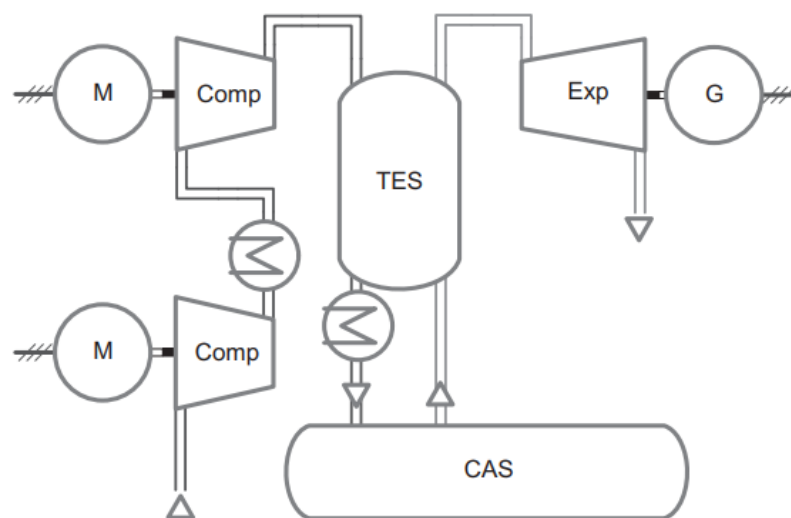


Figure 1.3 – Block diagram of a high-temperature A-CAES as it was designed in the AA-CAES project [3].

The intercooler is necessary because without it the air exiting the turbine during the discharge process would be significantly higher than the ambient one, causing energy losses. So, since an irreversibility is necessary, the best way to deal with it is to waste the thermal energy of the air at the beginning of the compression process, so that the rest of the compression takes

less power. Moreover, the intercooler decouples the storage pressure from the storage temperature: it is possible to control the storage temperature at constant storage pressure, even in off-design conditions, by simply changing the subdivision between the compression ratio before and the one after the intercooler.

Since 2010, this concept has been developed further in the research projects ‘ADELE’ (2010–2013) and ‘ADELEING’ (2013–2017). The major strength of these concepts is their high cycle efficiency, up to 70% [3] [19]. However, the problem is that the high storage temperature presents two issues. First, a high-temperature TES requires special materials as well as complex system engineering. Second, a compressor for such high temperatures is not available and it has to be designed for these types of plants specifically, which is exactly the subject of the present thesis.

1.2.4 UW-CAES

As already discussed, the Huntorf and the McIntosh plants use salt caverns as CAS. These systems are isochoric by nature and their pressure varies with the state of charge of the system. This varying pressure can result in a low efficiency for the compression and the expansion processes due to the deviation from the design point of the turbomachines [20]. Even if the turbine inlet pressure is kept constant using a throttling valve, this throttling process generates irreversibilities that affect the performances. A solution to this problem is represented by an isobaric CAS. The constant pressure can be achieved using a hydrostatic head and the CAES that use this system are called underwater CAES (UW-CAES). So, the acronym UW-CAES specifies just the CAS type and it does not indicate the thermodynamics of the cycle. This means that an UW-CAES can still be a D-CAES, an I-CAES or an A-CAES.

The CAS of an UW-CAES can be built both on-shore and off-shore. An isobaric CAS on-shore can be achieved using closed underground coal mines. These mines can be deep enough that it is possible to produce a hydrostatic head with a reservoir of water on the ground that compensate the pressure inside the mine through a hydrostatic head. Since the water level change in the reservoir is negligible, the pressure of the air trapped inside the mine is constant. To prevent the air from leaking into the surrounding rocks, flexible bags can be used to store it. This idea is interesting in China because there are a lot of coal mines that are going to be closed in the coming years [21].

An UW-CAES can also be developed off-shore. To do so, the CAS system is placed on the seabed (or on the bottom of a lake) at a depth that allows to have the air at the desired pressure. This configuration has two options: just the CAS is placed off-shore and it is connected to the rest of the plant, which is placed on the shores, through a pipeline in which the compressed air flows or all the power plant, with the TES, the compressor and the turbine is placed off-shore. There are two benefits of having all the components but the CAS on land. First, this allows to easily link the storage plant with other renewables sources or with other plants to provide services also for them. Then, it is avoided an expensive floating

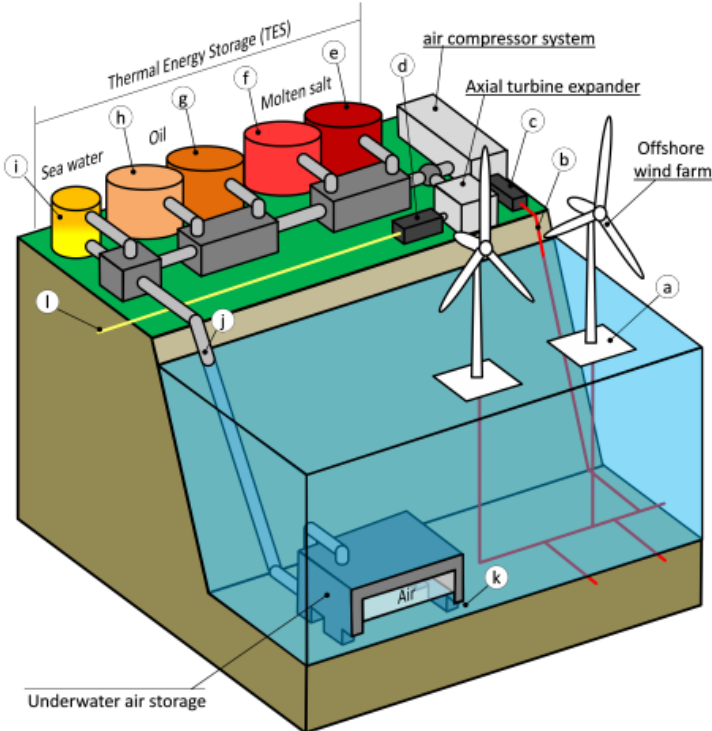
structure able to fit the big amount of thermal fluid and the turbomachines needed [4]. On the other hand, a very long pipeline must be placed on the seabed and the plant performances are damaged by the pressure drop of the air that flows inside it.

1.3 Case Study

The present work is based on the results of the study executed in the thesis “Underwater Compressed Air Energy Storage (CAES): system design optimization, economics and simulation” of Marco Belloli and Adriano Hirn [4]. This previous study designs the entire CAES plant, but it suggests that the analysis done on the compression system should be improved. Since the present work has the target of designing a compression system to be used in the power plant proposed by Belloli and Hirn, it is important to discuss their project first. A scheme of it is proposed in Figure 1.4.

It is an adiabatic CAES with an underwater CAS system that allows to store air at constant pressure. The plant is connected to an offshore wind farm and it has the purpose of storing the energy produced when the wind is abundant and the demand is low and to release that energy when the wind is weak and the demand is high. The CAS system consists in cement air tanks positioned at a depth of about 820 m, at which corresponds a hydrostatic pressure of about 80 bar. The designed electrical power for compression is 75 MW and it is divided into four parallel compression trains to increase the plant flexibility. The analysis of the compression system is based on statistical data, such as the Balje diagram, and it proposes a multistage solution with two shafts and one intercooler. Other solutions with a different number of shafts and intercoolers are studied in their thesis but, in the end, they are rejected. In fact, increasing the number of intercoolers and shafts improves the performances of the compression system, but it also increases the investment cost of the plant.

The maximum temperature of the TES system is 600°C. This very high storage temperature is achieved using in the high temperature TES (600°C – 290°C) molten salts with the following composition: 60% of $NaNO_3$ and 40% of KNO_3 . The medium temperature TES (290°C – 80°C) uses diathermic oil and the low temperature TES (80°C – 30°C) uses sea water. Assuming a minimum temperature difference between the air and the molten salts of 25°C, in their work it is proposed a maximum temperature of the air at the outlet of the compressor of 625°C.



- a. Wind turbine floating platform
- b. Power line from wind farm to CAES
- c. Compressor motor
- d. Generator
- e. Molten salt HT storage
- f. Molten salt LT storage
- g. Oil HT storage
- h. Oil LT storage
- i. Sea water thermocline storage
- j. Compressed air piping
- k. Sea water opening window
- l. Power line from CAES to Grid

Figure 1.4 – Scheme of the CAES plant proposed by Belloli and Hirn [4].

Chapter 2

Multistage Centrifugal Compressor

As explained in the previous chapter, the compression ratio required by the A-CAES power plant studied is very high, so a multistage centrifugal compressor is needed. Moreover, an advantage of the centrifugal compressors compared with the axial ones is their flexibility. This characteristic is very important in a CAES plant since it works often in off-design conditions.

Multistage centrifugal compressors are often used in the Oil & Gas field to compress the natural gas for transportation purposes, for the production of LNG (liquefied natural gas) or for a lot of other applications [6]. This provides a literature background specific for machines of big size, which is something not very common for centrifugal compressors.

2.1 Theoretical Overview

In this section, it is analysed the theory used in the computational procedure to study the centrifugal compressor and the statistical parameters used the most in the technical literature.

2.1.1 Compression Thermodynamics

The main concepts needed to study every component of a stage are illustrated below. The procedure in which they are applied is explained in the sub-section 2.3.1, at the end of this chapter.

First, the main thermodynamic quantities are determined. The specific gas constant R , the isochoric heat capacity c_v , the heat capacity ratio γ and the term ϑ are defined, respectively, in eq. (2.1), (2.2), (2.3) and (2.4).

$$R = \frac{R^*}{MM} \quad (2.1)$$

$$c_v = c_p - R \quad (2.2)$$

$$\gamma = \frac{c_p}{c_v} \quad (2.3)$$

$$\vartheta = \frac{\gamma - 1}{\gamma} \quad (2.4)$$

The inlet thermodynamic quantities required for the analysis are the velocity, the pressure and the temperature (static or total quantities are interchangeable, knowing the velocity). The relationship between total and static quantities are reported in eq. (2.5) and (2.6), respectively, for temperature and pressure.

$$T_{tot} = T + \frac{v^2}{2c_p} \quad (2.5)$$

$$\frac{p_{tot}}{p} = \left(1 + \frac{\gamma - 1}{2} M^2\right)^{\frac{1}{\vartheta}} \quad (2.6)$$

The term M is the Mach number and it is calculated as indicated in eq. (2.7). It can also be computed in the relative frame of reference, using w instead of v .

$$M = \frac{v}{\sqrt{\gamma RT}} \quad (2.7)$$

The link between the isentropic total outlet temperature and the real one is reported in eq. (2.8). The term $\Delta h_{tot,loss}$ stands for the total enthalpy change due to the losses and its calculation is described in Chapter 3.

$$T_{tot,out,real} = T_{tot,out,is} + \frac{\Delta h_{tot,loss}}{c_p} \quad (2.8)$$

To pass from the isentropic total outlet temperature to the total outlet pressure, the equation expressed in eq. (2.9) is used.

$$\frac{p_{tot,out}}{p_{tot,in}} = \left(\frac{T_{tot,out,is}}{T_{tot,in}}\right)^{\frac{1}{\vartheta}} \quad (2.9)$$

The density and the volumetric flow rate are derived from the formulas, respectively, in eq. (2.10) and (2.11).

$$\rho = \frac{p}{RT} \quad (2.10)$$

$$Q = \frac{\dot{m}}{\rho} \quad (2.11)$$

The formulations for the isentropic specific work W_{is} , the Euler's specific work W_{eul} and the actual specific work W_{act} are expressed, respectively, in eq. (2.12), (2.13) and (2.14) [9]. These quantities are related to the single stage compression. It can be noticed that the isentropic work is function of the inlet total temperature, the compression ratio and the thermodynamic properties of the fluid. The Euler's work is function only of the velocity triangles of the impeller. Finally, the actual work is computed as the increase in total enthalpy of the fluid.

$$W_{is} = c_p T_{tot,in} (\beta^\vartheta - 1) \quad (2.12)$$

$$W_{eul} = u_2 v_{u,2} - u_1 v_{u,1} \quad (2.13)$$

$$W_{act} = c_p (T_{tot,out} - T_{tot,in}) \quad (2.14)$$

It is important to study more in detail the difference between these three types of work. The isentropic work is the work required by an ideal compressor, in which there are no energy losses. The Euler's work and the actual work are linked to the isentropic work as reported in eq. (2.15) and (2.16). In these equations, the internal losses $\Delta h_{tot,int}$ and the parasitic losses $\Delta h_{tot,par}$ are introduced. The internal losses are the losses that happen inside the impeller and that affect the flow path in a way that influences the impeller outlet velocity triangle, in fact they impact on the Euler's work as indicated in eq. (2.15). The parasitic losses are losses that do not affect the flow path inside the impeller, but they increase the impeller discharge stagnation enthalpy without any corresponding increase in pressure [9]. The division of the loss mechanisms into internal losses and parasitic losses is executed in Chapter 3.

$$W_{eul} = W_{is} + \sum \Delta h_{tot,int} \quad (2.15)$$

$$W_{act} = W_{is} + \sum \Delta h_{tot,int} + \sum \Delta h_{tot,par} \quad (2.16)$$

Finally, the various efficiencies must be defined. It is important to distinguish between the compression of each single stage and the overall compression of the multistage machine. In fact, the isentropic work of the whole compression, obtained applying the eq. (2.12) to the

multistage compressor, is different from the sum of all the isentropic works of each stage, obtained applying eq. (2.12) to each stage. This is due to the re-heat factor. The single stage isentropic efficiency that is adopted in this work is the one defined in eq. (2.17) [9]. The multistage isentropic efficiency is reported in eq. (2.18). Again, due to the re-heat factor, the $\eta_{is,ms}$ is not the average of the $\eta_{is,ss}$ of all the stages.

$$\eta_{is,ss} = \frac{W_{is,ss}}{W_{act,ss}} \quad (2.17)$$

$$\eta_{is,ms} = \frac{W_{is,ms}}{W_{act,ms}} \quad (2.18)$$

These are the main thermodynamic equations needed to analyse the compression stages, both when the target is the stage design and when it is the study of the off-design conditions.

2.1.2 Air Properties

For the analysis of the present work, the air is considered an ideal gas. This assumption is reasonable for the compression phase because the differences between ideal and real gas increase increasing the pressure and decrease increasing the temperature, as shown in Figure 2.1. For a typical adiabatic compression process starting at ambient temperature, the ideal gas models can be applied up to high pressure because the air heats up during the compression. For this reason, the deviation from the ideal gas model remains acceptable throughout the whole compression process. However, this does not hold if the air is cooled down at high pressure, as done in almost all kinds of CAES plants. In this case, the differences between ideal and real gas models become unacceptable and the ideal gas model cannot be used for accurate technical calculations. In case a study on other components of the CAES is desired, it is suggested to follow the ASME standard for all the parts of the plant that deal with high pressure and low temperature air (i.e., the heat exchanger at the compressor outlet, the one at the turbine inlet and the CAS system). This standard suggests that a model representing an ideal mixture of real gases should be used [3].

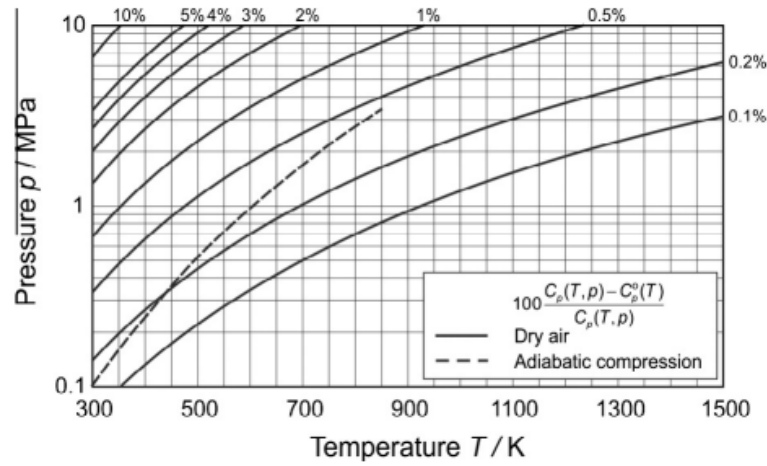


Figure 2.1 – Difference between ideal gas and real gas models. The c_p is used as an example for other thermodynamic properties. [3]

The air is considered dry, so the humidity effects are neglected. This assumption is good for the compression process, but it is suggested to account for the water content in the air in the heat exchanger after the compressor because at high pressure and with the temperature decreasing, condensation can happen. Moreover, during the expansion can be useful to humidify the hot dry air before entering the turbine to increase the mass flow. Doing so, the stored heat is used more efficiently [3].

Since air is analysed as an ideal gas, the specific heat at constant pressure and the dynamic viscosity are function only of the temperature of the air.

In this work, it is assumed the c_p constant for each compression stage. This decision is a trade-off between the computational power and the accuracy of the results. A variable c_p for the compression process would require calculating it every time and having more complex and computational expensive thermodynamic formulas (i.e., the integral formula for the enthalpy). On the other hand, keeping the c_p constant for all the compression would produce a significant error due to the application: in an A-CAES, the compression reaches very high temperatures at which the c_p is significantly different from the one at ambient conditions. So, it is decided to use a constant c_p computed using the inlet total temperature for each stage.

The air is treated as an ideal mix of ideal gases. The computation of c_p^* for each chemical component contained in the air is quantified using the formula reported in eq. (2.19) that uses the numerical values provided by [22] for the specific heat coefficients.

$$c_{p,i}^* = (a_0 + a_1T + a_2T^2 + a_3T^3 + a_4T^4)R^* \quad (2.19)$$

From all the $c_{p,i}^*$ it is possible to calculate the $c_{p,air}^*$ of the air, as described in eq. (2.20). The air composition is assumed to be the one described in Table 2.1. Finally, using the molar mass of the air, the isobaric mass specific heat $c_{p,air}$ is evaluated as described in eq. (2.21).

Nitrogen	78%
Oxygen	21%
Argon	1%

Table 2.1 – Air composition by volume adopted in this work.

$$c_{p,air}^* = 0.78 \cdot c_{p,N_2}^* + 0.21 \cdot c_{p,O_2}^* + 0.01 \cdot c_{p,Ar}^* \quad (2.20)$$

$$c_{p,air} = \frac{c_{p,air}^*}{MM_{air}} \quad (2.21)$$

The term $c_{p,air}$ is the mass specific heat at constant pressure and in the rest of the thesis it is indicated as c_p for simplicity.

The same approach used for the specific heat at constant pressure is adopted for the dynamic viscosity, so it is kept constant during the compression in the stage, but it is computed as function of the temperature at the inlet of each stage. The correlation chosen for the evaluation of the dynamic viscosity is the Sutherland's law reported in eq. (2.22) [23]. The values of the quantities μ_{ref} , T_{ref} and S for the air are reported in Table 2.2.

$$\mu = \mu_{ref} \left(\frac{T}{T_{ref}} \right)^{\frac{3}{2}} \frac{(T_{ref} + S)}{(T + S)} \quad (2.22)$$

Gas	μ_{ref} [Pa · s]	T_{ref} [K]	S [K]
Air	$1.716 \cdot 10^{-5}$	273.15	110.4

Table 2.2 – Values for the reference temperature, for the reference dynamic viscosity at the reference temperature and for the Sutherland constant [23].

2.1.3 Dimensionless Statistical Parameters

The dimensionless parameters are important to have an approximate idea of some quantities of the stage looking at the technical literature. The parameters used in this work are the specific speed ω_s and the specific diameter D_s . Their definition is reported, respectively, in eq. (2.23) and (2.24) [24]. All the quantities are expressed in the international system of units SI.

$$\omega_s = \frac{\omega Q_{in}^{1/2}}{(W_{is})^{3/4}} \quad (2.23)$$

$$D_s = \frac{D_2 W_{is}^{1/4}}{Q_{in}^{1/2}} \quad (2.24)$$

As it can be noted from eq. (2.23), the specific speed is not function of any geometrical quantity of the machine. Its formulation involves the rotational speed of the shaft, the isentropic work and the inlet volumetric flow rate. The isentropic work can be expressed as function of the fluid properties, the compression ratio and the inlet temperature, as expressed in eq. (2.12). The inlet volumetric flow rate can be derived from the mass flow rate and the inlet density, as reported in eq. (2.11). The density is computed as expressed in eq. (2.10). So, to evaluate the specific speed it is sufficient to know the rotational speed, the inlet conditions and the plant requirements, without any information on the stage geometry needed.

Once the specific speed is known, it can be linked to the specific diameter using a statistical diagram, called Cordier diagram and shown in Figure 2.2. It is an average experience curve fitted through a scatter plot and it only serves as an indication of the suitable machine type to select for a given application [24]. Inverting the eq. (2.24), it is possible to compute the outlet diameter of the impeller D_2 from the specific diameter D_s . Doing so, the plant requirements are linked to an approximate dimension of the compression stage. This allows to have a good value for the first iteration of the optimization algorithm.

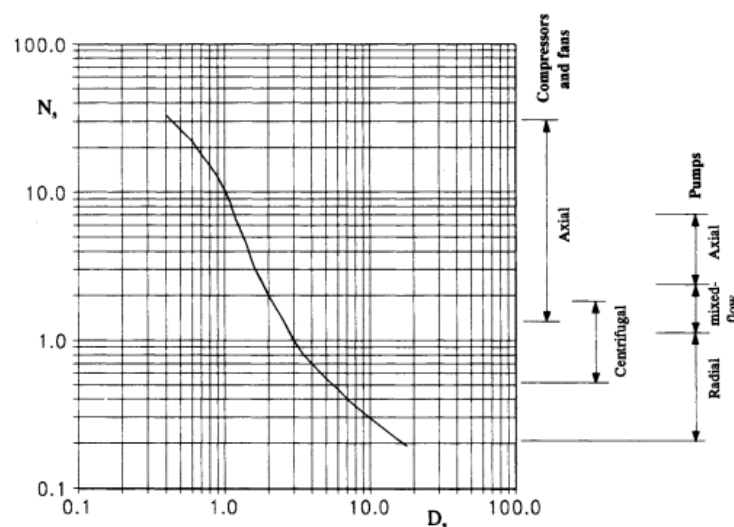


Figure 2.2 – Cordier diagram with the type of machine suggested [24]. N_s is the same quantity as the ω_s indicated in this work.

Two other useful dimensionless parameters are the head coefficient ψ and the flow coefficient φ , defined respectively in eq. (2.25) and (2.26). They provide the same information of ω_s and D_s , but the volumetric flow rate Q and the isentropic work W_{is} are separated each into one single coefficient. Doing so, these coefficients can be used to study the load and the flow rate of a stage with a statistical approach.

The head coefficient describes how much loaded the impeller is. Looking at eq. (2.25) it can be noticed that, for a fixed head coefficient, an increase in the tip speed of the impeller causes an increase in the isentropic work done by that impeller and so in its compression ratio. The flow coefficient, instead, represents how much volumetric flow rate passes through an impeller of fixed dimension and rotational speed. It is useful to classify the various types of impellers.

$$\psi = \frac{W_{is}}{u_2^2} \quad (2.25)$$

$$\varphi = \frac{Q_{in}}{\omega D_2^3} \quad (2.26)$$

2.2 Centrifugal Compressor Components

A centrifugal compressor (or radial compressor) is made of three main components: the impeller (also called rotor), the diffuser (which can be vaneless or vaned) and the volute or the return channel, depending on which stage is considered. The last stage of a multistage centrifugal compressor (or anytime the flow must leave the casing) and the single stage centrifugal compressor have a volute after the diffuser because the flow must be slowed down before entering the outlet duct. The intermediate stages of a multistage centrifugal compressor have a return channel instead of a volute because the kinetic energy can still be exploited in the following stages.

There is also the possibility of adding vanes with an adjustable orientation in the inlet duct before the impeller inlet. These vanes are called variable inlet guide vanes (VIGV) and they are mainly used to improve the off-design operation of the compressor.

2.2.1 Variable Inlet Guide Vanes

The variable inlet guide vanes (VIGV) are the first component that the flow encounters inside the compressor. In this work, the VIGV are the only element that can change its geometry during operation, so they help (together with the regulation of the rotational speed) with the

variation of volumetric flow rate at constant compression ratio, as required by this particular CAES power plant.

They consist in a row of movable axial inlet guide vanes upstream of the impeller that generates gas pre-swirl. This influences primarily the head of the following impeller, according to the Euler's equation reported in eq. (2.13) [5]. The shape of these blades is usually flat, so it has no camber. This allows an easier regulation and a symmetrical behaviour for positive and negative opening angles. A picture of the VIGV is reported in Figure 2.3.

In contrast to axial machines, centrifugal multistage single-shaft compressors cannot be equipped with VIGV ahead of each stage due to an extreme lack of interstage space dictated by the rotodynamic requirements. The maximum number of VIGV rows is two for back-to-back arranged impellers [5], so only the first compression stage of each shaft can be equipped with them.

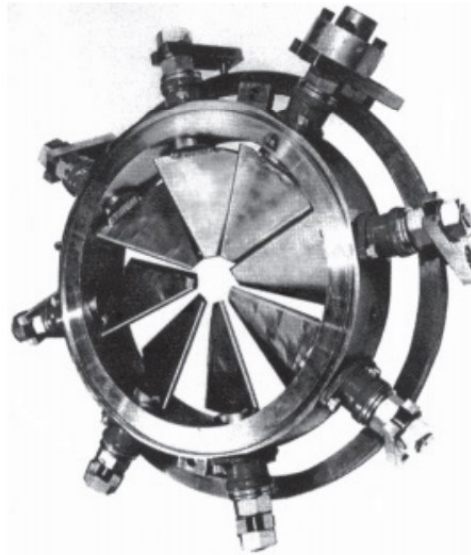


Figure 2.3 – An example of a VIGV system [7].

2.2.2 Impeller

The impeller is the only moving component of the machine, so it is the only one that provides work to the fluid. It is a bladed element and it can have two types of blades: blades that are as long as the impeller and blades that start when the flow curvature becomes high. The blades of the second type are called splitter blades. In the present work, the splitter blades are not considered.

High flow coefficient centrifugal compressors have a 3D geometry: the inlet part of the impeller is axial and it is called inducer. This component has the purpose of guiding the incoming flow while minimizing the losses. After the inducer, there is the conventional

radial part of the impeller. As the flow coefficient decreases, the geometry becomes more 2D, without the presence of an inducer: the impeller develops only in the radial direction [6]. The 3D impellers are characterized by higher efficiency, wider operating range and higher rotational speed. The 2D ones are able to provide a higher compression ratio at equal tip speed and a higher number of stages of this type can fit in a single shaft [5].

Impellers are further divided into two categories: the covered (or shrouded or closed) impellers and the uncovered (or unshrouded or open) impellers. The covered impellers have a layer of metal (cover) applied on top of the blades, which rotates with the impeller itself. The uncovered impellers lack this element, so they have the advantage of allowing a higher tip speed because they do not have the additional centrifugal load provided by the rotating cover. This speed increase allows to have higher volumetric flow rates and compression ratios. 2D impellers are always shrouded and 3D impellers can be shrouded or unshrouded [5].

For the stages of inline multistage centrifugal compressors, the covered impellers are often chosen. The reason for this is that the stages are on the same shaft, so assembly tolerances and long spans between impellers and thrust surfaces result in a high degree of axial motion of the impellers relative to the stationary elements [6]. Moreover, a long shaft is more prone to bending phenomena. In an uncovered impeller, this increases the space between the blade and the upper casing (called clearance gap), degrading the performances. A covered impeller has radial eye seals, so it can shift axially without affecting its performances [6].

In the present work, 3D impellers are used. A picture and the geometry of a 3D impeller used in a multistage inline configuration are reported in Figure 2.4.

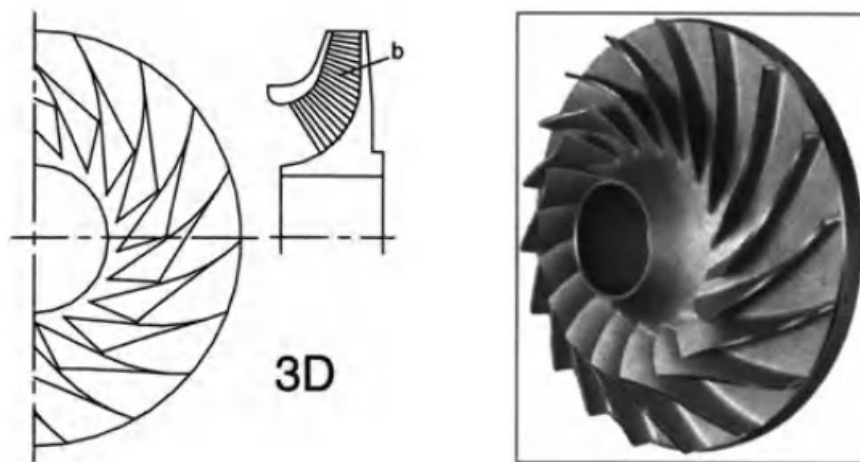


Figure 2.4 – Covered 3D-impeller with twisted backward-curved blades. The photo was taken before the cover was brazed on the impeller [5].

2.2.3 Diffuser

After the impeller, the flow encounters the diffuser which can be of two types: vaned or vaneless. Even a vaned diffuser is always preceded by a vaneless one, which is very short in this case. Its purpose is to allow the flow to mix and to be uniform before entering the vaned diffuser.

A vaned diffuser is more compact and less expensive to build. It also has the advantage of a higher design efficiency, but it lacks flexibility in off-design operation. Since the plant studied in this work must work very often in off-design conditions, a vaneless diffuser is chosen.

A vaneless diffuser consists in two parallel or converging walls forming an open radial passage. A scheme of it is reported in Figure 2.5. The length of the passage cannot be too long because this would make the flow reverse its path and cause instabilities like rotating stall and even surge. This phenomenon happens also when the inlet flow angle (so the angle at the outlet of the impeller) is too high (so too close to the tangential direction). In general, the cause of these instabilities is that the meridional velocity becomes too low to maintain the forward movement of the flow to overcome the adverse radial pressure gradient [5].

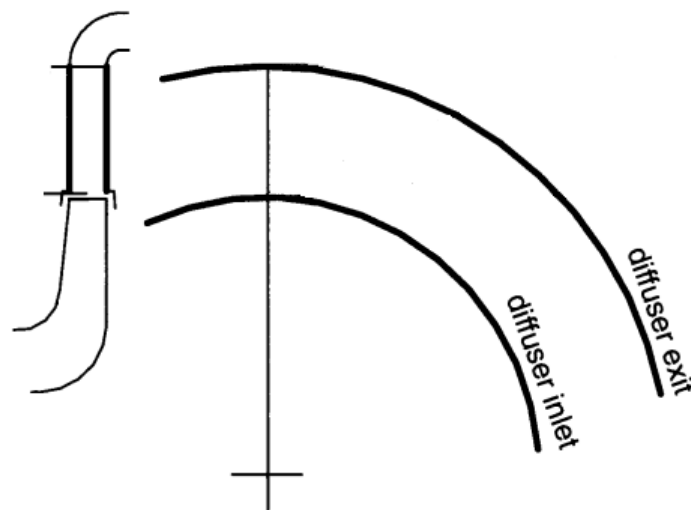


Figure 2.5 – Vaneless diffuser geometry [5].

2.2.4 Volute

In a multistage radial compressor, if the flow must be brought out of the casing for any reason (i.e., intercooling or end of the compression) a volute (also called scroll) or a collector is needed. The difference between the two is that the cross-sectional area of a collector is constant while the one of the volute increases around the circumference, in order to have an almost constant flow velocity inside [10].

Volutes are produced in a lot of different geometries: the cross-section can be circular, elliptical, quadratic or rectangular and all these shapes can be symmetrical, inclined or one-sided offset in relation to the radial direction of the diffuser exit. Also, there are various types of radial developments: the “external” volute is put on top of the diffuser, thus having an increasing centre-of-gravity radius towards the exit. The "central" volute has a centre-of-gravity radius being equal to the diffuser exit radius; and the "internal" volute is wrapped in such a way that its centre-of-gravity radius becomes smaller than the diffuser radius towards the exit [5].

In this work a volute with a circular external geometry is chosen and its shape is shown in Figure 2.6 and in Figure 2.7.

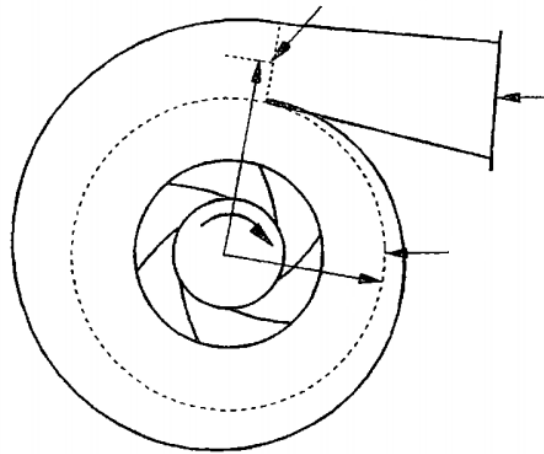


Figure 2.6 – Volute geometry [10].

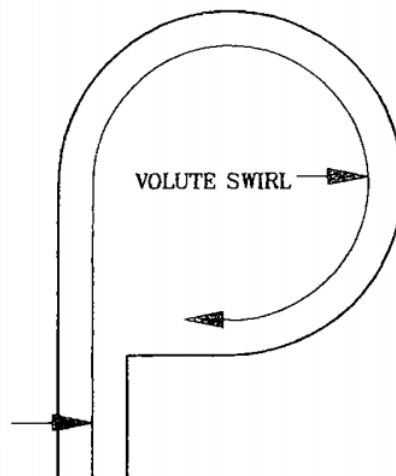


Figure 2.7 – Volute cross section with secondary flow pattern [10].

2.2.5 Return Channel

The return channel is an element used in inline multistage centrifugal compressors to bring the flow exiting from a stage into the next one. It is composed of three parts: an inlet crossover bend, an annular inwards channel and an outlet crossover bend. In the present work, the inlet crossover bend and the outlet crossover bend are also called, respectively, 1st bend and 2nd bend for simplicity. It is important to state that the annular inwards channel can be vaneless in some machines, however in this work it is chosen a vaned annular channel, which is called simply vaned channel.

The inlet crossover bend is a vaneless bend of 180° and it has the function of connecting the diffuser with the vaned channel. Its cross-sectional area is often increased from the diffuser outlet to the vaned channel inlet to compensate for the blade blockage at the vaned channel inlet. The vaned channel has the purpose of reducing the swirl of the flow before it enters the impeller of the following stage. It is a multichannel path consisting of a high-density cascade [5]. The outlet crossover bend is a vaneless bend of 90° that has the scope of connecting the exit of the vaned channel with the following stage inlet. The shape of the entire return channel, with its components highlighted, is shown in Figure 2.8.

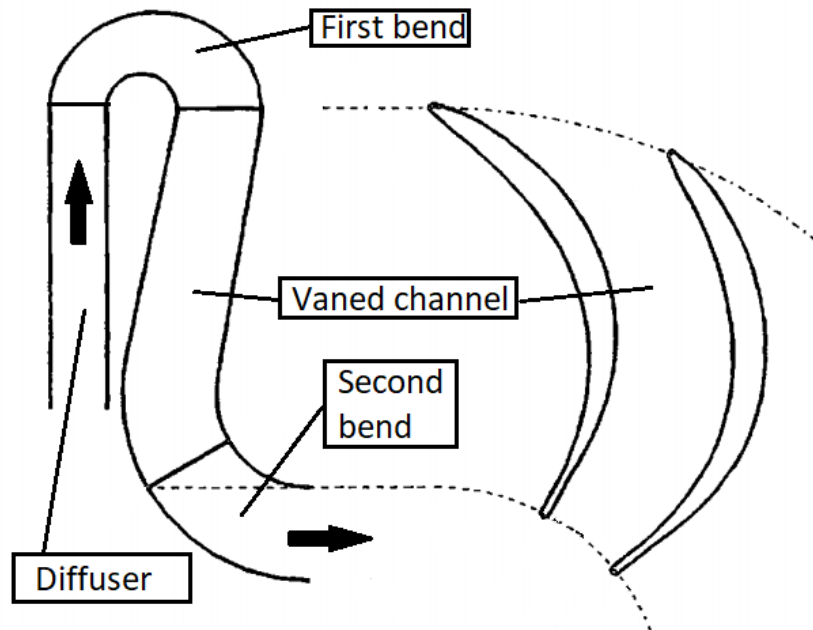


Figure 2.8 – Return channel geometry [10].

2.3 Computational Procedure

The computational fluid dynamics (CFD) consists in the analysis of systems involving fluid flow, heat transfer and associated phenomena such as chemical reactions by means of computer-based simulation. The technique is very powerful and spans a wide range of

industrial and non-industrial application areas. The main reason why CFD lagged behind is the tremendous complexity of the underlying behaviour, which precludes a description of fluid flows that is at the same time economical and sufficiently complete [25]. In the last decades, the computational power available has increased exponentially due to the technological progress of the computing hardware. This allowed the CFD to spread and to be used heavily in engineering applications.

However, during the preliminary design of a complex machine, the variables that must be considered are a lot. So, the use of CFD is still too expensive from the computational point of view to be used to optimize complex machines such as an entire stage of a centrifugal compressor. In this type of processes, the number of iterations needed is very high because a lot of variables are optimized at the same time. The algorithm needs to consider their combinations and it must select the best one, based on a particular objective quantity that often is the final efficiency of the machine. So, the well-established 0D methods are still used for the optimization processes. The 0D methods are simulations that use empirical correlations to quantify the losses in each component analysed. Once the losses are estimated, all the thermodynamic quantities inside the machine can be calculated using thermodynamic equations and averaging both in time and in space (i.e., no turbulence is considered, everything is analysed in the blade-to-blade plane considering just the inlet and outlet quantities). It is evident that the 0D methods are a simplification of the reality, so their accuracy is not very high. For this reason, the result of an optimization analysis executed with 0D methods can be considered a preliminary design that must be further refined using CFD and experimental methods.

In the end, CFD and 0D methods are not used for the same purpose, they are instead complementary. Since in this work a preliminary design of a multistage centrifugal compressor is executed, a 0D model is adopted. This is achieved looking for the best efficiency possible in design operation, taking also into consideration that a high flexibility is needed for this particular application. This aspect is important because a machine can have a high efficiency and stall very easily when the mass flow rate is reduced.

The optimization is done using the software MATLAB: the code searches the maximum efficiency point solving calculations for different combinations of the design variables. The trade-off between the efficiency in design condition and the flexibility is left to the user since it is a delicate work.

2.3.1 Stage Solution

In this sub-section it is described the 0D method built for the present work. However, only the main concepts are illustrated. The most important equations involved in the analysis are explained in the sub-section 2.1.1 and the loss correlations selected are the subject of Chapter 3.

First, the points for each stage are defined in Table 2.3, both for a stage with a volute and for one with a return channel. These points are used in the entirety of the present work, so this

convention is valid for all the chapters. The components used in this work for each stage of the centrifugal compressor are the VIGV (optional), the impeller, the vaneless diffuser (the vaned diffuser is not used due to flexibility issues) and the volute or the return channel (which is composed of the 1st bend, the vaned channel and the 2nd bend).

Name of the point	Position of the point in a stage with a volute	Position of the point in a stage with a return channel
0	Starting point	Starting point
0a	VIGV inlet	VIGV inlet
0b	VIGV outlet	VIGV outlet
1	Impeller inlet	Impeller inlet
2	Impeller outlet / Diffuser inlet	Impeller outlet / Diffuser inlet
3	Diffuser outlet / Volute inlet	Diffuser outlet / 1 st bend inlet
4	NOT USED	1 st bend outlet / Vaned channel inlet
5	Volute outlet / Conical diffuser inlet	Vaned channel outlet / 2 nd bend inlet
6	Conical diffuser outlet	2 nd bend outlet

Table 2.3 – Points and their position for a stage with a volute and for a stage with a return channel.

It must be noticed that the starting point related to point 0 in Table 2.3 stands for the ambient if the stage studied is the first stage, for the intercooler outlet if the stage comes after an intercooler or for the preceding stage outlet for all the other stages. In any case, the conditions of point 0 are provided as inputs. Moreover, point 4 is not used in a stage with a volute, so after point 3 there is point 5. This is to have the same stage outlet point (point 6) both for the volute and for the return channel.

The procedure described below is the one related to the design of the stage. It accepts as input the stage geometry, the compression ratio required, the mass flow rate, the rotational speed of the shaft and the absolute flow angle at the outlet of the impeller α_2 . However, to avoid to over-constrain the problem, some geometric quantities are derived in the procedure and they are not provided as inputs. In case a volute is present, the flow velocity in the outlet pipe is also provided as input.

An outer iteration loop is present on the whole calculation procedure. In fact, the efficiency of the stage for the first iteration is chosen as described in the sub-section 4.1.7 and this outer loop converges on this quantity. Since the efficiency is chosen and the isentropic work can be derived from the compression ratio, also the Euler's work is computed at the start. The Euler's work is involved to define the impeller outlet triangles. Then, for every component of the stage another inner layer of iterations is necessary to converge on its outlet conditions. An iterative method is needed because the density and the velocity are dependent on each

other in every component. In fact, the outlet density is computed from the static pressure and the static temperature, which depend on the velocity. Then, the velocity is function of the density because of the continuity equation (the correct mass flow rate needs to be discharged). Moreover, for all the components but the inlet duct, the losses must be computed. Now, the process to solve every component is illustrated.

Starting from point 0, the losses inside the inlet duct are neglected, so it is possible to compute all the thermodynamic properties of point 0a imposing that the total pressure remains constant. Also, there are no moving parts and so there is no work exchange, so the total enthalpy and, consequently, the total temperature are conserved (the whole machine is assumed adiabatic). The cross-sectional area of the VIGV is bigger than the one of the impeller inlet because it has a bigger diameter and it is a circular section and not an annular one (like the impeller inlet). For this reason, the VIGV meridional velocity is smaller than the one at the impeller inlet.

The same procedure adopted for the inlet duct is applied to the VIGV with the addition of the losses. Doing so, the conditions at point 0b are known.

The losses inside the convergent duct that connects the VIGV to the impeller (so from point 0b to point 1) are neglected. The tangential velocity in point 1 is derived from the conservation of angular momentum and the meridional velocity from the continuity equation.

The impeller is the only component in which the conservation of enthalpy does not hold. In fact, it is a moving component, so it provides work to the fluid. Moreover, in the impeller a lot of loss mechanisms take place. The outlet velocity triangle and the outlet blade height b_2 are computed from the Euler's work and from the angle α_2 , which is provided as an input. The link between the flow angle and the geometric angle of the blades is given by the slip factor as described by eq. (2.27). In this work, the slip factor is quantified applying the Wiesner correlation reported in eq. (2.28) [26].

$$\sigma = 1 - \frac{v_{u,2,\infty} - v_{u,2}}{u_2} \quad (2.27)$$

$$\sigma = 1 - \frac{\sqrt{\cos \beta_{2,g}}}{N_b^{0.7}} \quad (2.28)$$

The definition of the slip factor in eq. (2.27) is based on the difference in the absolute tangential velocity component between the hypothetical case in which the impeller has an infinite number of blades (so that the flow is perfectly guided and its direction corresponds to the geometrical direction of the blades), called $v_{u,2,\infty}$, and the actual one.

In the vanless diffuser, the meridional velocity at the outlet is calculated through the continuity equation, also considering the losses. The tangential velocity, instead, needs to be

derived considering the friction effect of the walls and this is done with the formula reported in eq. (2.29) [8].

$$v_{u,3} = \frac{v_{u,2}}{\frac{D_3}{D_2} + \frac{0.5\pi c_{f,vld} \rho_2 v_{u,2} D_3 (D_3 - D_2)}{\dot{m}}} \quad (2.29)$$

Inside the volute, the flow is considered incompressible due to the low velocities involved. So, the density in point 5 is equal to the one in point 6. Moreover, the outlet cross sectional area is derived from the flow velocity inside the outlet pipe after the conic diffuser, which is provided as input. Also, the area ratio of the conic diffuser is provided as input.

The geometry of the return channel is very complex, so a lot of assumptions are made (they are explained in the sub-section 4.1.3). The 1st bend, the vaned channel and the 2nd bend are analysed as separated components, so the procedure described for a standard component must be applied to all of them to calculate the properties of point 4, point 5 and point 6.

The procedure to study the off-design behaviour of the stages is similar to the one related to the stage design just described. However, since the stage geometry cannot change during off-design conditions (except for the VIGV), it must be fixed to the values found during the design phase. In the off-design analysis the entire geometry is provided as input and the compression ratio becomes an output. Also, in case a volute is present, the flow velocity in the outlet pipe is computed and not anymore imposed because the geometry and the mass flow rate are fixed.

Chapter 3

Loss Correlations

The fluid dynamic losses are computed using empirical and semi-empirical correlations from different authors. In this section, these loss correlations are reported and described. For some of them, the underlying physical phenomena are described, the necessary assumptions are stated and their choice among all the ones provided by the literature is justified. All the losses are expressed in $\frac{J}{kg}$. The losses that are computed with correlations that adopt other units of measure are converted in $\frac{J}{kg}$ anyway. Doing so, it is obtained a set of losses with the same unit of measure so that they are comparable to each other.

The correlations are divided into the main components of each stage: VIGV, impeller, diffuser, volute and return channel and for each component all the types of losses are analysed. The works of various authors are combined in this analysis, obtaining an original set of losses.

The values of some quantities must be assumed. The assumptions made in the present work are reported and explained in the sub-section 4.1.3.

3.1 Variable Inlet Guide Vanes Loss

In the literature, for the loss analysis of the VIGV two main correlations are provided: the one from Galvas and the one from Aungier. The first one adapts a correlation developed for centripetal turbine stators, while the second one is based on axial compressor stages. However, both underestimate the losses at low incidence angles when compared with the experimental results of Coppinger. In particular, the Galvas correlation gives values way below the Coppinger's ones for all the incidence angles [27].

For this reason, in the present work the experimental results of Coppinger are used and an original empirical correlation is produced interpolating the experimental loss values. This correlation is reported in eq. (3.1) and the results of Coppinger [7] are reported in Figure 3.1. Moreover, the third-degree polynomial function resulting from the interpolation is reported in Figure 3.2. It is important to notice that the angle α_1 must be expressed in degrees and not in radians. Since the VIGV analysed in this work have no camber, their behaviour is symmetrical for positive and negative incidence angles. So, the VIGV loss is symmetrical as well and the correlation uses the module on the angle to express this.

The interpolation is executed with the help of the software *ScanIt*, to precisely transform the diagram into numerical points, and of the software Microsoft Excel, to compute the interpolating polynomial. *ScanIt* is a computer program that allows extracting data from scientific graphs, particularly from line and scatter plots [28].

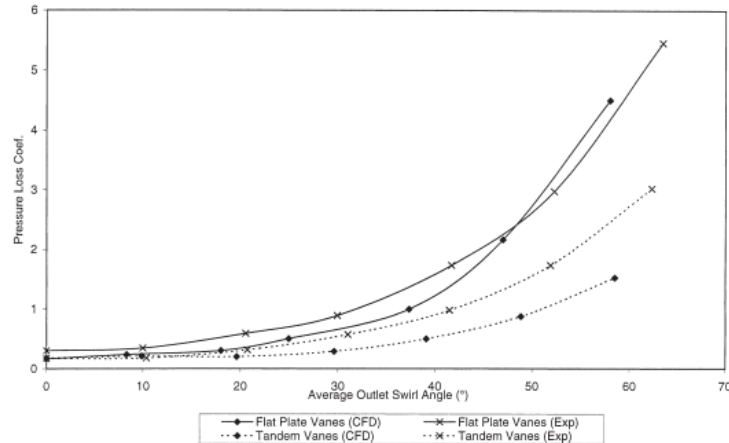


Figure 3.1 – Pressure loss coefficient in function of the VIGV average outlet flow angle [7]. In this work, the experimental results for the flat plate shape are used.

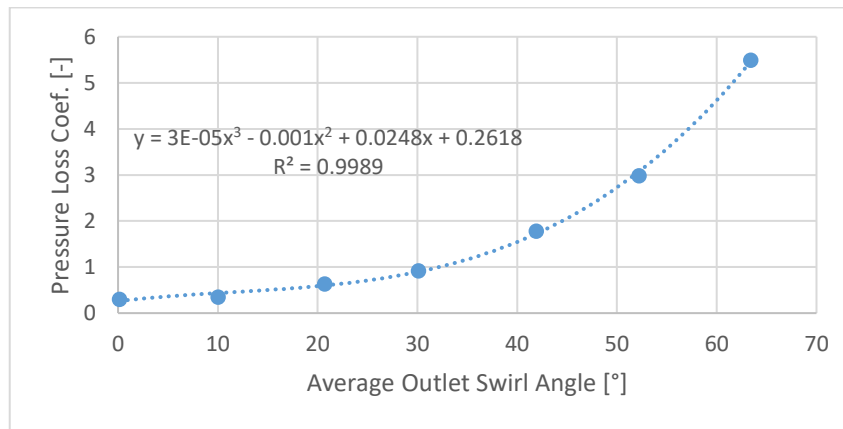


Figure 3.2 – Third-degree polynomial that interpolates the Coppinger's results. The R^2 parameter shows that the experimental data are really close to the model.

$$\Delta p_{tot,VIGV} = (3 \cdot 10^{-5} |\alpha_{0b,deg}|^3 - 0.001 |\alpha_{0b,deg}|^2 + 0.0248 |\alpha_{0b,deg}| + 0.2618) (p_{tot,0a} - p_{0a}) \quad (3.1)$$

Analysing eq. (3.1), it can be noticed that the loss is not null even if the angle α_1 is zero. This means that the VIGV loss is present also in design conditions, but it is at its minimum

value. Starting from the null incidence angle, an increase or a decrease of its value make the VIGV loss increase, following the cubic function.

The result of eq. (3.1) is expressed in total pressure drop because the work of Coppinger expresses the loss as pressure loss coefficient. However, to have all the losses expressed in $\frac{J}{kg}$, the formula reported in eq. (3.2) is applied. It converts the VIGV loss from total pressure drop to total specific enthalpy change. It is function of the thermodynamic properties of the fluid and of the VIGV outlet thermodynamic conditions.

$$\Delta h_{tot,VIGV} = c_p \left(1 - \frac{1}{\left(1 + \frac{\Delta p_{tot,VIGV}}{p_{tot,ob}} \right)^{\vartheta}} \right) T_{tot,ob} \quad (3.2)$$

3.2 Impeller Losses

The flow inside the impeller has a complex behaviour characterized by important secondary flows (flow movements perpendicular to the meridional direction). A secondary flow occurs under the influence of a blade-to-blade static pressure gradient due to both Coriolis forces and the forces imposed by the blade curvature [29]. This complex fluid dynamic scenario makes the study of this component really complicated and a lot of empirical correlations are proposed in the literature.

The method proposed by Aungier [10] considers 11 loss mechanisms for the internal losses and 3 for the parasitic losses, for a total of 14 loss mechanisms to evaluate the performances of the impeller alone. However, this analysis requires a lot of data about the specific machine and a more general approach is preferred, since the target of the present work is a preliminary design. In the work of Oh et al. [9], the optimum set of losses for the impeller includes 8 loss mechanisms. This approach is the one followed in the present work, even if the correlations used for these loss mechanisms are not always the same indicated in that work.

Moreover, the focus of this thesis is on an efficient and not highly loaded machine, so there are no issues of supersonic flows. For this reason, the correlation relative to the supersonic losses is not needed in the first place.

The impeller losses are divided into two categories: the internal losses and the parasitic losses. The thermodynamic impact of these two different categories of losses is described in the sub-section 2.1.1. Here they are just classified. The losses caused by incidence, blade loading, skin friction, clearance and mixing are classified as internal losses. The losses caused by leakage, disk friction and recirculation are classified as parasitic losses.

3.2.1 Incidence Loss

This loss mechanism considers the adjustment of the flow to the angle of the blade at the inlet of the inducer. The fluid in close proximity to the blade instantly experiences a speed change to follow the inlet angle of the blade. When the fluid separation occurs, losses are generated in association with this phenomenon [30]. This loss mechanism is present in every bladed element, so it is computed also in the vaned channel of the return channel (sub-section 3.5.2). It is also important to notice that there is a flow angle, called $\beta_{1,opt,mid}$, for which there is no incidence loss: this is the optimal angle and it is the design one. The consequence is that this loss mechanism is active only for the flow angles different from the design one, so in off-design operation.

For this mechanism it is adopted the correlation of Galvas reported in the eq. (3.3) [8].

$$\Delta h_{tot,inc} = \frac{w_{1,mid}^2 \sin^2 (|\beta_{1,f,mid} - \beta_{1,opt,mid}|)}{2} \quad (3.3)$$

The physical meaning of this correlation is that the kinetic energy associated with the change in relative tangential velocity is converted into internal energy, which manifests itself as an increase in temperature [8]. In fact, the numerator of the eq. (3.3) is the square power of the relative velocity component normal to the optimum direction. This strong physical meaning is the reason why this correlation is chosen in the present work. It must be noticed that the quantities involved are the ones at the mean diameter.

3.2.2 Blade Loading Loss

This loss is developed due to the negative gradient of the velocity in the boundary layers. Such deceleration increases the thickness of the boundary layer itself, leading to flow separation [30]. This loss mechanism is described by the Coppage correlation [9] reported in eq. (3.4).

$$\Delta h_{tot,bl} = 0.05 D_f^2 u_2^2 \quad (3.4)$$

This correlation is widely adopted in the technical literature and there are few alternatives. One of them is a correlation proposed by Aungier [10] but, as already explained, this author uses a different approach to estimate the impeller losses.

The term D_f , used in eq. (3.4), is the diffusion factor and it has the formulation reported in eq. (3.5) [9].

$$D_f = 1 - \frac{w_2}{w_{1,tip}} + \frac{0.75W_{eul}/u_2^2}{\left(\frac{w_{1,tip}}{w_2}\right) \left[\left(\frac{N_b}{\pi}\right) \left(1 - \frac{D_{1,tip}}{D_2}\right) + \frac{2D_{1,tip}}{D_2}\right]} \quad (3.5)$$

It is important to notice that D_f is function of the number of blades of the impeller N_b . In fact, with all the other variables fixed, the loss in eq. (3.4) decreases increasing N_b because the load on each single blade diminishes.

3.2.3 Skin Friction Loss

The action of shearing forces on the walls of the impeller due to the turbulent fluid friction generates the skin friction loss [30]. To estimate this loss mechanism, it is used the Jansen correlation reported in the eq. (3.6) [9].

$$\Delta h_{tot,sf} = 2c_{f,imp} \frac{L_b}{D_{hyd,imp}} \bar{w}^2 \quad (3.6)$$

All the new terms introduced by the eq. (3.6) are explained below.

The term \bar{w} in eq. (3.6) is the average relative velocity inside the impeller computed with a particular weighted average, expressed in eq. (3.7).

$$\bar{w} = \frac{v_{1,tip} + v_2 + w_{1,tip} + 2w_{1,hub} + 3w_2}{8} \quad (3.7)$$

The $D_{hyd,imp}$ in eq. (3.6) is the hydraulic diameter of the impeller and it is computed as an average between the hydraulic diameter at the inlet of the impeller and the one at the outlet, as reported in eq. (3.8).

$$D_{hyd,imp} = \frac{D_{hyd,1} + D_{hyd,2}}{2} \quad (3.8)$$

The terms $D_{hyd,1}$ and $D_{hyd,2}$ in eq. (3.8) are computed from the definition of hydraulic diameter, expressed in eq. (3.9). The term P in this case is the wetted perimeter.

$$D_{hyd} = \frac{4A}{P} \quad (3.9)$$

The term L_b used in eq. (3.6) is the blade length and it is estimated by the formula in eq. (3.10) proposed by Jansen [31].

$$L_b = \frac{\pi}{8} \left(D_2 - \frac{D_{1,tip} + D_{1,hub}}{2} - b_2 + 2L_{ax} \right) \left(\frac{2}{\frac{\cos \beta_{1,g,tip} + \cos \beta_{1,g,hub}}{2} + \cos \beta_{2,g}} \right) \quad (3.10)$$

The term $c_{f,imp}$ in eq. (3.6) is the friction coefficient inside the impeller and it is calculated with the formula in eq. (3.11) [11].

$$c_{f,imp} = c_f + 0.0015 \quad (3.11)$$

Finally, the term c_f in eq. (3.11) is the friction coefficient of a simple duct. It can be derived from the Colebrook equation [32] reported in eq. (3.12) using the quantities of the impeller. The Colebrook equation must be solved iteratively.

$$\frac{1}{\sqrt{c_f}} = -2 \log_{10} \left(\frac{Ra}{3.71 D_{hyd}} + \frac{2.51}{Re \sqrt{c_f}} \right) \quad (3.12)$$

3.2.4 Clearance Loss

Only in an uncovered impeller there is an actual clearance loss. In covered impellers, the blades and the cover are a unique piece of metal, which means that there is no gap between them and so no clearance loss.

The clearance loss considers the flow escaping from the gap between the blades and the outer casing of the compressor, from the pressure side to the suction side of the blade [30]. This flow undergoes a sudden contraction and a subsequent expansion across the clearance gap and this process affects both the clearance flow and the main flow into which it discharges. This loss mechanism becomes important for low specific speed stages [31].

The clearance loss is computed using the Jansen correlation [9] expressed in eq. (3.13). The pressure difference acting across the clearance gap is estimated from an assumed characteristic blade loading and the total pressure losses are obtained by assigning standard loss factors to the sudden contraction and sudden expansion processes [31]. The term ε_{cl} is the clearance gap.

$$\Delta h_{tot,cl} = 0.6 \frac{\varepsilon_{cl}}{b_2} v_{u,2} \left\{ \frac{4\pi}{b_2 N_b} \left[\frac{r_{1,tip}^2 - r_{1,hub}^2}{(r_2 - r_{1,tip}) \left(1 + \frac{\rho_2}{\rho_1} \right)} \right] v_{u,2} v_{1,mid} \right\}^{\frac{1}{2}} \quad (3.13)$$

A consideration to avoid confusion is required. In the sub-section 3.2.6, the leakage loss calculation for open impellers involves the clearance mass flow. That clearance mass flow is computed using the Aungier method because the entire leakage loss (which is where that clearance flow is used) is evaluated with that method. However, the clearance loss computed in eq. (3.13) does not involve the Aungier method in any way.

3.2.5 Mixing Loss

This loss mechanism accounts for the mixing of low-momentum flow with the core flow at the outlet of the impeller [10]. The low-momentum flow exiting the impeller is called wake and it is located on the suction side of the blade while the high-momentum flow is located on the pressure side and it is called jet. The mixing loss is described by the Johnston and Dean correlation, which is reported in eq. (3.14). The term b^* is the ratio of vaneless diffuser inlet width to impeller exit width and the initial enlargement caused by the disk and cover thickness is neglected. The term ε_{wake} is the wake fraction of the blade-to-blade space [9].

To use this correlation, it is necessary to assume a simple “square-wave” velocity profile, in which the relative velocities of the wake and the jet portion of the flow are uniform inside their respective flow portion. Moreover, the static pressure must be assumed constant along the impeller outlet, the number of impeller blades must be high ($N_b \geq 10$) and the relative velocity in the wake must be considered negligible [33].

$$\Delta h_{tot,mix} = \frac{1}{1 + \tan^2 \alpha_2} \left(\frac{1 - \varepsilon_{wake} - b^*}{1 - \varepsilon_{wake}} \right)^2 \frac{v_2^2}{2} \quad (3.14)$$

3.2.6 Leakage Loss

The leakage mechanism is different in uncovered impellers with respect to covered ones. For an uncovered impeller it consists in the fluid flowing in the gap between the blade and the casing that returns to the impeller inlet and it is reenergized. So, this flow is a portion of the clearance flow, only the fraction that goes back to the impeller inlet. For a covered impeller, the leakage flow is the flow through the gap between the impeller cover and the casing. To limit this flow, a labyrinth eye seal is usually employed. This portion of fluid returns to the impeller inlet and it is reenergized [10].

For an uncovered impeller, it is adopted the Aungier correlation as reported in eq. (3.15). This correlation assumes that the portion of the clearance flow that goes back to the impeller inlet is half of it. This assumption is empirical and it is derived from experimental results [10].

$$\Delta h_{tot,leak} = \frac{\dot{m}_{cl} u_{cl} u_2}{2\dot{m}} \quad (3.15)$$

The clearance flow velocity u_{cl} and the clearance mass flow rate \dot{m}_{cl} are computed as indicated, respectively, in eqs. (3.16) and (3.17).

$$u_{cl} = 0.816 \sqrt{\frac{2\Delta p_{cl}}{\rho_2}} \quad (3.16)$$

$$\dot{m}_{cl} = \rho_2 N_b \varepsilon_{cl} u_{cl} L_m \quad (3.17)$$

The pressure difference across the blade surfaces Δp_{cl} and the meridional length of the impeller L_m , used in eqs. (3.16) and (3.17), are calculated as reported, respectively, in eqs. (3.18) and (3.19). To compute L_m , it is assumed that the meridional shape of the compressor is an arc of ellipse [34]. So, in the eq. (3.19) is reported the approximated formula to compute a quarter of the perimeter of an ellipse having the impeller axial length L_{ax} and the impeller radial length L_{rad} as semiaxis.

$$\Delta p_{cl} = \frac{\dot{m}(r_2 v_{u,2} - r_{1,mid} v_{u,1,mid})}{N_b \bar{r} \bar{b} L_m} \quad (3.18)$$

$$L_m = \frac{1}{2} \pi \sqrt{\frac{L_{rad}^2 + L_{ax}^2}{2}} \quad (3.19)$$

The terms \bar{r} and \bar{b} used in eq. (3.18) are calculated as reported, respectively, in eqs. (3.20) and (3.21).

$$\bar{r} = \frac{r_{1,mid} + r_2}{2} \quad (3.20)$$

$$\bar{b} = \frac{b_1 + b_2}{2} \quad (3.21)$$

The impeller radial length L_{rad} used in eq. (3.19) is defined as expressed in eq. (3.22).

$$L_{rad} = \frac{D_2 - D_{1,mid}}{2} \quad (3.22)$$

For a covered impeller, it is adopted the correlation expressed in eq. (3.23) to compute the leakage flow [11]. The term N_{leak} stands for the number of teeth inside the labyrinth seal and S_{leak} is the annular area available for the flow to leak through and it is computed as reported in eq. (3.24). Its formulation involves the inlet tip diameter because the seal is positioned between the cover and the casing at the impeller inlet and its diameter is almost equal to $D_{1,tip}$. The term ε_{leak} is the gap between the seal teeth and the other surface and the term C_D is a coefficient that depends on the geometrical shape of the labyrinth seal (see Figure 4.2).

$$\dot{m}_{leak} = C_D S_{leak} \rho_1 \sqrt{\frac{2\Delta h_{is}}{N_{leak}}} \quad (3.23)$$

$$S_{leak} = \pi D_{1,tip} \varepsilon_{leak} \quad (3.24)$$

Once the leakage flow is known, the leakage loss must be derived. Continuing to follow the Aungier method, the leakage loss in a covered impeller is quantified as expressed in eq. (3.25). This formula expresses the direct proportionality between the leakage loss, the Euler's work and their respective mass flows involved. This simply accounts for the fact that the leakage flow is worked on by the impeller a second time [10].

$$\Delta h_{tot,leak} = \frac{\dot{m}_{leak} W_{eul}}{\dot{m}} \quad (3.25)$$

3.2.7 Disk Friction Loss

The disk friction is generated by adhesive forces between the rotating disk and the fluid in the surrounding enclosure. The induced flows depend on the geometry of the impeller and on the one of its enclosure [30]. If the impeller is covered, these forces are applied also on the cover. To compute this loss, it is necessary to compute the friction coefficient of both disk and cover. To accomplish this, in this work it is adopted the method used by Aungier integrated with some further assumptions.

The friction coefficient is calculated starting from the method of Daily and Nece, which considers rotating disks in a housing. In the present work, it is assumed that the Reynolds number is high enough to be in the regime of "fully rough" disk. In this regime, the friction coefficient is not anymore dependent on the Reynolds number but it depends only on the

roughness of the surfaces and on the geometry of the machine, as expressed in eq. (3.26) [10]. The term ε_{disk} is the gap between the disk or the cover and the casing.

$$\frac{1}{\sqrt{c_{f,ideal\ disc}}} = 3.8 \log_{10} \left(\frac{r_2}{R_a} \right) - 2.4 \left(\frac{\varepsilon_{disk}}{r_2} \right)^{0.25} \quad (3.26)$$

Once the eq. (3.26) is solved in the variable $c_{f,ideal\ disc}$, Aungier proposes some empirical correction to account for the leakage flow. The correction expressed in eq. (3.27) quantifies the friction coefficient of the impeller $c_{f,df}$ and it is supported by the accurate work input predictions that provides for ultralow flow coefficient stages, where leakage and disk friction losses are very high [10]. The definitions of the parameters K_0 and K involved in the eq. (3.27) are reported, respectively, in the eqs. (3.28) and (3.29).

$$c_{f,df} = c_{f,ideal\ disc} \frac{(1 - K)^2}{(1 - K_0)^2} \quad (3.27)$$

$$K_0 = \frac{0.46}{1 + \frac{\varepsilon_{disk}}{r_2}} \quad (3.28)$$

$$K = K_0 + C_q (1.75K_f - 0.316) \frac{r_2}{\varepsilon_{disk}} \quad (3.29)$$

The expressions for the terms C_q and K_f are reported, respectively, in eqs. (3.30) and (3.31).

$$C_q = \frac{\dot{m}_{leak} \left(\frac{\rho_2 r_2 u_2}{\mu} \right)^{\frac{1}{5}}}{2\pi \rho_2 r_2^2 u_2} \quad (3.30)$$

$$K_f = \frac{v_{u,2}}{u_2} \quad (3.31)$$

The expression of K_f reported in (3.31) is valid if the leakage flow moves from the outlet to the inlet of the impeller.

The leakage mass flow \dot{m}_{leak} must be known both in the cover-casing gap and in the disk-casing gap to be able to apply this method. The leakage mass flow in the cover-casing gap is the same one computed for the leakage loss in the case of a covered impeller. The leakage mass flow in the disk-casing gap is more case-dependent. In fact, it depends on the specific geometry of the compressor, on its operating condition and on the seals used. Since the

working fluid is air (so it is neither toxic nor dangerous), it is likely that the leakage flow goes out from the machine into the surrounding environment, passing through the shaft labyrinth seals. So, it is possible to quantify this leakage mass flow rate knowing the specific geometry of the machine and the shaft seal used. However, in the present work the leakage mass flow in the disk-casing gap is neglected.

Once the impeller friction coefficient $c_{f,df}$ is known, the friction coefficient of the disk $c_{f,df,disk}$ and the one of the eventual cover $c_{f,df,cov}$ can be evaluated. Their definitions are reported, respectively, in eqs. (3.32) and (3.33). These new friction coefficients are an adjustment of the impeller friction coefficient $c_{f,df}$. The constant 0.75 is an empirical factor derived from the experimental results of other studies. It must be noted that in the work of Daily and Nece the friction coefficient refers to both sides of the disk, so the use of the factor 0.75 implies a friction coefficient about 50% higher than the one of the Daily and Nece work. The friction coefficient of the cover $c_{f,df,cov}$ also includes a correction for the different surface area of the cover relative to that of a flat disk [10].

$$c_{f,df,disk} = 0.75c_{f,df} \quad (3.32)$$

$$c_{f,df,cov} = 0.75L_m c_{f,df} \frac{1 - \left(\frac{D_{1,tip}}{D_2}\right)^5}{r_2 - r_{1,mid}} \quad (3.33)$$

In the end, the disk friction coefficient of the disk $c_{f,df,disk}$ and the disk friction coefficient of the cover $c_{f,df,cov}$ are the ones involved in the definition of the disk friction loss, as explained in eq. (3.34). In the case of an open impeller, the term $c_{f,df,cov}$ in this correlation is set equal to zero.

$$\Delta h_{tot,df} = \frac{(c_{f,df,disk} + c_{f,df,cov})\rho_2 r_2^2 u_2^3}{2\dot{m}} \quad (3.34)$$

3.2.8 Recirculation Loss

In a centrifugal compressor, there is a recirculation of low momentum fluid from the vaneless diffuser inlet into the impeller outlet. This phenomenon is considered by the recirculation loss. For this loss mechanism, it is chosen the Coppage correlation reported in eq. (3.35) [8]. The term D_f is the diffusion factor and it is defined in eq. (3.5).

$$\Delta h_{tot,rec} = 0.02 \tan \alpha_2 D_f^2 u_2^2 \quad (3.35)$$

In the eq. (3.35) it can be noticed that as the impeller discharge flow angle becomes large, the loss becomes increasingly significant [8].

Other possible correlations provided by the literature are the Jansen's version of the Coppage correlation, which is equal but uses $\sqrt{\tan \alpha_2}$ instead of $\tan \alpha_2$, the Aungier correlation and the Oh correlation that involves the use of $\sinh 3.5\alpha_2^3$ instead of $\tan \alpha_2$. However, the Aungier correlation presents a physically unrealistic abrupt change at the stall point in the recirculation loss prediction [9]. Moreover, for high values of α_2 the Jansen's version of the Coppage correlation underestimates the loss while the Oh correlation overestimates them. For these reasons, the Coppage correlation reported in eq. (3.35) is chosen for the present work.

3.3 Vaneless Diffuser Loss

The loss phenomenon inside the vaneless diffuser is only due to the friction loss. This loss is computed using the Coppage correlation reported in eq. (3.36) [8].

$$\Delta h_{tot,vld} = \frac{c_{f,vld} r_2 \left(1 - \left(\frac{r_2}{r_3}\right)^{1.5}\right) v_2^2}{1.5 b_2 \cos \alpha_2} \quad (3.36)$$

The term $c_{f,vld}$ in eq. (3.36) is computed using the Japikse correlation expressed in eq. (3.37) [8]. The quantity k can range between 0.005 and 0.02, but usually it has the value of 0.01.

$$c_{f,vld} = k \left(\frac{1.8 \cdot 10^5}{Re_{vld}} \right)^{0.2} \quad (3.37)$$

3.4 Volute Losses

The volute is applied after the vaneless diffuser every time it is needed to bring the flow outside of the inline configuration. In this work, this happens in the stage before an intercooler and in the last stage of a shaft.

To compute the losses of this component, it is used the method proposed by Aungier which starts from the analysis of Weber and Koronowski [10]. This method is designed for a volute with a circular external geometry [5]. It divides the losses into 4 different mechanisms that in this work are called meridional velocity loss, tangential velocity loss, skin friction loss and exit cone loss. These mechanisms are described below.

It is important to state that the Aungier's method works in terms of total pressure losses. To have the same unit of measure used for the other loss mechanisms in the compressor, in this work the losses expressed in total pressure drops by Aungier are converted into total specific enthalpy changes, as it is done for the VIGV loss. This is obtained applying the formula reported in eq. (3.38) which reports the conversion from a generic volute loss expressed in terms of total pressure drop into a generic volute loss expressed in terms of total specific enthalpy loss. This is the same formula reported in eq. (3.2), but in this case it is applied to the volute.

$$\Delta h_{tot,vol} = c_p \left(1 - \frac{1}{\left(1 + \frac{\Delta p_{tot,vol}}{p_{tot,6}} \right)^{\vartheta}} \right) T_{tot,6} \quad (3.38)$$

3.4.1 Meridional Velocity Loss

It is very difficult for a volute to recover the incoming meridional velocity. This velocity, in a volute with a circular external geometry, becomes a “swirl” component within the volute passage and it is eventually dissipated in the downstream pipe. So, the loss associated to this mechanism considers a complete loss of the meridional velocity head. This is expressed in eq. (3.39) [10].

$$\Delta p_{tot,mer} = \left(\frac{v_{m,3}}{v_3} \right)^2 (p_{tot,3} - p_3) \quad (3.39)$$

The total pressure loss resulting from eq. (3.39) is converted into specific enthalpy applying the eq. (3.38).

3.4.2 Tangential Velocity Loss

The ideal condition for a volute is to collect the flow while conserving the angular momentum. If the area and mean radius variation in the circumferential direction forces a change in the angular momentum, some portion of the tangential velocity head can be expected to be lost. This loss mechanism is computed using the correlation expressed in eq. (3.40) [10], which has two formulations depending on the volute sizing parameter SP . This parameter is defined as expressed in eq. (3.41) and its optimal value is 1.

$$\begin{aligned}\Delta p_{tot,tang} &= \frac{1}{2} \frac{D_3 v_{u,3}^2}{D_5 v_3^2} \left(1 - \frac{1}{SP^2}\right) (p_{tot,3} - p_3); & SP \geq 1 \\ \Delta p_{tot,tang} &= \frac{D_3 v_{u,3}^2}{D_5 v_3^2} \left(1 - \frac{1}{SP}\right)^2 (p_{tot,3} - p_3); & SP < 1\end{aligned}\quad (3.40)$$

$$SP = \frac{D_3 v_{u,3}}{D_5 v_5} \quad (3.41)$$

The total pressure loss resulting from eq. (3.40) is converted into specific enthalpy applying the eq. (3.38).

3.4.3 Skin Friction Loss

Like in every component of a fluid machine, inside the volute there is a loss due to fluid friction against the walls. This loss is calculated as reported in eq. (3.42) [10].

$$\Delta p_{tot,fr} = 4c_{f,vol} \left(\frac{v_5}{v_3}\right)^2 \frac{L_{vol}}{D_{hyd,vol}} (p_{tot,3} - p_3) \quad (3.42)$$

The average path length for the flow inside the volute L_{vol} and the hydraulic diameter $D_{hyd,vol}$ are defined as reported, respectively, in eq. (3.43) and (3.44). The friction coefficient $c_{f,vol}$ is computed applying the Colebrook equation expressed in eq. (3.12) to the volute.

$$L_{vol} = \frac{\pi(r_3 + r_5)}{2} \quad (3.43)$$

$$D_{hyd,vol} = \sqrt{\frac{4A_5}{\pi}} \quad (3.44)$$

The total pressure loss resulting from eq. (3.42) is converted into specific enthalpy applying the eq. (3.38).

3.4.4 Exit Cone Loss

This loss occurs because after the volute there is a conical diffuser. This component has two purposes: it connects the volute with the outlet pipe and it helps to reduce the flow speed, recovering a little amount of static pressure. This further diffusion leads to a loss, which is

the exit cone loss and it is computed as indicated in eq. (3.45). The value obtained from this correlation is substantially greater than the one used by Weber and Koronowski because in their work the exit cone is assumed to be an optimized ideal conical diffuser. Considering the distorted flow entering the exit cone and the transition from a swirling annular flow to a linear flow path, that assumption is judged too optimistic [10].

$$\Delta p_{tot,ec} = \left(\frac{v_5 - v_6}{v_3} \right)^2 (p_{tot,3} - p_3) \quad (3.45)$$

The total pressure loss resulting from eq. (3.45) is converted into specific enthalpy applying the eq. (3.38).

3.5 Return Channel Losses

The return channel is divided into three components. In this work, they are called 1st bend, vaned channel and 2nd bend.

The 1st bend is a vaneless passage with a 180° bending that connects the outlet of the vaneless diffuser with the inlet of the vaned channel. It reverses the direction of the flow, from an outward direction to an inward one. The vaned channel reduces the tangential component of the velocity in order to have a limited swirl at the inlet of the following stage. It also recovers a portion of the kinetic energy, increasing the static pressure. The 2nd bend is a vaneless passage with a 90° bending and it is necessary to connect the outlet of the vaned channel with the inlet of the following compression stage.

The losses inside these three components are analysed in this section.

3.5.1 First Bend Losses

The losses inside this component are computed applying the model of a vaneless annular passage proposed by Aungier [10]. This model includes two different loss mechanisms: the loss related to the diffusion process and the one related to the curvature.

To compute the diffusion loss, some parameters need to be defined. The formulations for the divergence parameter D and for D_{max} are reported, respectively, in eq. (3.46) and (3.47). These formulations are the adjustment of the work of Reneau et al. for a centrifugal compressor [10]. The derivative used in eq. (3.46) is quantified in eq. (3.48), assuming a constant velocity decrease along the bend.

$$D = - \frac{\bar{b} dv}{\bar{v} dm} \quad (3.46)$$

$$D_{max} = 0.4 \left(\frac{b_3}{L_{bend1}} \right)^{0.35} \cos \alpha_3 \quad (3.47)$$

$$\frac{dv}{dm} = \frac{v_4 - v_3}{L_{bend1}} \quad (3.48)$$

At this point, the empirical diffusion efficiency E_{bend1} is defined, depending on the value of D , in eq. (3.49).

$$\begin{aligned} E_{bend1} &= 1; & D &\leq 0 \\ E_{bend1} &= 1 - 0.2 \left(\frac{D}{D_{max}} \right)^2; & 0 < D < D_{max} \\ E_{bend1} &= 0.8 \sqrt{\frac{D_{max}}{D}}; & D &\geq D_{max} \end{aligned} \quad (3.49)$$

Then, it is introduced in eq. (3.50) the maximum outlet height that does not produce stall in the annular passage. The eq. (3.50) is a simplified version of the general formula that uses the area instead of the height, as shown in (3.65). This simplification is possible because this passage has a 180° bending and the inlet radius is equal to the outlet one.

$$b_{max,bend1} = b_3 \left(1 + \frac{0.16L_{bend1}}{b_3} \right) \quad (3.50)$$

Finally, the diffusion loss is computed in eq. (3.51) and (3.52). The value chosen between the two resulting from eq. (3.51) and (3.52) depends on whether the outlet passage height is higher or lower of $b_{max,bend1}$, which is the maximum stall free height. If $b_4 \leq b_{max,bend1}$ there is no stall in the annular passage and the diffusion loss is the result of the correlation reported in eq. (3.51). If $b_4 > b_{max,bend1}$ there is stall and the diffusion loss is the maximum value between the results of eq. (3.51) and eq. (3.52).

$$\Delta h_{tot,diff} = -2(\overline{p}_{tot} - \bar{p})(1 - E_{bend1}) \frac{1}{\bar{\rho} \bar{v}} (v_4 - v_3) \quad (3.51)$$

$$\Delta h_{tot,diff} = 0.65(\overline{p}_{tot} - \bar{p}) \frac{\left(1 - \frac{b_{max,bend1}}{b_4} \right)}{\bar{\rho}} \quad (3.52)$$

The curvature loss is quantified using the correlation reported in eq. (3.53). The term κ_m is the streamline curvature (the reciprocal of the radius).

$$\Delta h_{tot,curv} = \frac{\kappa_m (\overline{p_{tot}} - \bar{p}) \overline{v_m}}{13 \bar{\rho} \bar{v}} \quad (3.53)$$

3.5.2 Vaned Channel Losses

This component is analysed applying the method proposed by Aungier [10]. This method includes four loss mechanisms: the incidence loss, the skin friction loss, the blade loading loss and the mixing loss. For the incidence loss, it is applied the Galvas correlation [8] instead of the Aungier's one because it has more physical meaning and it is simpler.

As for the volute losses, the losses in the vaned channel of the return channel are computed by Aungier in terms of total pressure drop. In this work, they are converted into specific total enthalpy changes using the formula reported in eq. (3.54), except for the incidence loss which is computed with a correlation of a different author and it is already expressed in specific total enthalpy change. The formula in eq. (3.54) is equal to the one reported in eq. (3.2) but it is adapted to the vaned channel.

$$\Delta h_{tot,vc} = c_p \left(1 - \frac{1}{\left(1 + \frac{\Delta p_{tot,vc}}{p_{tot,5}} \right)^\vartheta} \right) T_{tot,5} \quad (3.54)$$

Since this is a vaned element, the incidence loss is considered. It is calculated following the Galvas correlation reported in eq. (3.55) as already done for the impeller in eq. (3.3) [8]. This loss is active only in off-design conditions because during design operation the flow angle is the optimum one, so the incidence loss is null.

$$\Delta h_{tot,inc} = \frac{v_4^2 \sin^2 (|\alpha_{4,f} - \alpha_{4,opt}|)}{2} \quad (3.55)$$

The skin friction loss inside the vaned channel is computed using the correlation reported in eq. (3.56) [10]. The first term inside the brackets represents the loss caused by the fluid dynamic friction of the flow against the walls of the channel. The second term inside the brackets is the curvature loss, derived from the one of the annular passage in eq. (3.53). The

friction coefficient $c_{f,vc}$ is computed applying the Colebrook equation reported in eq. (3.12) to the vaned channel.

$$\Delta p_{tot,fr} = \left(4c_{f,vc} \left(\frac{\bar{v}}{v_4} \right)^2 \frac{L_{b,vc}}{D_{hyd,vc}} + \frac{v_{m,4}v_{m,5}|\alpha_4 - \alpha_5|}{13v_4^2} \right) (p_{tot,4} - p_4) \quad (3.56)$$

The total pressure loss resulting from eq. (3.56) is converted into specific enthalpy applying the eq. (3.54).

The blade loading loss of the return channel is quantified by the correlation reported in eq. (3.57) [10].

$$\Delta p_{tot,bl} = \frac{\left(\frac{\Delta v_{rc}}{v_4} \right)^2}{6} (p_{tot,4} - p_4) \quad (3.57)$$

The term Δv_{rc} of eq. (3.57) is the average blade-to-blade velocity difference and it is computed as expressed in eq. (3.58).

$$\Delta v_{rc} = \frac{2\pi(r_4 v_{u,4} - r_5 v_{u,5})}{N_{b,vc} L_{b,vc}} \quad (3.58)$$

The total pressure loss resulting from eq. (3.57) is converted into specific enthalpy applying the eq. (3.54).

The wake mixing loss in the vaned channel is computed using the correlation reported in eq. (3.59) [10].

$$\Delta p_{tot,mix} = \left(\frac{v_{m,wake} - v_{m,mix}}{v_4} \right)^2 (p_{tot,4} - p_4) \quad (3.59)$$

The terms $v_{m,wake}$ and $v_{m,mix}$ used in eq. (3.59) represent the velocity meridional component, respectively, just before and just after the mixing process. Their definition is reported, respectively, in eq. (3.60) and (3.61). The tangential component of the velocities is governed by the conservation of angular momentum since the wake mixing happens outside the bladed section.

$$v_{m,wake} = \sqrt{v_{sep}^2 - v_{u,5}^2} \quad (3.60)$$

$$v_{m,mix} = v_{m,5} \frac{A_{out,vc}}{\pi D_5 b_5} \quad (3.61)$$

The term $A_{out,vc}$ used in eq. (3.61) represents the cross-sectional area at the outlet of the vaned channel and it is calculated as shown in eq. (3.62).

$$A_{out,vc} = (\pi D_5 - N_{b,vc} t_{vc}) b_5 \quad (3.62)$$

The term v_{sep} used in eq. (3.60) represents the velocity at which the flow boundary layer detaches from the blade. This velocity is important because in this point the flow mixing happens. In order to quantify the value of v_{sep} , it is necessary to define the maximum vane surface velocity $v_{max,vc}$, which is done in eq. (3.63). The quantity Δv_{rc} is the same one defined in eq. (3.58).

$$v_{max,vc} = \frac{1}{2}(v_4 + v_5) + \Delta v_{rc} \quad (3.63)$$

It must be checked that $v_{max,vc}$ is bigger than v_4 to include the most common case in which the maximum velocity in the vaned channel is the inlet velocity v_4 . So, if $v_{max,vc} < v_4$, the value of $v_{max,vc}$ must be corrected and it must be put equal to v_4 .

Now, v_{sep} is computed as indicated in eq. (3.64), so the formula adopted depends on the value of $v_{max,vc}$.

$$\begin{aligned} v_{sep} &= \frac{v_{max,vc}}{2}; & v_{max,vc} > 2v_5 \\ v_{sep} &= v_5; & v_{max,vc} \leq 2v_5 \end{aligned} \quad (3.64)$$

Finally, since all the quantities used in eq. (3.59) are known, the total pressure drop due to mixing can be calculated and it is then converted into a total specific enthalpy change applying eq. (3.54).

The Aungier method also proposes an approximate solution for the computation of the losses in the 2nd bend. However, it suggests treating it as an annular passage, which is what is done in the present work.

3.5.3 Second Bend Losses

This is the third and last component of the return channel encountered by the flow. It is an annular passage with a bending of 90°. The losses analysis is the same one used for the first

bend since they are the same type of component. So, in this work it is avoided to copy here the same loss correlations.

However, it is important to highlight a difference with the first bend: since this second bend has a curvature angle of 90° , the outlet radius is not equal to the inlet one. So, the simplified formula in eq. (3.50) used to compute $b_{max,bend1}$ cannot be used to compute $b_{max,bend2}$. It is instead necessary to pass to the complete version of that formula, reported in eq. (3.65).

$$b_{max,bend2} = \frac{r_5}{r_6} b_5 \left(1 + \frac{0.16L_{bend2}}{b_5} \right) \quad (3.65)$$

Chapter 4

Code

In this chapter, the code written to study the compressor is described. It is an original code, developed to apply the computational process described in the sub-section 2.3.1 and to make it possible from the numerical point of view. It is used the software “MATLAB” version “R2020a” on a laptop with the processor “Intel Core i7-5500U”, which has two cores that run at 2.40 GHz. Inside MATLAB, the “Optimization Toolbox” and the “Parallel Computing Toolbox” are used, respectively, to be able to use all the powerful optimization algorithms provided and to have the possibility of running the code in parallel on both the cores available on the processor described.

The code is always as modular as possible. This is extremely useful when a certain part of the code must be used multiple times (i.e., the loss correlations are used both to design the machine and to study the off-design behaviour) because if a change is needed to that part, it is sufficient to do it once and not every time that part is used.

In this chapter, the mechanisms of the code and its structure are described. However, the code is not described line by line and this is not a guide on how to use it. The code of this work has been written specifically for this kind of application (high compression ratio, high flexibility and high outlet temperature). In Chapter 5 the results obtained for the case study are shown and the decision taken are explained.

4.1 Design

The design of the multishaft multistage compressor is based on the optimization of each stage. The stages are divided into different shafts, so all the stages of a single shaft have the same rotational speed. The mass flow rate is conserved because any mass flow leaking outside the machine is neglected. The inlet conditions for each stage must be known to calculate the outlet ones. For the first stage, the inlet pressure and temperature are the ambient ones and they are assumed. For the following stages, the inlet temperature and pressure are the ones of the preceding stage outlet or of the preceding intercooler outlet. For this reason, the analysis of the stages must proceed from the first one to the last one, one at the time. So, it is not possible to implement a parallel process that computes more than one stage simultaneously.

The structure of the algorithm used for the design process is shown in Figure 4.1. It represents the overall design process and how it is conceptualized. Each passage of this process is analysed in detail in this section, highlighting the most important parts. The computational procedure used by the optimization process is described in the sub-section 2.3.1.

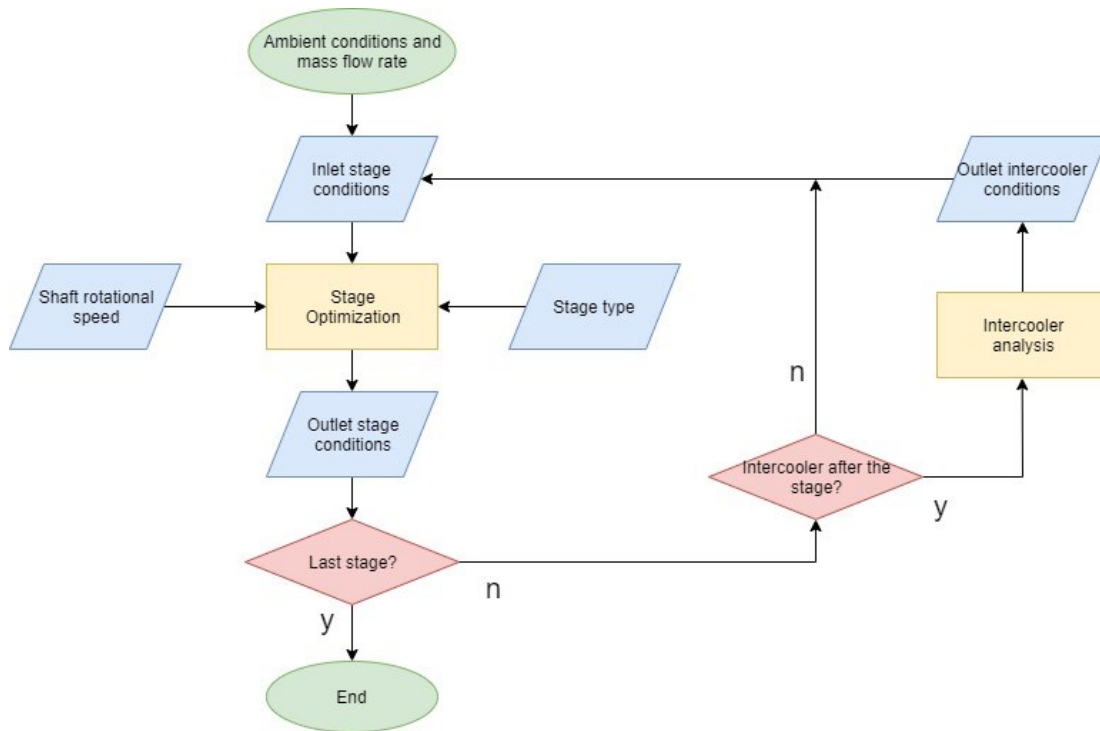


Figure 4.1 – Flow chart of the design algorithm.

4.1.1 Initial Design

The design of a multistage and multishaft centrifugal compressor is very complex, so a statistical analysis is needed before running the code. It manages to achieve a trade-off between the precision and the automation of the design and its computational cost. Its results are then tested with the code and a sensitivity analysis is performed to confirm them or to select different values.

The number of shafts and the number of stages to achieve the compression ratio required are evaluated with an initial design and they are given as input to the optimization code. To do this, it must be considered that increasing the number of stages and shafts, both the compression efficiency and the investment cost increase.

Once these two variables are selected, it must be decided how to divide the compression between the stages. A compression ratio for each stage is selected looking at the head coefficient ψ . It is a good idea to load all the stages of the same type (covered and uncovered impellers must be evaluated differently) with approximately the same head coefficient.

Moreover, the correct head coefficient is a trade-off between the number of stages and the efficiency, as described before. For a balanced value, a statistical analysis is the solution.

In the case of an A-CAES plant, to decide the distribution of the compression ratios between the stages, the position of the intercooler must be selected simultaneously. In fact, the compression ratio after the intercooler is decided assuming an efficiency for each stage and fixing the temperature at the outlet of the whole compressor. This temperature is important for the CAS, so it is a constraint for the compression system. This concept can be understood looking at eq. (4.1), where all the quantities are referred to the second part of the compression process, the one after the intercooler. This compression is adiabatic, so the isentropic work can be evaluated using eq. (2.12). Since the temperature at the outlet of the intercooler is fixed, the term $W_{is,ms}$ depends only on the compression ratio. In the end, to control the outlet temperature $T_{tot,out}$, the compression ratio after the intercooler is the variable to choose once the efficiency is assumed. This process could be done with the code, but an outer iteration cycle would be needed, changing the compression ratio distribution with the efficiency that varies at every iteration. This is simply too expensive from the computational point of view.

$$\frac{W_{is,ms}}{\eta_{is,ms}} = c_p (T_{tot,out} - T_{tot,in}) \quad (4.1)$$

The shaft rotational speed could be optimized by the code, but this would require again an outer loop. So, the rotational speed is selected calculating the specific speed ω_s and comparing it with the numbers proposed in the statistical charts.

Next, it is decided the type of impeller to apply. As explained in the sub-section 2.2.2, it is a good idea to use covered impellers for multistage machines due to the high axial tolerances and the shaft bending, so this type is usually preferred, even if it means a lower maximum tip speed for the impeller. A choice between volute and return channel must be made. This is quite easy: every time the flow needs to leave the inline configuration, a volute is adopted and when the flow can stay on the same shaft, a return channel is the solution. It must be decided in which stage to put the VIGV. As already seen in the sub-section 2.2.1, it is suggested to apply them only at the inlet of the first stage of each shaft.

Finally, the mass flow rate must be chosen to exploit approximately the power for which the plant is designed. Again, the mass flow rate is linked to the efficiency as described in eq. (4.2) and the efficiency is dependent on the mass flow rate because of all the loss correlations, so this would need an outer loop of iterations on the entire machine. It is instead computed using the value for the efficiency already assumed in eq. (4.1). At the end of the design optimization, it is checked that the values chosen for the initial design are close to the resulting ones.

$$P_{tot} = \dot{m} \frac{W_{is,ms}}{\eta_{is,ms}} \quad (4.2)$$

4.1.2 Optimization Method

In the Optimization Toolbox of the software MATLAB, various optimization methods are available [12]. All of them can find the minimum of a quantity changing the values of some variables. These variables are called design variables and the quantity to minimize is called objective quantity. In the end, the combination of design variables that minimizes the objective quantity is found. In the present work, the objective quantity is the negative of the efficiency of each compression stage. Doing so, the efficiency is automatically maximized, which is the target of the optimization.

The minimization algorithms of the various optimization methods are not analysed in detail because it is a very complex and vast topic and it is out of the scope of this work. However, the reasons for the choice of the method used are explained. They are based mainly on the suggestions written on the MATLAB site [12] and on the experience made trying different solutions. The function that the code must optimize is quite complex, in fact it has 8 design variables and 5 or 6 (depending on the stage type) non-linear constraints, so the optimization process is a delicate, complex and computationally expensive procedure.

In the design described in this work, the *patternsearch* method is adopted. The *fmincon* method has been tried as well, but it has some problems of local minima. In fact, even if it is way faster, the *fmincon* method is more likely to stop the minimization with a local minimum as a result. This kind of problem cannot be accepted because the optimization must find the maximum efficiency possible in the whole domain. Moreover, it can lead to designs that are very different if the input variables change by a little, so it can result in discontinuities among different stages or different plant conditions.

The *patternsearch* method represents a solution to this problem. In fact, it takes more function evaluations and it searches through several different regions of the domain [12]. However, calculating many function evaluations is computationally expensive. In this work, the design of each stage with the *patternsearch* method executed in parallel, using the MATLAB version and the processor indicated at the beginning of this chapter, needs from 250 to 2500 seconds. Since the machine is a multistage compressor, this is an important amount of time that limits the possibilities of this approach, in fact this is the main reason why an initial design is needed in the first place: an extremely fast optimization could allow to leave the choice of other variables to the code (i.e., the shafts rotational speed and the compression ratio distribution). But, again, a trade-off is achieved between speed and accuracy and the result of this trade-off is the *patternsearch* method preceded by an initial design.

However, the *patternsearch* can have problems of local minima as well. In general, if there are problems with the convergence of an optimization method, it is a good idea to try a new starting point. In a process as complex as the design of an entire stage of a centrifugal compressor, the starting point can be changed for every stage or even more than once for each stage, to better understand if the result found is a local minimum or a global one. It can

be useful to change the starting point even if the code does not converge or if an error appears.

Other methods are present in the Optimization Toolbox that take more function evaluations than the *patternsearch* (i.e., the genetic algorithm *ga* or the *particleswarm*). They are not adopted because of their complexity and their high computational time.

4.1.3 Assumptions

To design each stage, some quantities are calculated, some others are chosen by the optimization method, but a lot of quantities must be assumed. This is done for several reasons. The first one is that it is computationally expensive to optimize everything with the code. Then, some quantities are a standard in turbomachinery and they are fixed by technological and economic reasons. Finally, it is difficult to penalize the code for abusing of some variables, so sometimes it would calculate an implausible design, which makes the code unstable. In this sub-section, the main assumptions adopted in the present work are named and explained.

First, the multistage compressor is assumed adiabatic and with no mass leakage. This is done because the thermal power exchanged with the surrounding environment and the air mass flow leaving the machine are negligible for a preliminary design.

The average roughness R_a is assumed to be equal to 2 μm for all the surfaces in contact with the fluid. This is a typical value in turbomachinery.

The VIGV are assumed to be completely open in design condition, so the pre-swirl is considered only in off-design operation. The losses in the duct connecting the stage inlet with the VIGV and the ones in the converging duct between the VIGV and the impeller inlet are neglected. In case the stage has no VIGV, the losses that are neglected are the ones in the duct that connects the inlet of the stage with the inlet of the impeller. These assumptions are justified by the fact that these losses would most likely be very small. The section in which the VIGV are installed is assumed to be circular (not annular as the impeller inlet one) and its diameter D_{0a} is assumed to be 1.75 times the impeller tip one $D_{1,tip}$.

The axial length L_{ax} of each stage is assumed to be 80% of the radial length L_{rad} [11].

The thickness of the blades of the impeller and of the return channel is assumed to be constant along the blade length and equal to 2 mm.

The height of the vaneless diffuser b_3 is assumed to be 95% of the impeller outlet blade height b_2 . So, the ratio of vaneless diffuser inlet height to impeller exit height b^* , used in eq. (3.14), is assumed to be equal to 0.95 and the diffuser is defined as pinched (when its height is smaller than the impeller outlet height).

The wake fraction of the blade-to-blade space ε_{wake} used in eq. (3.14) is assumed to be equal to 0.1, so 10% of the impeller outlet flow is interested by the wake phenomenon.

The quantity k used in eq. (3.37) to compute the friction coefficient of the vaneless diffuser is assumed to be equal to 0.01. This is a typical value.

Regarding the leakage seals for covered impellers, the leakage gap ε_{leak} used in eq. (3.24) is assumed to be equal to 0.5 mm. The number of teeth inside the labyrinth seal N_{leak} used in this work is 4. This quantity is involved in eq. (3.23) to calculate the leakage mass flow. It is selected a straight through geometry with grooves for the sealing system, which implies that the coefficient C_D of eq. (3.23) is equal to 0.8, as shown in Figure 4.2.

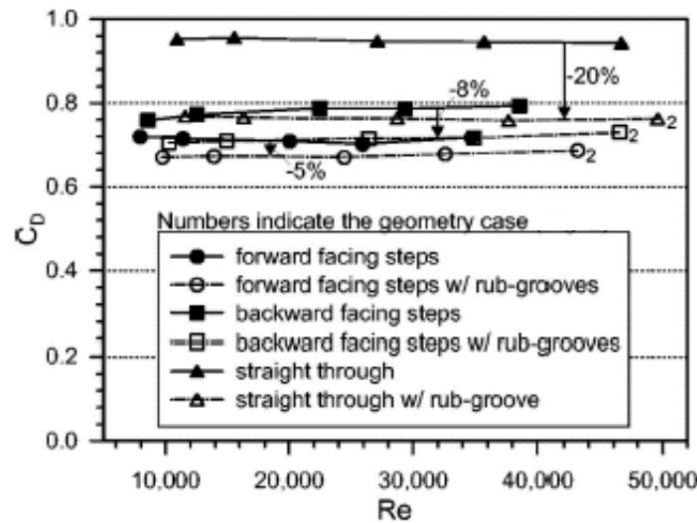


Figure 4.2 – C_D as function of the seal geometry and the Reynolds number [11].

The clearance gap ε_{cl} used in eq. (3.13) is assumed to be equal to 0.8 mm. This value is quite large (usually for a single stage compressor is about 0.5 mm) because centrifugal compressors with more stages on a single shaft are characterized by a high degree of axial motion and significant shaft bending phenomena, so the axial tolerances must be higher, as explained in the sub-section 2.2.2.

The disk-case gap and the cover-case gap (both are called ε_{disk} in this work) are assumed to be equal to 5 mm.

Regarding the volute, at its outlet and at the outlet of the conical diffuser the velocity is assumed to be only meridional, even if a swirl is present. The swirl effect is considered with the loss correlations.

In the return channel, a high number of hypothesis are made due to the complexity of its geometry. In the 1st bend, the tangential velocity at the inlet and at the outlet is assumed to be the same even if the friction with the walls will reduces it. This is due to the conservation of angular momentum since the inlet and outlet radius are equal. Then, the outlet height b_4 is imposed to be 1.8 times the inlet one b_3 . The radius of curvature is assumed to be 1.5 times the inlet height b_3 . These assumptions are introduced to simplify the study and they are reasonable values for a common geometry. In the vaned channel, the height is considered

constant and the outlet flow is designed to be radial, so the outlet swirl is present only in off-design conditions. The height of the 2nd bend is assumed constant and its outlet diameter is assumed to be equal to the impeller mid diameter, to have a good connection with the following stage. The assumptions relative to the 2nd bend are quite approximative because its geometry depends on the one of the following stage, which cannot be designed until the current stage is completed.

4.1.4 Design Variables

It is important to carefully choose as design variables quantities that are directly linked to the design of the machine and that are relevant in the technical literature. This helps to select proper boundaries for them: these boundaries are often available in the literature or they can be chosen to force the solution to have physical sense.

To design each stage, the design variables used in this work and their respective minimum and maximum allowed values are reported in Table 4.1 and Table 4.2. The term $D_{2,stat}$ is the statistical value for the outlet impeller diameter derived from the Cordier diagram in Figure 2.2. Its calculation is automatized using the code and this process is described in detail in the sub-section 4.1.7.

The intervals in which the design variable can be chosen are an indication of what should be done for a generic stage, but when a specific machine is designed and some specific targets need to be reached or some problems appear, these intervals can be forced to be smaller. They can also be enlarged to include more possibilities, but this should be done wisely and with a good justification.

Component	Impeller					Vaneless diffuser
Design variable	D_2 [m]	N_b [-]	$\frac{D_{1,hub}}{D_{1,tip}}$ [-]	$\frac{D_{1,tip}}{D_2}$ [-]	α_2 [°]	$\frac{D_3}{D_2}$ [-]
Min value	$0.3 \cdot D_{2,stat}$	6	0.3	0.5	50	1.2
Max value	$D_2(u_{2,max})$	30	0.7	0.7	70	1.8

Table 4.1 – Design variables and their optimization interval for the impeller and the vaneless diffuser.

Component	Return channel		Volute	
	Design variable	$N_{b,rc}$ [-]	$\frac{D_5}{D_{1,tip}}$ [-]	v_6 [m/s]
Min value	10	0.5	25	1
Max value	40	1.5	40	3

Table 4.2 – Design variables and their optimization interval for return channel and the volute.

Now it is explained the origin of each interval. To contain the centrifugal stresses and to assure the mechanical resistance of the machine, a maximum limit is imposed on the peripheral velocity of the impeller u_2 . Knowing the rotational speed, the limit on u_2 can be applied limiting the maximum diameter D_2 (which is a design variable), as expressed in eq. (4.3). This limit changes depending on whether the impeller is covered or uncovered because covered impellers have bigger centrifugal stresses at equal u_2 compared with uncovered ones, due to the added rotating mass of the cover. For covered impeller, the maximum u_2 is 400 m/s, for an uncovered one it is 600 m/s. These limits are common in the technical literature.

$$D_{2,max} = \frac{2u_{2,max}}{\omega} \quad (4.3)$$

The lower limit on D_2 is equal to 30% of the value $D_{2,stat}$. This limit is a weak limit since the code never goes close to it.

The upper and lower values chosen for the number of blades of the impeller N_b and for the number of blades in the vaned channel of the return channel $N_{b,rc}$ are also weak constraints and they are chosen to guide the code into physical results, but it never goes close to them. However, a lower limit for N_b is imposed as a non-linear constraint, as described in the next sub-section.

The intervals for $\frac{D_{1,hub}}{D_{1,tip}}$ and for $\frac{D_{1,tip}}{D_2}$ are taken from the technical literature [11]. Since the value of $D_{1,hub}$ is selected to satisfy the torque at the shaft (explained in the sub-section 4.1.6) and the value of D_2 is selected to work with the best impeller tip velocity u_2 , these two ratios depend mainly on the value of $D_{1,tip}$. This value is selected looking at the relative Mach number $M_{w1,tip}$ that results as consequence. The value of $M_{w1,tip}$ must be as low as possible to limit the losses. If the value of $D_{1,tip}$ is too low, the inlet absolute velocity v_1 becomes too high, causing a high $M_{w1,tip}$. If $D_{1,tip}$ is too high, the rotational velocity $u_{1,tip}$ becomes too high, causing again a high $M_{w1,tip}$. Moreover, a $D_{1,tip}$ too high generates a relative flow angle $\beta_{1,tip}$ too high, so the relative flow would be too tangential and the blade blockage would be excessive [11].

The upper limit on the angle α_2 is an important one. It is imposed to have a good flexibility because in off-design, at low mass flow rates, α_2 increases. For values of α_2 higher than 80° , the recirculation loss and the vaneless diffuser loss increase dramatically and the stage can stall. So, a trade-off between design performances and flexibility results in the choice of the maximum value for α_2 . Its lower limit, instead, is a weak limit and the code never approaches it.

The lower limit on the vaneless diffuser length is chosen because all the stages of a centrifugal compressor need a minimum length of vaneless diffuser, but the code never goes close to it. The upper limit, instead, is imposed because there is high risk of stall for vaneless diffusers that are too long. This happens because the flow loses momentum through the diffusion process and it is prone to reverse its direction and to come back towards the impeller exit.

The limits on the flow velocity v_6 in the outlet piping at the volute exit are due to common practice, in fact the upper limit is the maximum flow velocity allowed in the piping system and the lower limit is useful to impose a maximum size to the cross-sectional area of the outlet pipe.

The boundaries on the area ratio $\frac{A_6}{A_5}$ are imposed to limit the conical diffuser geometry, in fact the lower limit is equal to 1, meaning that it must be a diffuser and not a nozzle and the upper limit is chosen to impose a limit on the diffusion that happens in the conical diffuser, but it is never reached in optimal conditions.

The possible interval for the ratio $\frac{D_5}{D_{1,tip}}$ is the most difficult one to choose because the design of the outlet of the return channel is linked to the dimensions of the following stage, which are unknown when the computations on the current stage are executed. It is imposed an interval on this ratio to have the value of the outlet diameter of the vaned channel D_5 close to the one of the impeller inlet tip diameter $D_{1,tip}$. Then, also considering the curvature of the 2nd bend of the return channel, the outlet diameter of the current stage should be approximately equal to the inlet diameter of the following one. It is important to know that most likely the following stage has smaller or equal dimensions compared to the current stage because during the compression process the volumetric flow rate decreases.

4.1.5 Non-Linear Constraints

The boundaries imposed on the design variables are not sufficient to assure a meaningful optimization. In fact, some results of the calculations must also be constrained to have a good solution. These quantities are the maximum Mach numbers, the minimum number of impeller blades and the De Haller parameter.

Since the scope of the present work is an efficient compressor, it is chosen to work only with subsonic stages. This is justified by the fact that there is no particular need to have a compact or light machine, so it is chosen not to load too much the stages. It is imposed that the Mach numbers at the inlet of the vaned components must be below 1 to avoid any type of

supersonic shock. The Mach numbers in all the other points must be below 1.2. This less strict limit is due to the lower losses caused by a supersonic flow if it does not encounter any vaned element.

The minimum number of impeller blades is imposed to be the one computed using the Eckert correlation reported in eq. (4.4) [35]. Usually, this correlation is used to suggest the optimum number of blades. However, in this work it is used as lower limit because it seems that the loss correlations do not penalize enough the fluid phenomena that happen at low number of blades, so sometimes the code ends up with an optimum design that has a number of blades in the impeller that is too low to make physical sense. Using an empirical correlation as lower limit makes the code more stable and consistent, even if it limits its potential to explore lower numbers of blades.

$$N_b = \frac{2\pi \cos \bar{\beta}_g}{0.4 \ln \frac{D_2}{D_{1,mid}}} \quad (4.4)$$

The eq. (4.4) involves quantities that are computed during the optimization ($\bar{\beta}_g$ and $D_{1,mid}$), so it cannot be applied directly as lower limit to the optimization variable N_b . This is the reason why it is inserted as non-linear constraint.

The De Haller criterion, reported in eq. (4.5), is usually used to study the surge phenomenon in axial compressors. In the present work, it is adapted to be used in a centrifugal compressor because it is common practice to use criteria built for axial compressors to study also centrifugal ones. A justification for this choice can be found in the paper [36] that uses the same criterion reported in eq. (4.5) to limit the rangeability of a centrifugal compressor.

The condition reported in eq. (4.5) indicates the operational region without stall issues. Designing the stage, it is important to assure that it does not stall even when the flow rate is reduces, so the lower limit for the ratio $\frac{w_2}{w_{1,tip}}$ during the design is higher than 0.6 to guarantee flexibility. In the present work, each stage is designed to have $\frac{w_2}{w_{1,tip}} \geq 0.8$ to ensure flexibility and avoid stall at low flow rates.

$$\frac{w_2}{w_{1,tip}} \geq 0.6 \quad (4.5)$$

Finally, another constraint is imposed on the return channel. To have an inward 2nd bend, it is necessary to have its inlet diameter bigger than the outlet one. This constraint seems trivial from a human perspective, but it is important to lead the code in the direction of a physical result.

4.1.6 Shaft Torque

After the whole compressor design is performed, it must be checked the mechanical integrity of the shafts. In fact, the shaft diameter must be big enough to handle the torque provided by the electric motor and absorbed by each stage. However, the shaft diameter is directly linked to the geometry of each stage, in fact all the stage diameters must be larger than it. In particular, the check is done on the smallest one, the inlet hub diameter $D_{1,hub}$. It is assumed that it must be at least 1.5 times larger than the shaft diameter to fit the stage on the shaft.

It is checked if the shaft diameter needed to fit the stage is bigger than the minimum one required to handle the torque. This process is repeated for each stage, knowing that the torque reduces along the shaft because it is absorbed by every stage.

For each stage, the torque is computed as described in eq. (4.6) with P that refers to the power absorbed by the current stage and the ones that follow on the shaft, on the other side with respect to the motor.

$$T = \frac{P}{\omega} \quad (4.6)$$

It is computed the maximum allowed tensile stress on the shaft from the yield stress, imposing a safety factor of 2, as expressed in eq. (4.7). From the maximum tensile stress, it is calculated the maximum shear stress on the cross section using the von Mises yield criterion for a stress situation of pure torque, reported in eq. (4.8). Finally, it is computed the minimum diameter required to transmit that torque with that limit on the shear stress, as reported in eq. (4.9) [37].

$$\sigma_{max} = \frac{\sigma_{yield}}{2} \quad (4.7)$$

$$\tau_{max} = \frac{\sigma_{max}}{\sqrt{3}} \quad (4.8)$$

$$D_{shaft,min} = \sqrt[3]{\frac{16T}{\pi\tau_{max}}} \quad (4.9)$$

The material adopted for the shaft is a hardened and tempered steel, specifically the 39NiCrMo3. Its yield tensile stress σ_{yield} is about 900 MPa [38].

4.1.7 Starting Values

An optimization code requires a starting point to search for best combination of variables. In general, the starting value for a variable is chosen approximately in the middle of the interval defined by its constraints.

It is more interesting to procedure adopted to choose the value for the outlet diameter D_2 . It is based on a statistical approach using ω_s and D_s . In details, it consists in the digitization of the Cordier line of the diagram in Figure 2.2. This is achieved using the software *ScanIt* [28]. Using this software, some points are precisely extracted from the diagram in Figure 2.2 and a cubic spline is used to interpolate between them.

So, a numerical function is now available to correlate every value of ω_s to a value of D_s . The value of ω_s is computed applying eq. (2.23). From the corresponding value of D_s , it is possible to compute the value of the impeller external diameter D_2 .

This procedure it is fundamental for the optimization process because this algorithm must work for every possible mass flow rate and rotational speed. This implies that the value of D_2 can range in a huge interval. If the optimization process starts with a value of D_2 that does not make any sense, the computations will produce no meaningful result and the algorithm crashes at the first iteration. For other variables, the interval of possible values is not so huge, so this problem becomes not so relevant.

Another interesting starting value to choose is the one relative to the efficiency of the stage. It is selected as it is explained for D_2 , but this time the diagram digitized is the one reported in Figure 4.3, only the part relative to the centrifugal compressor subdomain [13]. However, the starting value for the efficiency is not crucial because its range for a reasonable design is not so big.

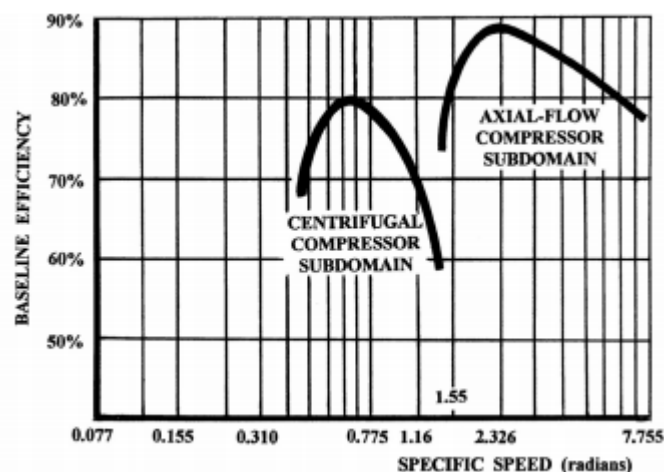


Figure 4.3 – Statistical values of efficiency as function of ω_s [13].

4.1.8 Intercooler

An analysis on the intercooler is performed to establish the values of pressure and temperature at the outlet of this component. The outlet temperature is assumed to be equal to the ambient one. This is a good assumption because the CAES plant studied in this work is located near the coast, since the CAS system is on the seabed. A power plant that operates on the coast has the advantage of having abundant sea water accessible. Using sea water in the intercooler, it is possible to cool down the compressed air to ambient temperature because a heat exchanger that uses water allows small temperature differences, due to the high heat transfer coefficient. However, the use of sea water can generate corrosion and fouling, so this aspect must be carefully considered. It is assumed a pressure drop for the air inside the intercooler of 2%, so the formula adopted to compute the outlet pressure is indicated in the eq. (4.10).

$$p_{ic,out} = 0.98 \cdot p_{ic,in} \quad (4.10)$$

4.2 Off-Design

Once the compressor is designed, its performances in off-design conditions are evaluated. In off-design operation, the geometry of the whole machine (except for the VIGV) is always the design one. So, to avoid to over-constrain the problem, all the fluid dynamic quantities cannot be imposed during the stage solution. For example, during the design process the compression ratio of each stage is imposed, but during the off-design analysis this is not possible because it is a result of the calculations.

The most difficult challenge is to keep the compression ratio of the whole machine constant at every flow rate. This is fundamental due to the nature of the isobaric CAS. In fact, to force the air to go into the CAS it is necessary to match its pressure with the compressor. Usually, compressors adjust their compression ratio to the flow rate imposed, as qualitatively shown in Figure 4.4. So, to force the machine to have a constant compression ratio at every flow rate, some degrees of freedom are needed.

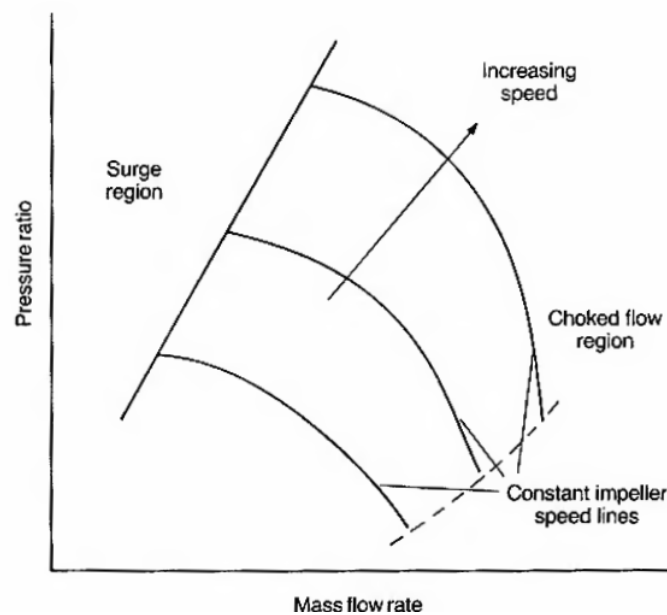


Figure 4.4 – Illustrative compressor performance map [8].

In particular, the electrical motor is equipped with an inverter that allows to control its rotational speed, as explained in the section 5.5. This variable is a parameter that allows to actively control the machine. Moreover, each VIGV installed is a further degree of freedom on which the code can operate to achieve the constant pressure goal.

In this section it is described the code written to actively manage the off-design operation. It is assumed that at least one VIGV is present on the whole machine and that the rotational speed can be changed. In fact, if there are two or more degrees of freedom, it is possible to fulfil the outlet pressure requirement and, at the same time, minimize the power consumed. To do so, an optimization method must be adopted.

4.2.1 Optimization Method

Differently from the design optimization, the off-design optimization is likely based on less variables. Their number is equal to the one of the VIGV present plus one, which is the rotational speed. In the present work, these variables are called control variables. However, the necessity of having a fixed outlet pressure is a very strong constraint that makes the process more difficult.

The optimization method must change the control variables and, for every combination that evaluates, it needs to compute all the stages of the machine. This makes every iteration much more computationally expensive than in the design case. Moreover, the off-design analysis must be executed on enough values of flow rate to makes possible to build a trend line to study the compressor performances.

It is used the *fmincon* as minimization method to optimize the off-design behaviour. This choice is based on the computational cost of each iteration and on the probability of local

minima. As discussed in the previous chapter, the *fmincon* method is quicker than the *patternsearch* because it takes less evaluations. So, since in this case the iterations are way more expensive, a faster method allows to contain the computational time. Using *fmincon* in serial, the analysis of each mass flow rate takes from 1100 seconds to 1500 seconds on the previously described processor. Moreover, the control variables interfere less with each other with respect to the design case. For example, the VIGV angle influences the fluid dynamics of the following stages, but this effect diminishes very quickly as the stages are more distant from that VIGV. For this reason, if the VIGV are positioned with some stages between them, their fluid dynamic effects do not combine significantly. This allows the code to control the VIGV separately and it helps to avoid problems of local minima.

4.2.2 Control Variables

As previously described, the control variables are the rotational speed and every VIGV present on the multistage compressor. The code must select a combination of them that satisfies the constraints and that minimizes the power absorbed by the whole machine.

The VIGV are usually placed only in the first stage of each shaft, so the maximum number of VIGV present in a multistage compressor is equal to the number of shafts. If there is only one motor connected to the shafts, the ratio of rotational speeds between the different shafts must remain constant, even if the rotational speed of the motor is regulated, because the shafts are connected to the same gearbox. For this reason, there is just one degree of freedom related to the rotational speed, even if more than one shaft is present.

There is an interval in which the variables can be selected to have a meaningful result. The VIGV angle is set to stay between -70° and 70° and the rotational speed must stay between the nominal value and 70% of it. However, these are weak limits because they are never approached by the code at the optimal point.

4.2.3 Non-linear Constraints

Due to the nature of the A-CAES plant with isobaric CAS, some specific constraints are imposed on the outlet of the whole machine. The first one is the pressure. As previously stated, the outlet pressure must be always constant due to the nature of the isobaric CAS. This necessity is set as a constraint on the optimization method, so the outlet pressure found in design condition is imposed for all the mass flow rates. The difference between the computed outlet pressure and the design one is the parameter that must be set to zero to fulfil the constraint. This difference can be divided by a factor to increase the tolerance of the optimization method. In fact, if the pressure is expressed in Pascal, there is no need to achieve a precision on the pressure constraint of a fraction of a Pascal.

Another non-linear constraint is the outlet temperature. The heat exchanger at the compressor outlet can handle an increase in the air temperature while maintaining the molten salts temperature constant (this is important for its thermal stability). The solution for this is

to increase the temperature difference between the air and the molten salts, for example reducing the heat exchange area. However, the compressor could have problems at high temperatures due to creep. The regulation of the rotational speed in off-design condition helps to avoid this phenomenon. The outlet temperature increases when the efficiency decreases, so probably when the flow rate reduces significantly. In this situation, also the rotational speed and, consequently, the centrifugal stress decrease. In the end, the reduction in centrifugal stress can partially compensate for the increase in temperature, mitigating the creep problem.

It must be considered that, if an intercooler is present, the VIGV can be used to control the outlet temperature managing the compression ratio before and after the intercooler. In fact, if the compression ratio before the intercooler is increased and the outlet pressure is fixed, the one after the intercooler is consequently reduced. Since the temperature exiting the intercooler is almost constant, a lower compression ratio implies a lower outlet temperature. However, the increase in compression ratio before the intercooler is limited by the maximum load that the stages can handle before stalling.

On the other side, the temperature should not decrease too much either. To avoid that the code minimizes the power absorbed reducing the outlet temperature, it is imposed a minimum acceptable value. This situation can appear when an intercooler is present in the compression process, due to the phenomenon already described. In fact, the reduction in outlet temperature means a lower average compression temperature, so a lower power consumption. The code always tries to reduce this power and a solution can be to have a lower outlet temperature. However, this solution is not good for an A-CAES because the temperature in the TES must be as high as possible. The highest temperature technically sustainable is the design one so, if the outlet air temperature decreases, the energy storage system is penalised and the advantage of a lower power consumption is cancelled.

Chapter 5

Results

In this chapter, the results obtained applying the code described in this thesis to the power plant proposed by Belloli and Hirn [4] (described in the section 1.3) are shown. The compression system proposed is analysed both in design conditions and in off-design operation. All the significant data available are illustrated in form of tables and graphs. The choices made by the author before, during and after the code execution are explained and justified. At the end, the mechanical and electrical system needed to drive the compressor is described and a specific selection of machines, correlated with the datasheets, is proposed.

The ambient temperature and the ambient pressure are assumed to be, respectively, 293.15 K and 101325 Pa .

5.1 Initial Design

As discussed in Chapter 4, the design of a multistage multishaft compressor is a complex task. It is so complex that it is not a good idea to automate the whole process. In the present work, an initial design is accomplished before the MATLAB code is involved. In this initial design, approximate values are used to derive some important quantities that are provided to the code as inputs. The quantities relative to the whole machine and the ones related to each stage are reported, respectively, in Table 5.1 and Table 5.2. The first stage of the compressor has a parallel configuration, meaning that the mass flow rate is split into two identical stages, so only one of them is analysed. The terms $\psi_{min,close}$ and $\psi_{min,open}$ are the minimum head coefficients relative to, respectively, a covered impeller and an uncovered impeller (considering the maximum u_2 allowed by the centrifugal stress). The values highlighted in green represent the choice made (between covered and uncovered impellers) for the stage of that row.

The target outlet temperature and pressure are respectively 625°C (898.15 K) and 81.06 bar ($\beta = 80$). A two-shafts configuration is selected. The design power for each compression train is 18.75 MW since the plant has a design compression power of 75 MW and four parallel compression trains are suggested. These quantities are proposed by Belloli and Hirn in their work [4].

Quantity	$c_p \left[\frac{J}{kgK} \right]$	Stage efficiency [-]	Shaft 1 [RPM]	Shaft 2 [RPM]	Mass flow rate [kg/s]
Value	1040	0.82	16000	28000	25

Table 5.1 – Values used in the initial design.

Stage	β	$T_{out} [K]$	$p_{out} [bar]$	$\rho_{out} \left[\frac{kg}{m^3} \right]$	$Q_{in} \left[\frac{m^3}{s} \right]$	$W_{is} \left[\frac{J}{kg} \right]$	ω_s	$\psi_{min,closed}$	$\psi_{min,open}$
0		293.0	1.01	1.20					
1	2.80	410.5	2.84	2.41	10.378	100175	0.959	0.626	0.278
IC	0.98	293.0	2.78	3.31	10.384				
2	2.70	405.7	7.51	6.44	7.56	96130	0.844	0.601	0.267
3	1.95	505.9	14.64	10.08	3.88	85423	0.660	0.534	0.237
4	1.70	603.2	24.89	14.37	2.48	83000	0.944	0.519	0.231
5	1.57	700.8	39.07	19.42	1.74	83191	0.790	0.520	0.231
6	1.48	798.4	57.82	25.22	1.29	83302	0.678	0.521	0.231
7	1.402	893.6	81.06	31.60	0.99	81156	0.607	0.507	0.225

Table 5.2 – Results of the initial design.

The purpose of the initial design is the evaluation of the number of stages, their division into the shafts, their compression ratios, their type (covered or uncovered impeller), the rotational speed of the shafts, the mass flow rate needed to absorb the design power and the position of the intercooler. Also, a check on the choice of two shafts is executed.

The values of c_p and of the stage efficiency reported in Table 5.1 are assumed. These assumptions are made to approximate average values. The number of shafts and their rotational speed are selected to have a good specific speed ω_s on all the stages. Looking at the statistical data, such as the diagram reported in Figure 4.3, a good interval for ω_s for a centrifugal compressor stage is between 0.5 and 1.3. The results reported in Table 5.2 show that ω_s is kept between 0.6 and 1 using only two shafts, so that choice is approved. It is important to avoid a ω_s higher than 1 for the first and second stages because it is likely to require a supersonic solution, which is not contemplated in this work. This issue is present only for the first and second stages because for the others the inlet temperature increases, decreasing the Mach number at equal velocity (eq. (2.7)).

The intercooler is positioned after the first compression stage. This is an easy choice because the compression ratio of 2.80 before the intercooler (required to have the correct temperature at the outlet of the last stage of the compressor) can be achieved with just one stage.

It is important to notice that the mass flow rate is divided into two parallel stages only for the first compression stage of the first shaft. So, the mass flow rate used in the calculations for that stage is half of the one used for all the other stages. The decision of adopting a

parallel configuration only for the first stage is due to the position of the intercooler. In fact, the volumetric flow rate would reduce dramatically between the first stage and the second stage if no parallel configuration is used. The reason for this is that the air is compressed and then cooled down by the intercooler, so its density increases a lot (Table 5.2). This would cause a drastic change in ω_s between the first stage and the second one, which would damage dramatically the performance of the compressor. In fact, as already explained, the interval of ω_s that results in a good centrifugal stage design is narrow.

To achieve a high efficiency and a good flexibility, 7 stages are used. This number could be reduced, but the stages would need to be more loaded and both the flexibility and the design efficiency would be damaged. The target of a CAES plant is to obtain good performances and there is no particular necessity of having a compact machine, so this reduction is not worth it. The first 3 stages are placed on the first shaft, which rotates at 16000 RPM, and the last 4 stages are placed on the second shaft, which rotates at 28000 RPM.

The first 2 stages are uncovered impellers because the volumetric flow rate is high, so the clearance loss remains relatively low even if the clearance gap is quite high, due to the multistage configuration. Also, the first stage needs to be uncovered because the compression ratio required before the intercooler would be quite high for a covered impeller. Apart from the first 2 stages, all the others have a covered impeller because of the smaller volumetric flow rate.

The compression ratio of each stage is chosen looking simultaneously at the head coefficient ψ and at the specific speed ω_s . The minimum head coefficient ψ_{min} is computed using the maximum rotational speed u_2 for that type of stage, which is equal to 400 m/s for a covered impeller and to 600 m/s for an uncovered one. The specific speed must stay in a small interval, as previously explained, and the head coefficient must be almost the same for each stage of the same type to equally distribute the load. The values found in the literature for ψ are between 0.7 and 0.8 for an uncovered impeller and between 0.6 and 0.7 for a covered one [11]. It can be noticed that in the present work the ψ_{min} is below the suggested values, so the stages are not designed to be highly loaded.

Finally, the VIGV are applied only to the first stage of each shaft (so, to the stage 1 and to the stage 4) as suggested in the sub-section 4.2.2. Since the stage 1 consists of two parallel stages, the VIGV actually used are 3. However, for the purpose of the analysis, the two parallel stages are managed as one since they are identical and operate with the same conditions. For this reason, only two VIGV are modelled.

5.2 Design

In this section, the results of the design process obtained through the code are presented and described. Since a huge number of quantities are computed for each stage, only the most significant ones are shown.

The main quantities for each stage are reported in Table 5.3. The compression ratio β is defined as the ratio between the stage outlet total pressure and the stage inlet total pressure. The stage outlet is determined to be the outlet of the conic diffuser in case a volute is involved or the outlet of the 2nd bend if a return channel is used. The efficiency $\eta_{is,ss}$ is defined in eq. (2.17).

The specific speeds ω_s reported in Table 5.3 are very similar to the ones evaluated in Table 5.2. This fact confirms that the initial design results are close to the ones obtained with the code. The head coefficient in Table 5.3 of the first two stages is much higher than the minimum one, reported in Table 5.2. This can be explained looking at Figure 5.1, where the actual impeller tip speed is compared to the maximum one for each stage. It can be observed that the difference between the design u_2 and the maximum one is significant for the first two stages, while all the other stages work almost at the maximum u_2 possible. For this reason, the head coefficient is way higher than the minimum one in the first two stages and it is close to the minimum value for all the other stages.

Stage number	1	2	3	4	5	6	7
Rotational speed [RPM]	16000	16000	16000	28000	28000	28000	28000
Impeller type	Uncovered	Uncovered	Covered	Covered	Covered	Covered	Covered
β	2.800	2.700	1.950	1.700	1.570	1.480	1.402
$\eta_{is,ss}$	0.834	0.842	0.813	0.817	0.819	0.824	0.806
ω_s	0.955	0.841	0.659	0.941	0.787	0.677	0.607
ψ	0.430	0.463	0.538	0.525	0.527	0.526	0.543
$T_{tot,out}$ [K]	413.45	407.53	511.69	611.30	709.04	803.99	896.16
$p_{tot,out}$ [Pa]	283727	750776	1464067	2489017	3907841	5783679	8108891
$W_{is,ss}$ [$\frac{J}{kg}$]	100763	96676	86002	84001	84242	84133	81546

Table 5.3 – Main quantities for each stage.

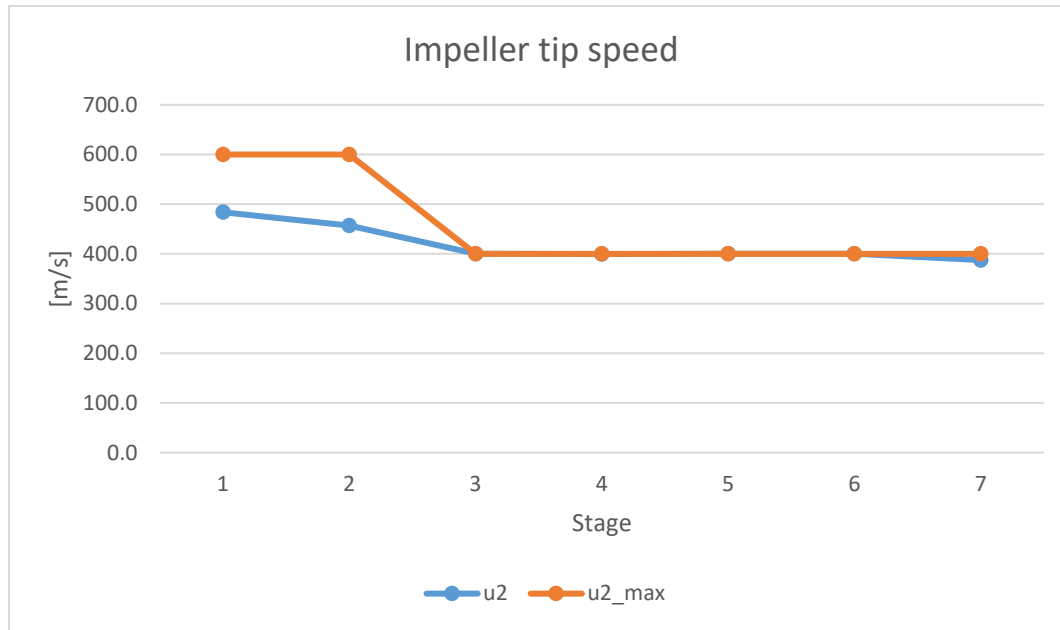


Figure 5.1 – Actual impeller tip speed and maximum impeller tip speed for each stage.

The design total power consumed by the compressor is equal to 18.761 MW (the one required by the plant project is 18.75 MW). It is calculated as the sum of the power of each stage, keeping in mind that the first stage is computed only once but it is composed of two parallel stages.

The design average efficiency of the whole compressor $\bar{\eta}_{is}$ is equal to 0.823 and it is obtained as the average of the efficiencies of each stage $\eta_{is,ss}$ weighted on the isentropic work, as described in eq. (5.1). It is used this definition to compute the efficiency of the compressor because the classic one (eq. (2.18)) would produce a value way lower due to the re-heat factor and it would not correctly represent the fluid dynamic quality of the machine. Another alternative is the polytropic efficiency, which does not suffer from the re-heat factor at all and it evaluates only the fluid dynamic aspect of the compressor. However, for the present work it is chosen the efficiency expressed in eq. (5.1).

$$\bar{\eta}_{is} = \frac{\sum_{i=1}^7 \eta_{is,ss,i} W_{is,ss,i}}{\sum_{i=1}^7 W_{is,ss,i}} \quad (5.1)$$

Another important parameter that characterizes a compressor of an A-CAES plant is the thermal power dissipated by the intercooler. In design conditions, this value is equal to 3.02 MW.

5.2.1 Geometry

In the scale model shown in Figure 5.2, it is possible to understand the dimensions and the geometrical configuration of each component. The parallel stage is organized in a back-to-

back configuration. This arrangement implies that the axial thrusts are oriented in opposite directions, so their effect on the bearings is negligible [5]. Also, it can be noticed that the volute starts before the vaneless diffuser ends. This allows to have a lower wetted surface and less radial extension of the machine, but it provides the same kinetic energy recovery since the fluid dynamic path is the same inside the vaneless diffuser and inside the first part of the volute, where the curvature has not started yet.

All the stages on the high-pressure shaft have covered impellers and they all work with an impeller tip speed u_2 close to the maximum one (which is equal to 400 m/s for covered impellers), as shown in Figure 5.1. Since they rotate all with the same rotational speed (they are connected to the same shaft), to have the same u_2 they need to have the same outlet impeller diameter D_2 . This result is visible both in Figure 5.2 and in Figure 5.3. The electrical motor is connected on the left for both shafts.

Generally, the trend is a reduction in the overall dimension of the stages as the compression proceeds. This is due to the reduction in the volumetric flow rate, which happens also between the first and the second stage, even if the first one processes only half of the mass flow rate because of the parallel configuration (Table 5.2).

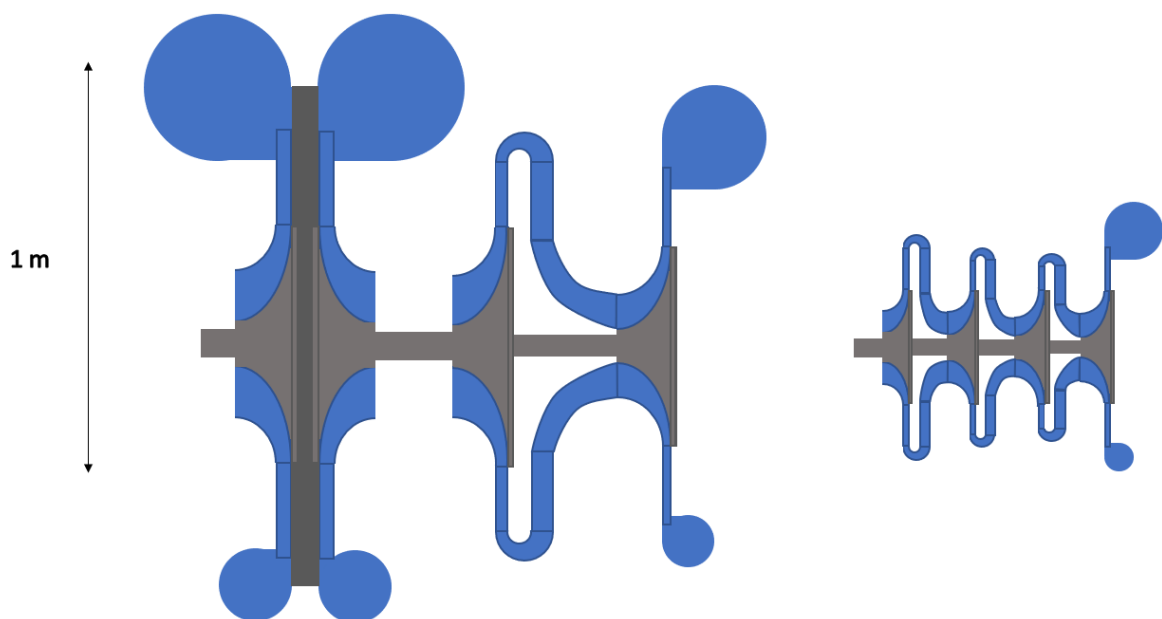


Figure 5.2 – Scale section of the multistage compressor. The stage number increases from left to right.

The geometrical dimensions are better quantified in the following diagrams. In Figure 5.3 the diameter values for the impeller and the diffuser are illustrated. The impeller outlet

diameter D_2 is almost constant for all the stages of the high-pressure shaft, as already discussed.

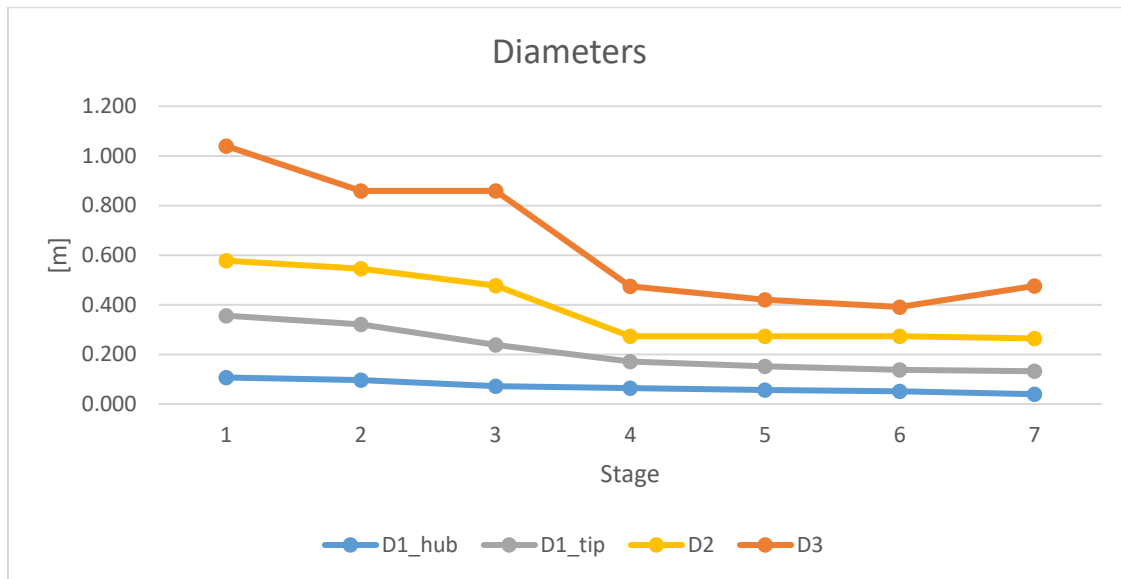


Figure 5.3 – Impeller and vaneless diffuser diameters for each stage.

In Figure 5.4 it can be noticed that the ratio between the diffuser outlet diameter D_3 and the impeller outlet diameter D_2 tends to be bigger in the stages equipped with a volute (stage 1, stage 3 and stage 7). The reason for this is that when a return channel is present at the outlet of a stage, the kinetic energy is partially saved and exploited by the following stage, so the diffuser function is not particularly important. When a volute is adopted, instead, the kinetic energy must decrease because the flow velocity in the outlet pipe must be limited. The volute is not very efficient at recovering this kinetic energy into static pressure, so it is way better to let this recovering process happen in the diffuser, which is longer for this reason.

In fact, in all the stages ending with a volute the vaneless diffuser length is the maximum one allowed by the constraints ($\left(\frac{D_3}{D_2}\right)_{max} = 1.8$), as shown in Figure 5.4. Moreover, the vaneless diffuser length is linked also to the impeller outlet velocity v_2 : a higher v_2 implies

a higher kinetic energy at the outlet of the impeller that must be recovered by the diffuser, so a longer diffuser results as a consequence.

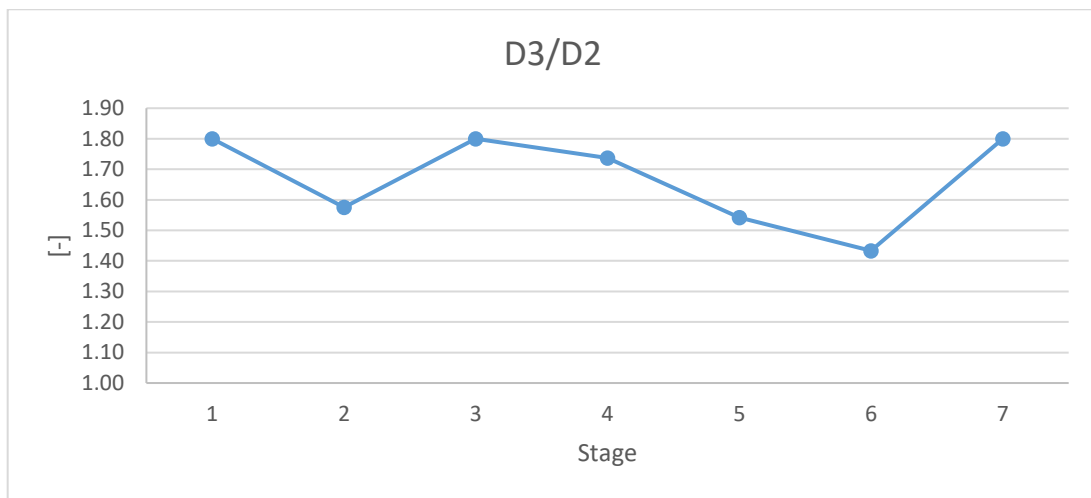


Figure 5.4 – Diffuser outlet diameter to impeller outlet diameter ratio for each stage.

In Figure 5.5 the inlet and outlet impeller blade height are shown. In Figure 5.6, the number of impeller blades N_b and return channel blades $N_{b,vc}$ are reported. The impeller blade heights follow the trend of the stage dimensions, so they decrease as the volumetric flow rate decreases. However, the number of blades both of the impeller and of the vaned channel does not show any monotonic trend. The vaned channel has more blades than the impeller due to the solidity concept. In fact, since the diameter at which the vaned channel is positioned is higher, it needs more blades to manage the whole circumference.

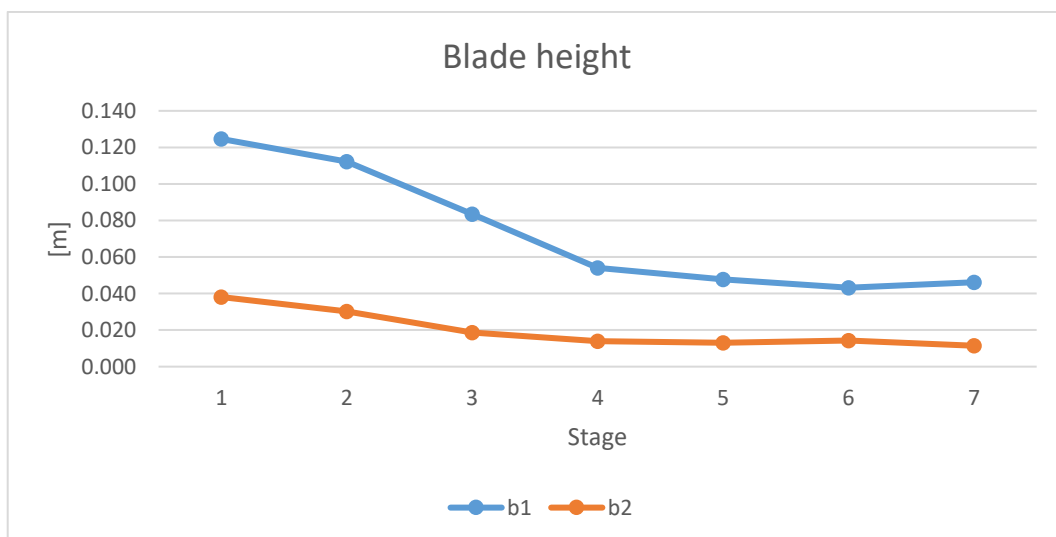


Figure 5.5 – Inlet and outlet impeller blade heights for each stage.

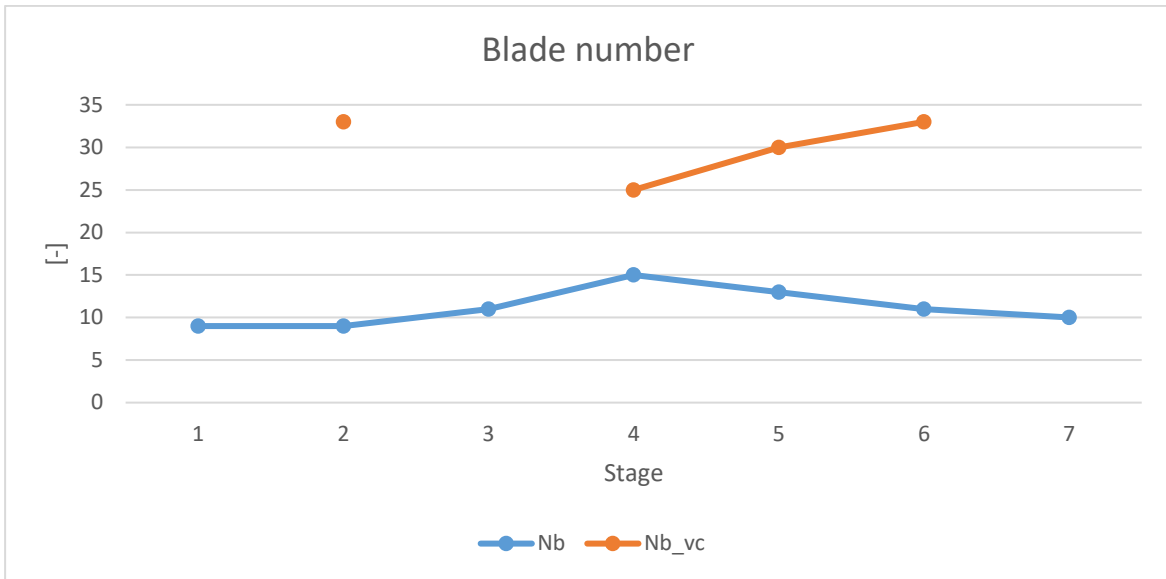


Figure 5.6 – Number of blades present in the impeller and in the vaned channel of the return channel for each stage.

5.2.2 Loss Mechanisms

The losses of each stage are presented in Figure 5.7. The losses inside the impeller are divided into their respective fluid dynamic mechanisms.

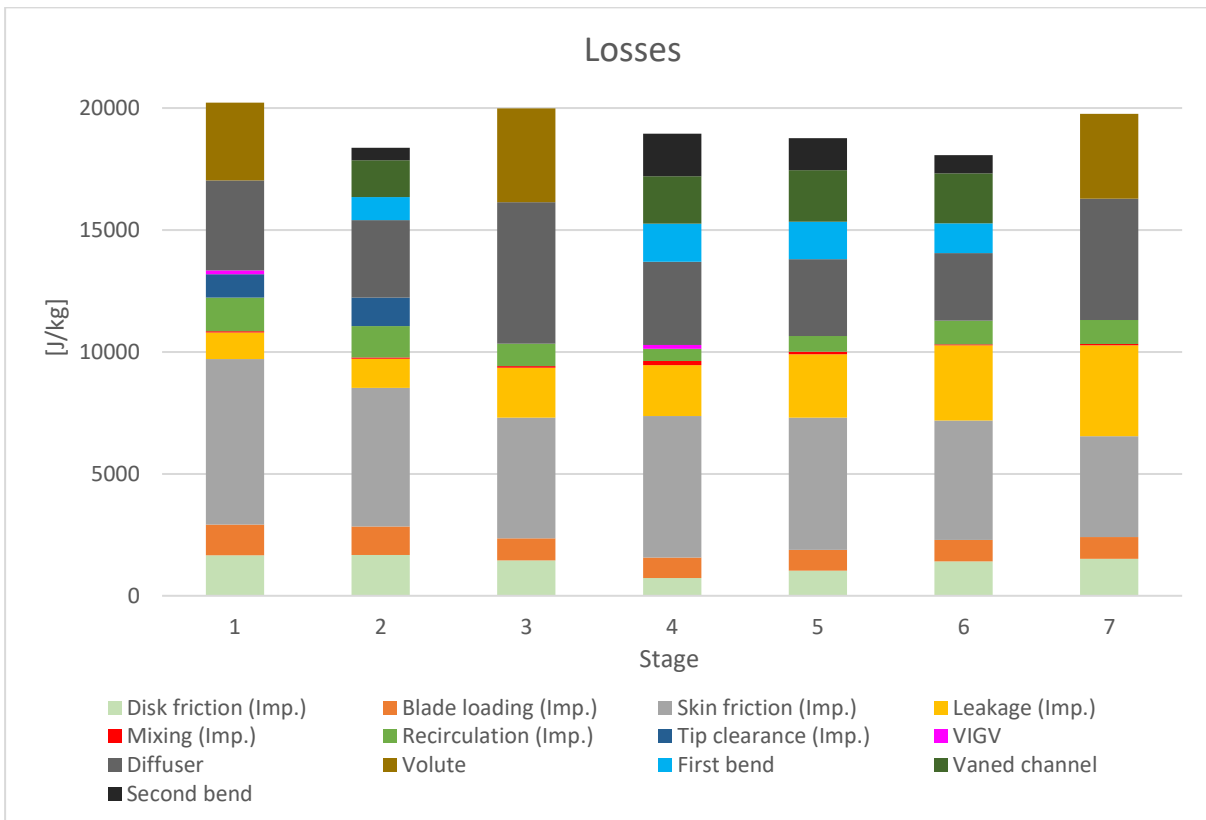


Figure 5.7 – Types of losses for each stage.

The most trivial concept that must be noticed is that in the stages equipped with a volute, there are no losses regarding the return channel (which is composed by 1st bend, vaned channel and 2nd bend) and vice versa. Also, since the VIGV are applied only to the stage 1 and to the stage 4, the VIGV loss is active only on these stages. However, its value is quite low in both of them due to the fact that the inlet duct has a big cross-section area compared to the one at the inlet of the impeller, so the flow velocity is low.

It is very important to highlight that not all the losses have the same thermodynamic effect. In fact, due to the re-heat factor, the losses that happen at the start of the compression process have a higher impact on the stage performances with respect to the ones that happen at the end, comparing the same amount of loss. For example, a static enthalpy increase inside the impeller damages more the performances of that particular stage with respect to the same static enthalpy increase happening in the vaneless diffuser. Moreover, the loss mechanisms inside the impeller are divided into internal losses and external losses that have different effects, as described in Chapter 2 and in Chapter 3. These considerations lead to the fact that the losses cannot be simply added up. The graph in Figure 5.7 is useful to compare the loss mechanisms inside a stage and to study the importance of a loss mechanism for different stages, but the losses are different and they cannot be summed all together.

The importance of the leakage loss increases with the stage number. This happens because the last stages are smaller than the first ones. In fact, the leakage mass flow rate is linked to the clearance gap ε_{cl} in uncovered impellers and to the leakage gap ε_{leak} in covered ones. Both these quantities are fixed because they are a technological limit, so their relative impact is higher for smaller machines. The same concept is valid also for the tip clearance loss, but this loss mechanism is present only in the first two stages since they are the only uncovered ones. Moreover, the leakage loss is higher in the stages with covered impellers (which are the stages 3, 4, 5, 6 and 7). It must be recognized that the seal leakage loss in covered impellers can be reduced improving the eye labyrinth seal (i.e., increasing the number of teeth in the seal), so its big impact on the small stages can be mitigated.

The impact of the vaneless diffuser loss is higher in the stages equipped with a volute. This is reasonable because, as already explained in 5.2.1, when a volute is used the kinetic energy of the flow must be converted into static pressure. Since the volute is not efficient in doing so, this process is mainly carried out by the vaneless diffuser. When a return channel is present, a good amount of kinetic energy can exit the stage and it is exploited by the following stage. So, the vaneless diffuser loss is higher if the stage is equipped with a volute because it must recover a higher amount of kinetic energy.

5.2.3 Velocity Triangles

The velocity triangles at the inlet and outlet of the impeller are reported in the diagrams from Figure 5.8 to Figure 5.14. The orange vectors represent the impeller outlet velocity triangle, the blue vectors represent the inlet one, the orange dotted line represent the geometrical

direction of the blade at the outlet of the impeller and the blue dotted line represent the geometrical direction of the blade at the inlet of the impeller. The velocity triangles at the impeller inlet are drawn at the mid diameter. All the velocity triangles follow the vectorial sum $\vec{v} = \vec{u} + \vec{w}$.

The difference between the blade direction and the flow direction at the design point is caused by the blades thickness at the impeller inlet and by the slip factor σ at the impeller outlet. The design flow direction at the inlet of the impeller is the optimal one, the one that generates no incidence loss. This optimal direction is different from the blade direction because the flow must respect the continuity equation and the conservation of angular momentum. Since the cross-sectional area just after the leading edge of the blades is smaller than the area just before it, the meridional velocity of the flow must be suddenly higher. However, the conservation of angular momentum requires that the tangential velocity component remains constant. For this reason, the flow direction just before the blades inlet is different from the one just after it.

The variation between the design flow direction and the blade direction at the impeller outlet is explained by the slip factor, as described in eq. (2.27).

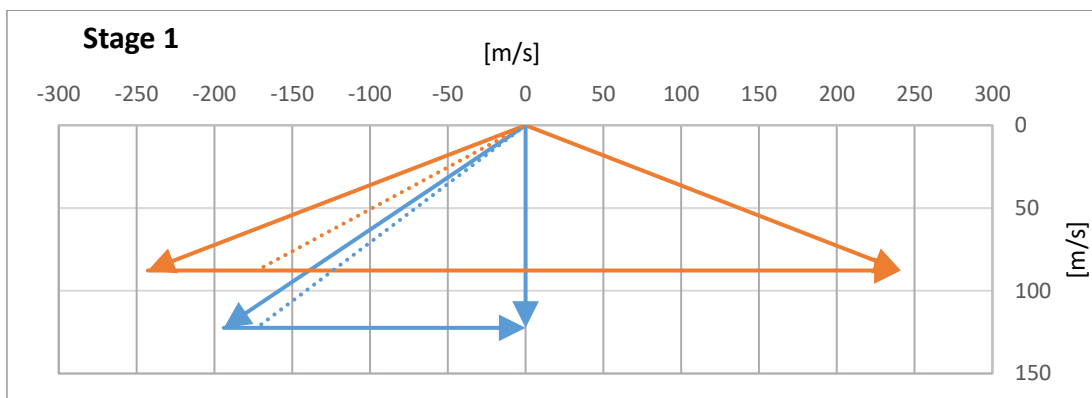


Figure 5.8 – Impeller velocity triangles of stage 1.

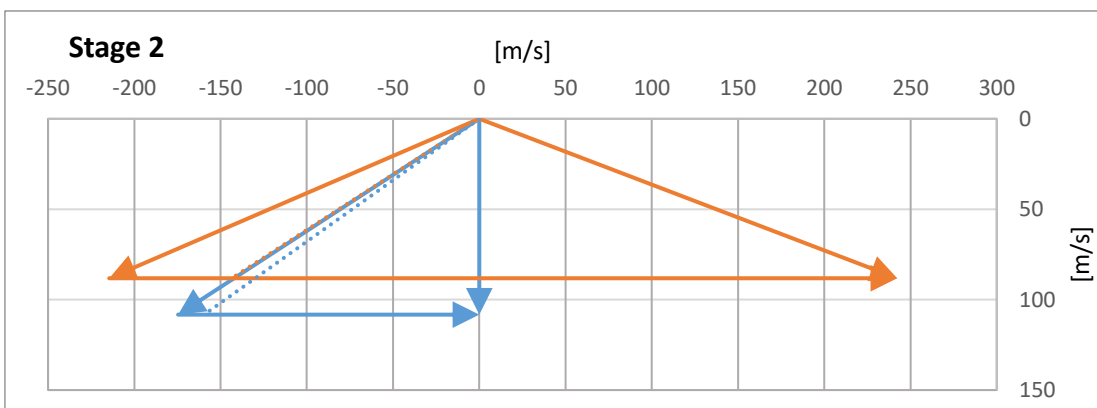


Figure 5.9 – Impeller velocity triangles of stage 2.

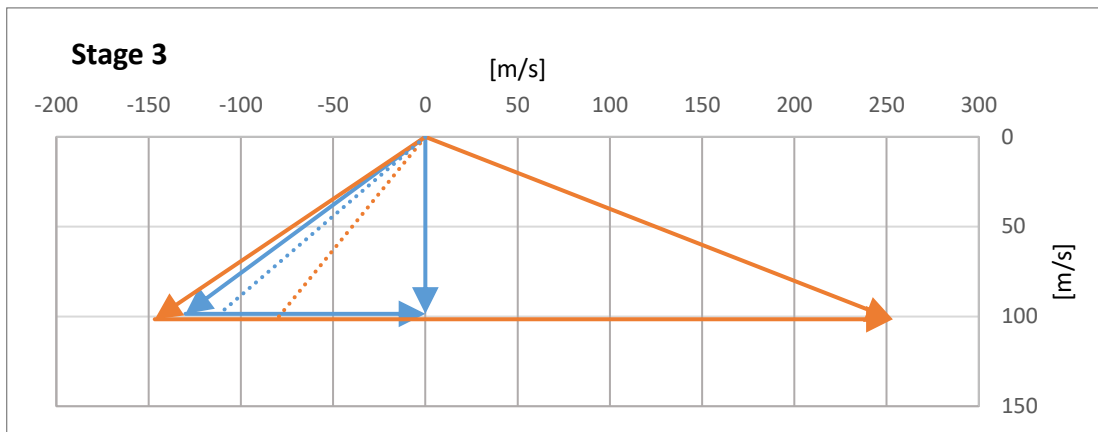


Figure 5.10 – Impeller velocity triangles of stage 3.

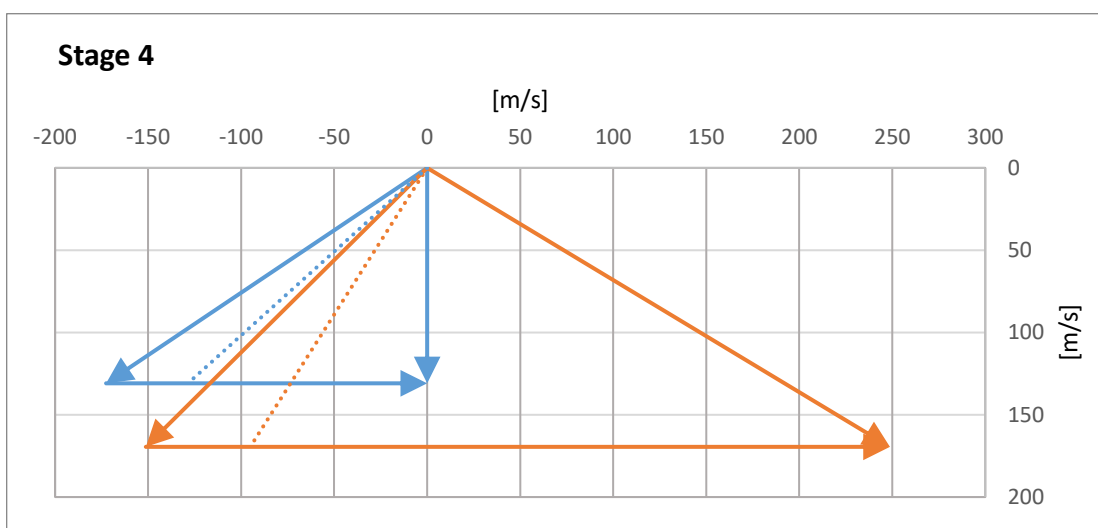


Figure 5.11 – Impeller velocity triangles of stage 4.

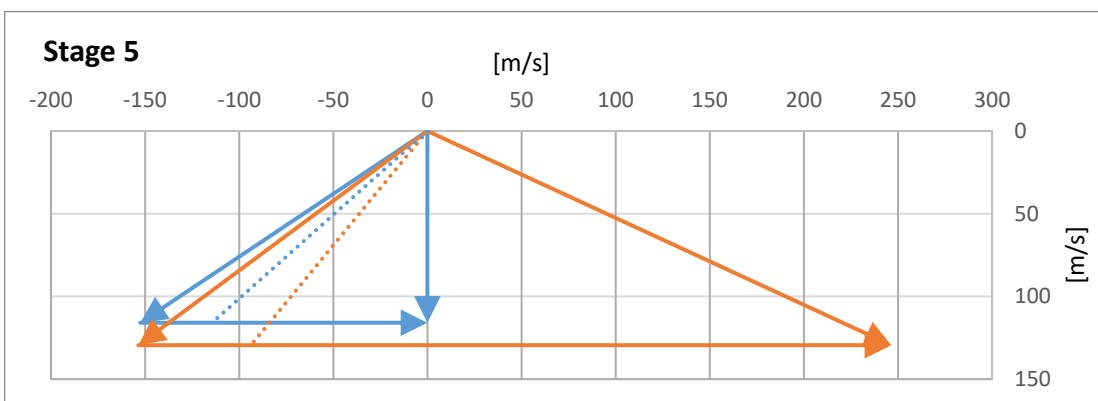


Figure 5.12 – Impeller velocity triangles of stage 5.

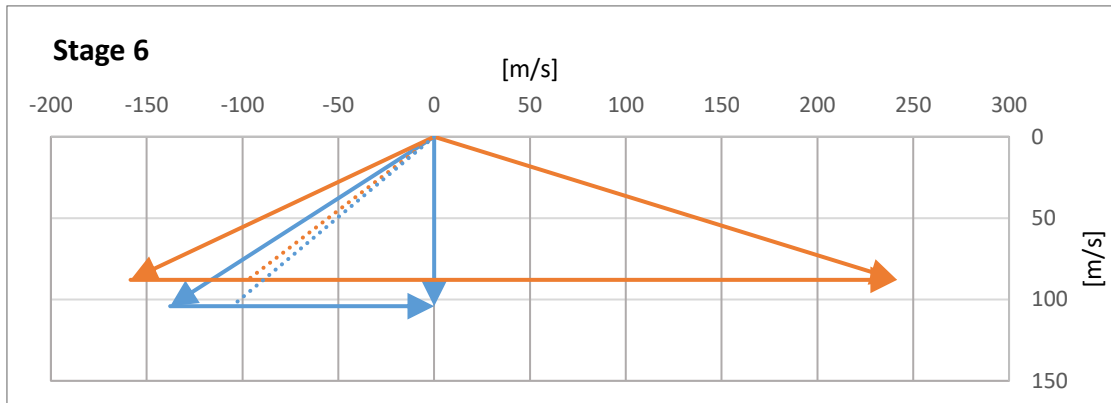


Figure 5.13 – Impeller velocity triangles of stage 6.

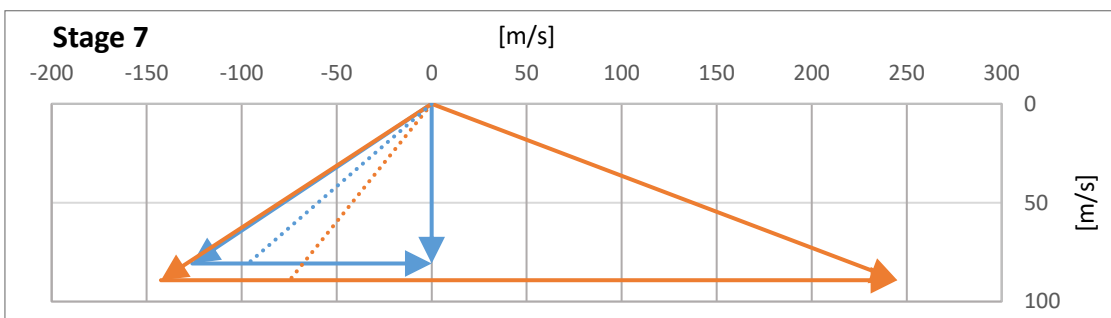


Figure 5.14 – Impeller velocity triangles of stage 7.

The difference between the blade direction and the design flow direction at the inlet is higher for the smaller stages. In fact, since the blade thickness is fixed for all the stages and the number of impeller blades does not decrease significantly with the stage dimension (Figure 5.6), the area reduction due to the blade blockage at the impeller inlet increases as the inlet diameters decrease (Figure 5.3). The fact that the meridional velocity at the inlet is higher for some stages and lower for some others with respect to the outlet one is simply a result of the optimization process.

In Figure 5.15, the relative Mach number at the tip diameter of the impeller inlet $M_{w1,tip}$ is shown. In the present work, this Mach number is the highest one in the stage (in other compressors, the outlet ones can be higher) and the impeller inlet is the worst point to have a supersonic flow. The reason for this is that the impeller blades would cause a shockwave at the beginning of the compression, causing significant fluid dynamic losses. It can be noticed that the only two stages in which the flow is close to the sonic condition are the stage 1 and the stage 2. This is due to the low temperature of the fluid (also the stage 2 works with the air at the inlet at ambient temperature due to the presence of the intercooler) and to their high rotational velocity u_1 (both have uncovered impellers).

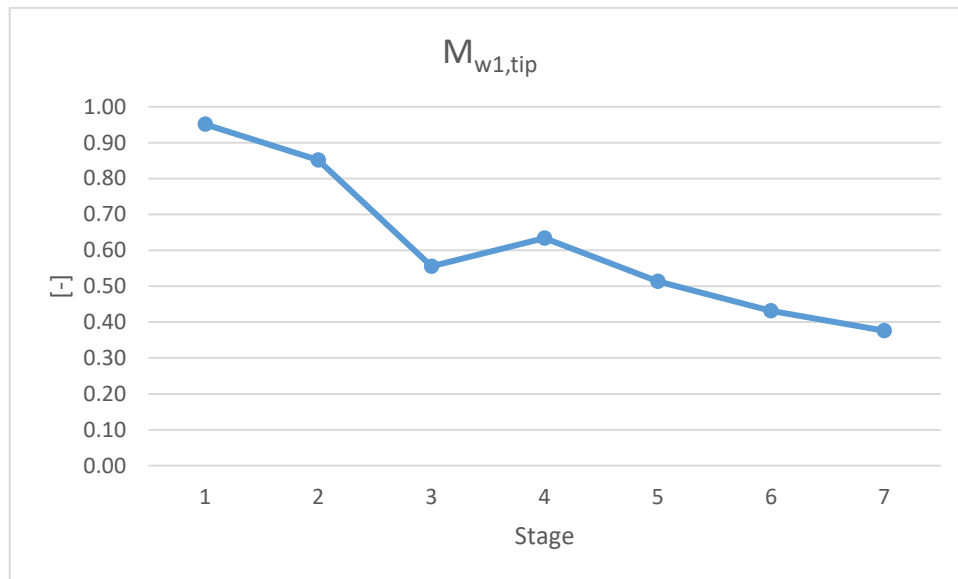


Figure 5.15 – Relative Mach number at the tip diameter at the inlet of the impeller for each stage.

5.3 Shaft Torque

The check on the mechanical resistance of the shaft is executed only in design conditions. In off-design conditions, the reduction of rotational speed is small compared to the reduction in the mechanical power required by the machine, so the torque is lower than in the design case. If the machine is required to work above 100% of the design power, this check must be performed also in that operating region because the torque is very likely to rise with the power, but this situation is not analysed in the present work.

The design power of the low-pressure shaft is equal to 8.536 MW (considering the parallel configuration) and the one of the high-pressure shaft is 10.225 MW.

The design values of the inlet hub diameter $D_{1,hub}$ are compared with the minimum ones required to guarantee the mechanical integrity of the shaft, following the procedure described in the sub-section 4.1.6. The values relative to the low-pressure shaft are reported in Figure 5.16 and the ones relative to the high-pressure shaft are reported in Figure 5.17.

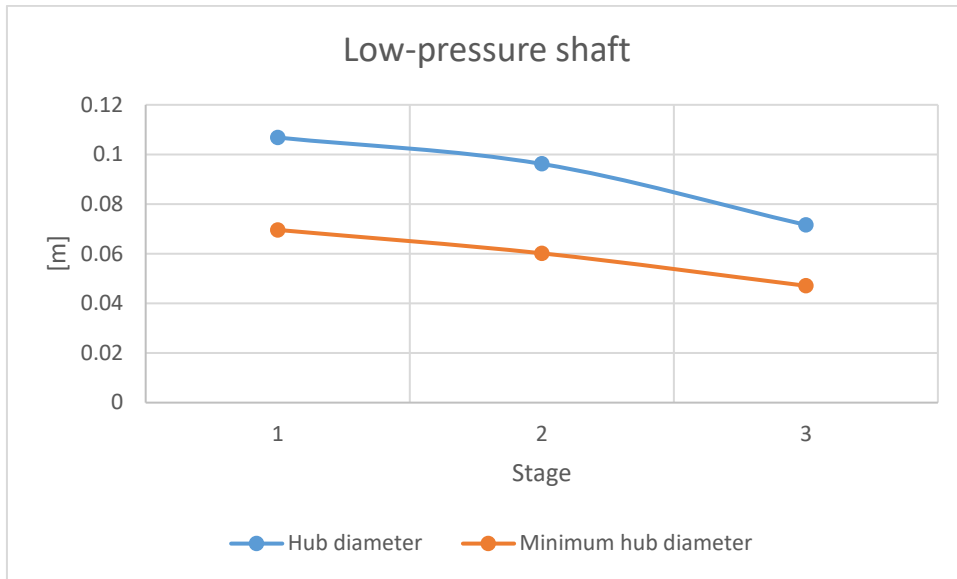


Figure 5.16 – Comparison between the mechanical requirements and the actual values for the hub diameter of each stage of the low-pressure shaft.

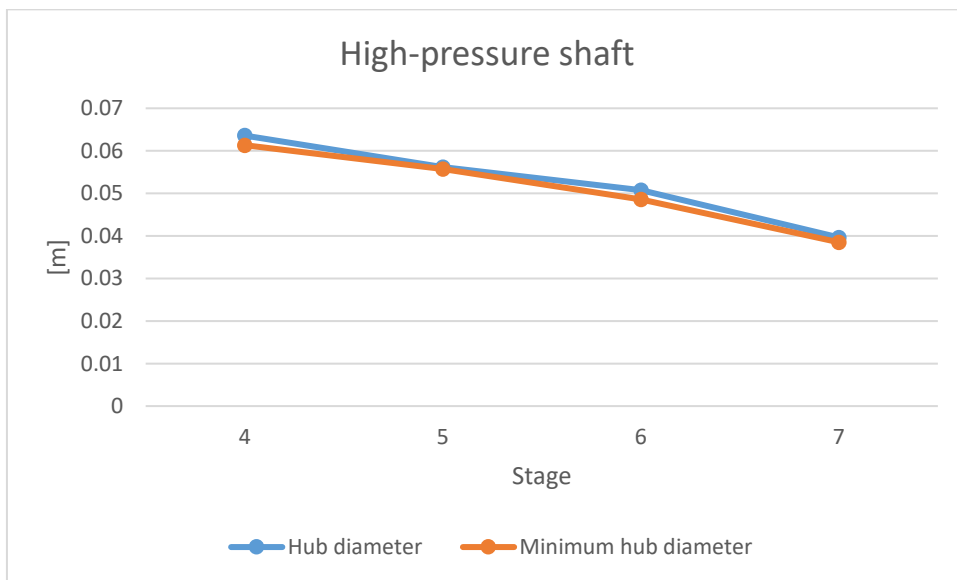


Figure 5.17 – Comparison between the mechanical requirements and the actual values for the hub diameter of each stage of the high-pressure shaft.

It is clear that the mechanical constraint of the torque is an issue only on the high-pressure shaft. In fact, the design values are very close to the minimum one. It must be noticed that the safety factor used is equal to 2 and the ratio between $D_{1,hub}$ and the shaft diameter is assumed to be at least 1.5.

To respect the constraint, it is necessary to impose a minimum value for the design variable $\frac{D_{1,hub}}{D_{1,tip}}$ equal to 0.37 instead of 0.3 for the stages 4, 5 and 6.

5.4 Off-Design

The off-design analysis is conducted between 50% and 100% of the design mass flow rate, running the code every 10%. The idea is to study the compressor until 50% of the design power to be able to regulate the A-CAES plant, which is composed of four parallel trains, continuously between 12.5% and 100% of the plant nominal power. The mass flow rate at 50% of the design power is lower than 50% of the design one because the efficiency is lower than in the design condition (Figure 5.21). However, the study is interrupted at 50% of the design mass flow rate because the results show that a stall is likely to happen. A detailed analysis of this concept is conducted in the sub-section 5.4.3.

The pressure exiting the compressor is always equal to 81.06 bar ($\beta = 80$). The outlet temperature reported in Figure 5.18 is constrained to stay between 620°C and 700°C, however the upper limit is never approached by the code. The reasons to impose an acceptable temperature interval are discussed in the sub-section 4.2.3. The outlet temperature remains almost constant for high mass flow rates, but it increases steeply as the mass flow rate approaches lower values. This behaviour is explained in the next sub-section since it is linked to the VIGV regulation.

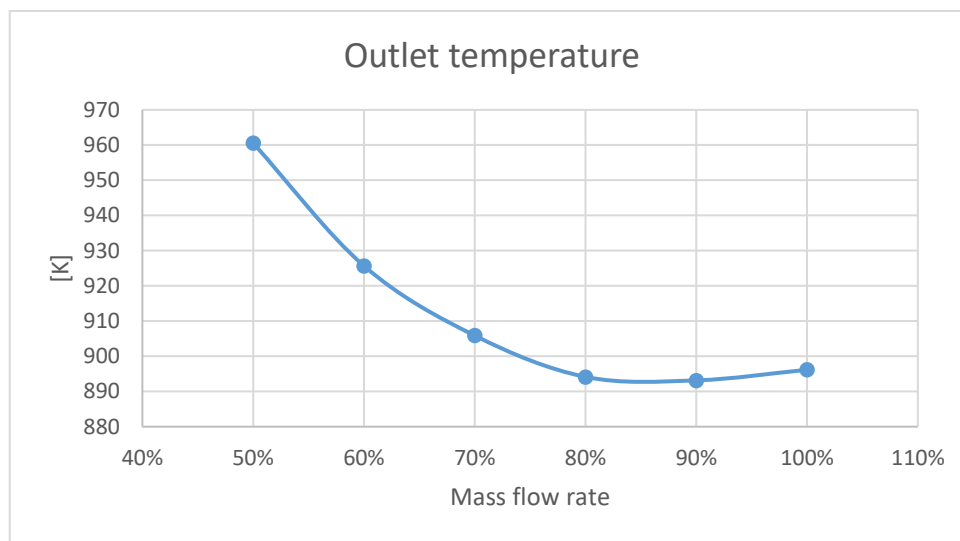


Figure 5.18 – Temperature at the outlet of the compressor in off-design operation.

The thermal power dissipated by the intercooler is reported in Figure 5.19. It can be noticed that the specific enthalpy drop of the air inside the intercooler increases as the mass flow rate decreases because the thermal power is not directly proportional to the mass flow rate (i.e., at 50% of the design mass flow rate the thermal power is more than 50% of the design one). The same thing happens with the compression power reported in Figure 5.20: the specific work W_{act} of the whole machine increases as the mass flow rate decreases since the power is not directly proportional to the mass flow rate. These two facts are related to the decrease in the average efficiency $\bar{\eta}_{is}$ defined in eq. (5.1) and reported in Figure 5.21 for the off-design operation.

The increase in the specific enthalpy drop inside the intercooler helps to compensate for the temperature increase caused by the drop in the average efficiency. A lower compression temperature causes a lower power consumption, for this reason the optimization process selects to dissipate more specific enthalpy in the intercooler. The increase in the total specific work W_{act} absorbed by the compressor is a consequence of the lower average efficiency and the fixed compression ratio. In general, the W_{act} of all the centrifugal compressors with a negative β_2 increases as the mass flow rate decreases if no control variables are actively changed.

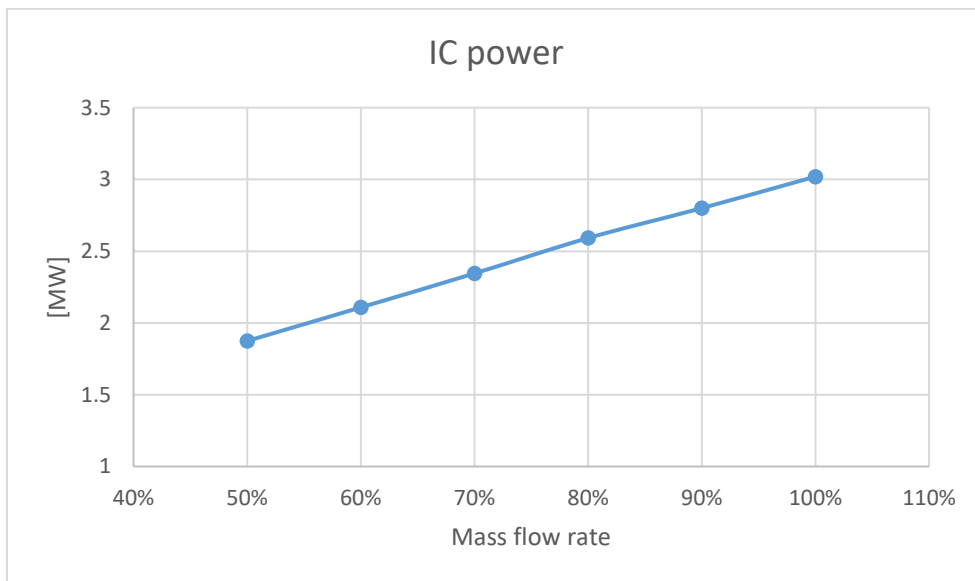


Figure 5.19 – Thermal power dissipated by the intercooler in off-design operation.

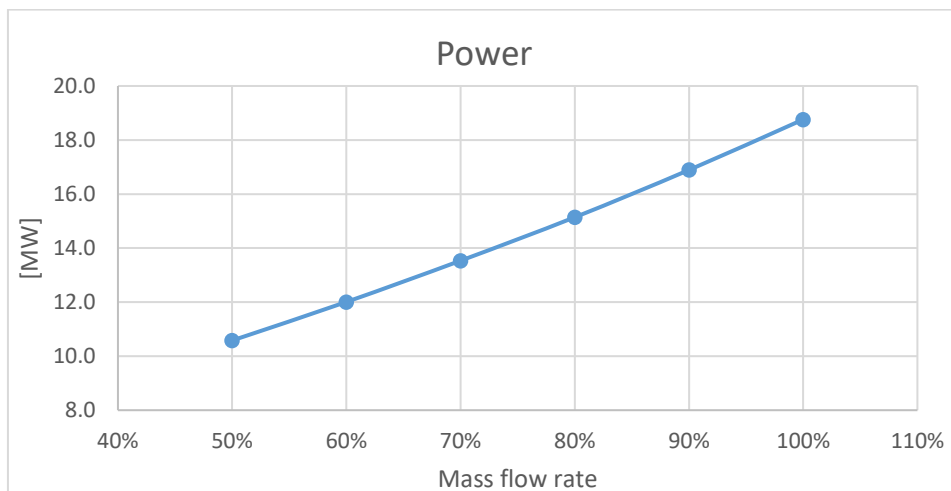


Figure 5.20 – Compression power absorbed by the whole compressor in off-design operation.

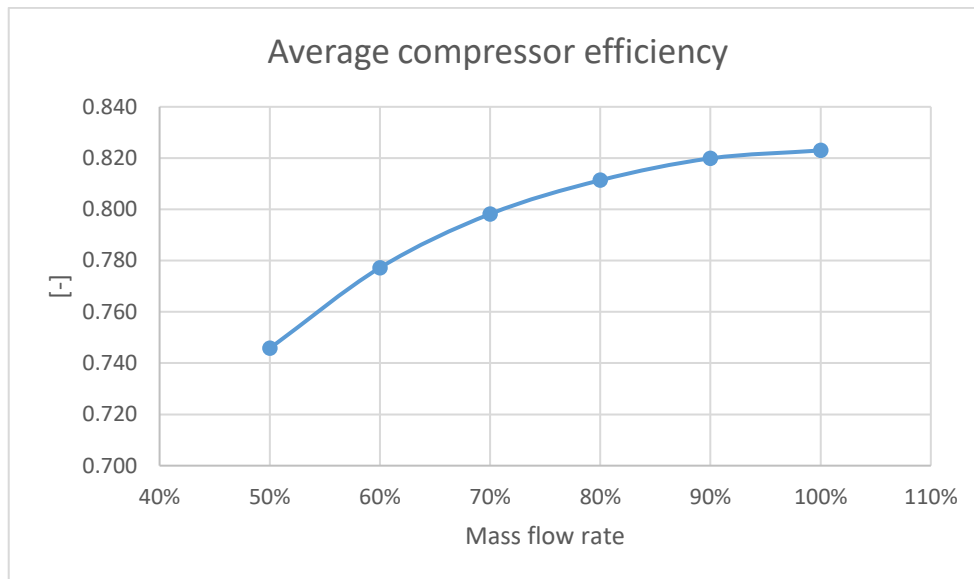


Figure 5.21 – Average compressor efficiency in off-design operation.

5.4.1 Control Variables and Stage Analysis

The off-design regulation of the machine is executed working on three variables: the two VIGV at the inlet of both shafts and the rotational speed of the electric motor. The optimization of the whole machine is accomplished by the code, as described in the section 4.2. In the present sub-section, the results are displayed and discussed.

The VIGV angles α_{ob} chosen by the code for the stage 1 and for the stage 4 are shown respectively in Figure 5.22 and Figure 5.23. The regulation in rotational speed for the low-pressure shaft and the high-pressure shaft are shown respectively in Figure 5.24 and Figure 5.25. For the graphs regarding the rotational speed, it must be noticed that the RPM interval displayed is narrow and the scale should not deceive the reader: the rotational speed variation throughout the whole off-design regulation is small. In the stage 1 the mass flow rate is half of the one of the other stages because of the parallel configuration.

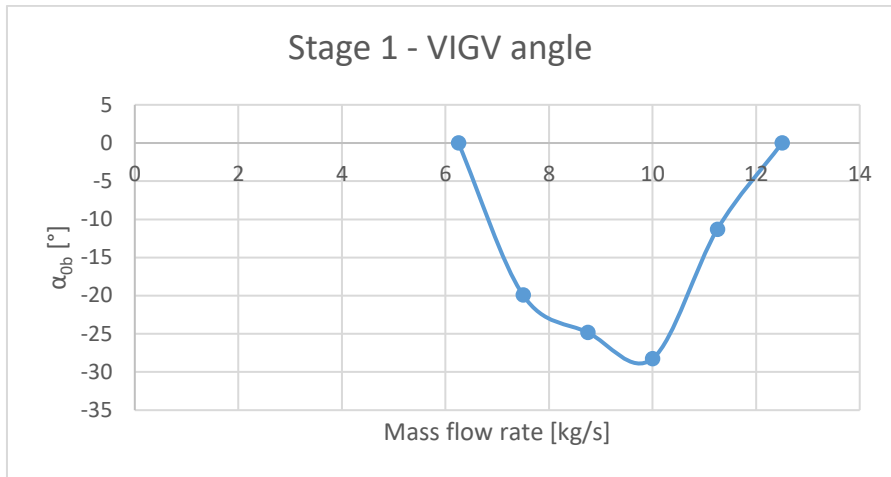


Figure 5.22 – VIGV off-design regulation for stage 1.

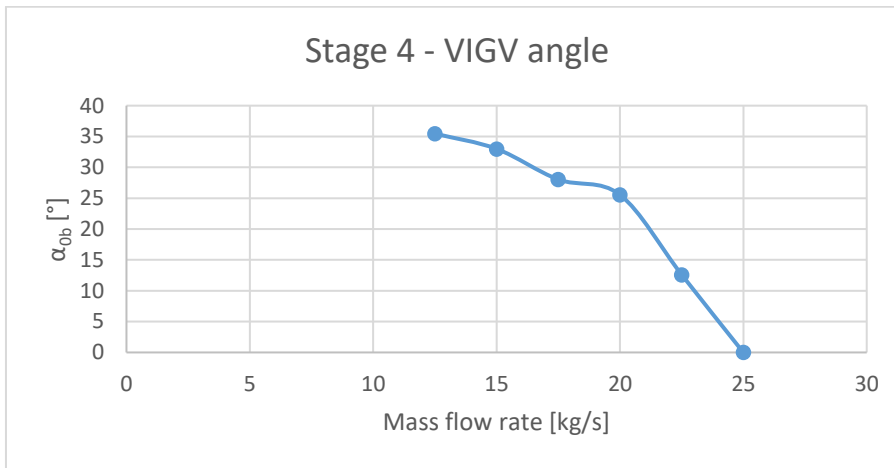


Figure 5.23 – VIGV off-design regulation for stage 4.

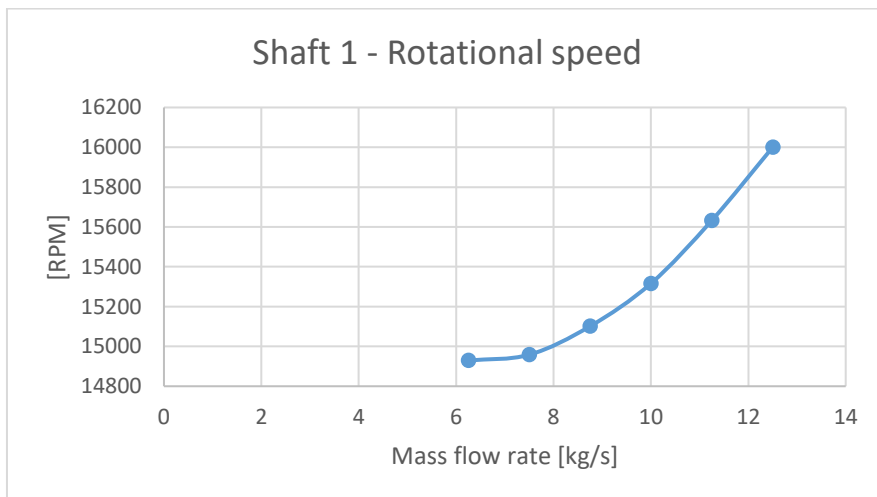


Figure 5.24 – Rotational speed off-design regulation for the low-pressure shaft.

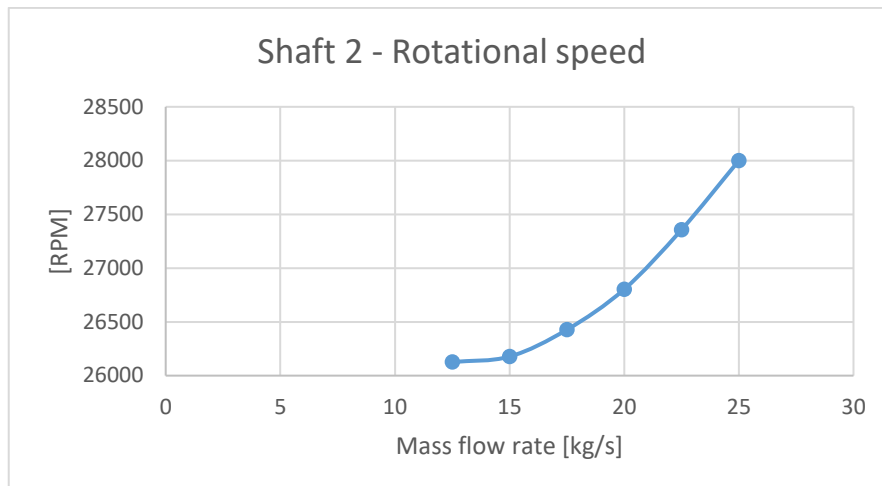


Figure 5.25 – Rotational speed off-design regulation for the high-pressure shaft.

The VIGV of the stage 1 works with a negative angle to load more the first stage. This approach is explained in the sub-section 4.2.3. It can be noticed that reducing the mass flow rate close to the design point, the VIGV angle decreases steeply. This happens because the stage 1 can handle the increase in load. This steep load increase, together with a still good average efficiency (Figure 5.21), allows to have an almost constant temperature exiting the compressor for a mass flow rate higher than 80% of the nominal one (Figure 5.18).

However, when the mass flow rate is reduced too much, the VIGV angle must increase and it returns to be almost completely open (with α_{0b} almost null) at a mass flow rate of 50%. This happens to avoid the stall of the stage 1. In fact, if the VIGV angle did not increase for a mass flow rate lower than 80%, the stage 1 would not tolerate the excessive load. This high load is caused by the simultaneous effect of the negative VIGV angle and the normal tendency of a centrifugal compressor with a negative β_2 angle to increase its compression ratio with a decrease in mass flow rate.

The load increase on the stage 1 and the drop in efficiency at low flow rates explain why the thermal power dissipated by the intercooler is more than proportional to the mass flow rate (Figure 5.19).

In the end, the VIGV of the stage 1 increases the load when it is possible to exploit the intercooler and to compensate for the increase in the outlet temperature due to the reduction in efficiency.

The VIGV of the stage 4 reduces the load on that stage. It counterbalances the increase in incidence angle on the impeller inlet caused by the reduction in mass flow rate imposing a positive $\alpha_{0,b}$.

The rotational speed of the two shafts is always linked by the design gear ratio because they are connected to the same gearbox. So, the graphs in Figure 5.24 and Figure 5.25 have the same exact shape. The rotational speed decreases following quite closely a parabolic trend.

The results relative to each stage are shown in the following graphs. The compression ratio and the efficiency are respectively shown in Figure 5.26 and Figure 5.27.

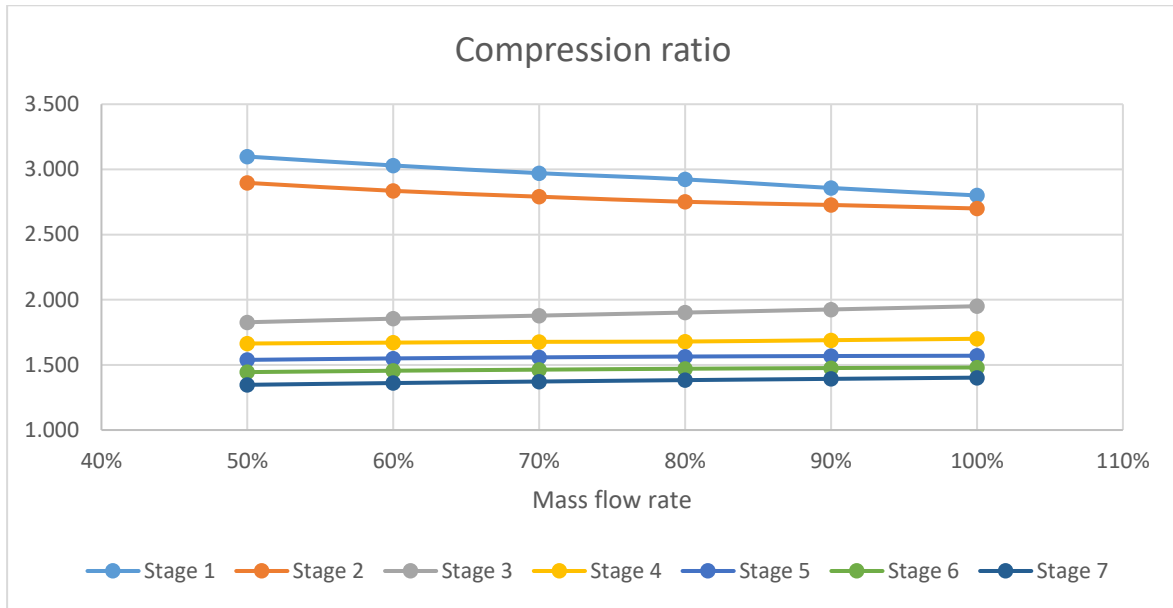


Figure 5.26 – Compression ratio for each stage in off-design operation.

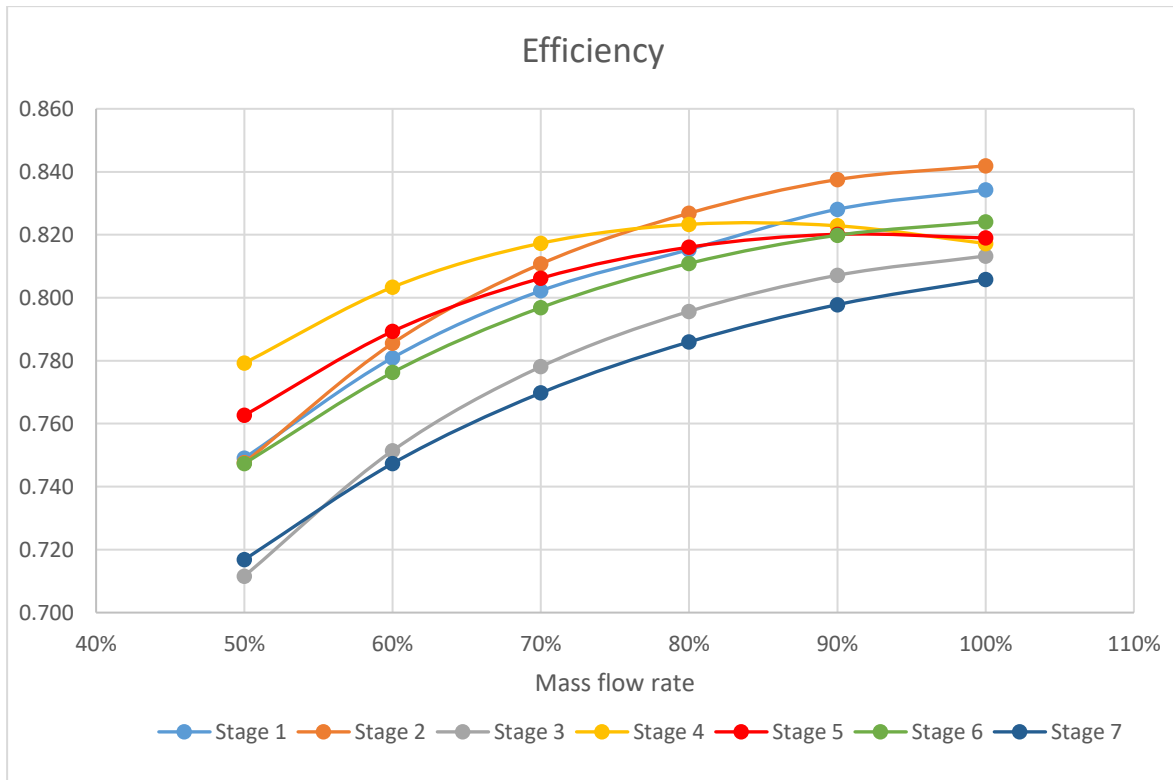


Figure 5.27 – Efficiency $\eta_{is,ss}$ for each stage in off-design operation.

As the mass flow rate decreases, the compression ratio of some stages increases and the one of other stages decreases, so that the whole compression ratio remains constant. In particular, the compression ratio of the stages 1 and 2 increases and the one of all the other stages decreases as the mass flow rate decreases, as shown in Figure 5.26. As already discussed, the VIGV of stage 1 increases the load and the VIGV of stage 4 reduces it. This effect propagates on the stages that follow the VIGV, so the compression ratio of the stage 2, 5, 6 and 7 follows the trend imposed by the upstream VIGV. However, it is not possible to establish with a theoretical approach a priori how the compression ratio of each stage evolves because both the VIGV angle and the rotational speed are involved.

In general, the efficiency of the stages decreases as the mass flow rate decreases because the optimal operating point is the design one and the farther a turbomachine operates from it, the more its performances are damaged. However, in the stage 4 and 5, close to the design point, the efficiency increases as the mass flow rate is reduced. This is an effect of the VIGV angle that reduces the load on these stages.

5.4.2 Loss Mechanisms

The values for every type of loss in every stage for every operating condition are reported from Figure 5.28 to Figure 5.34.

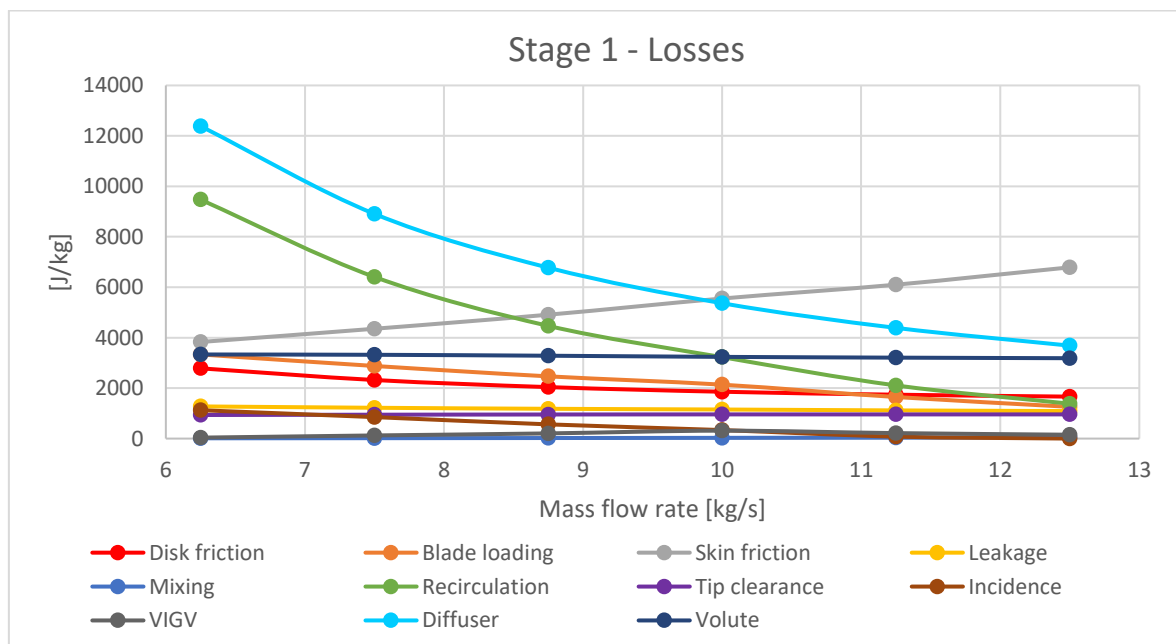


Figure 5.28 – Loss distribution for stage 1 in off-design operation.

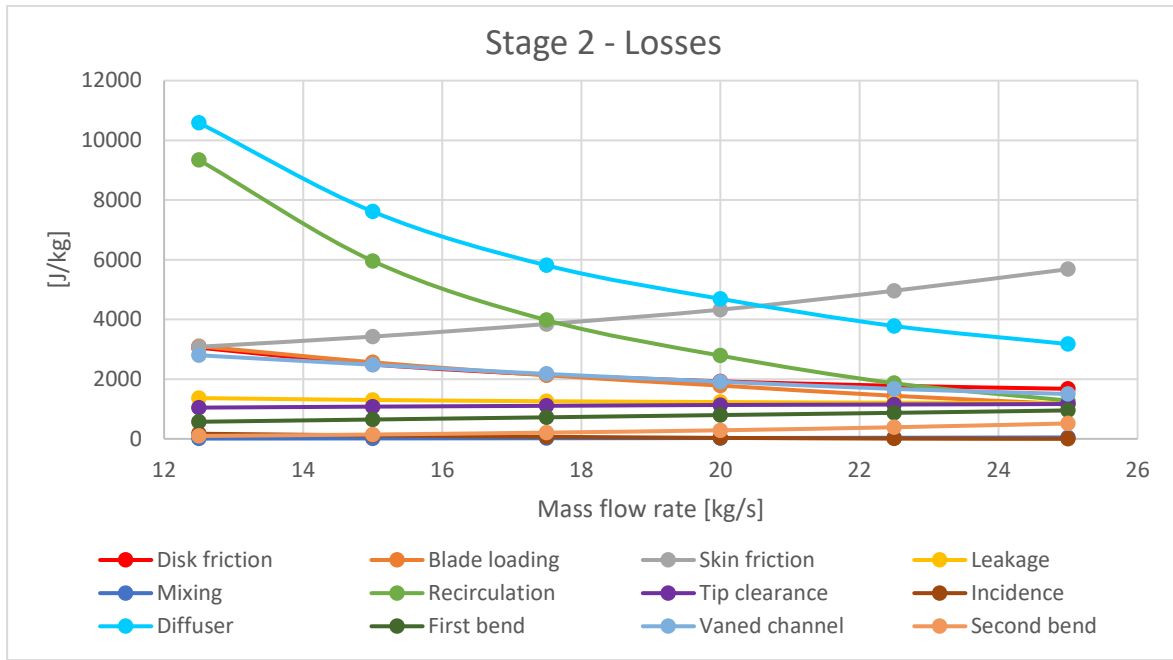


Figure 5.29 – Loss distribution for stage 2 in off-design operation.

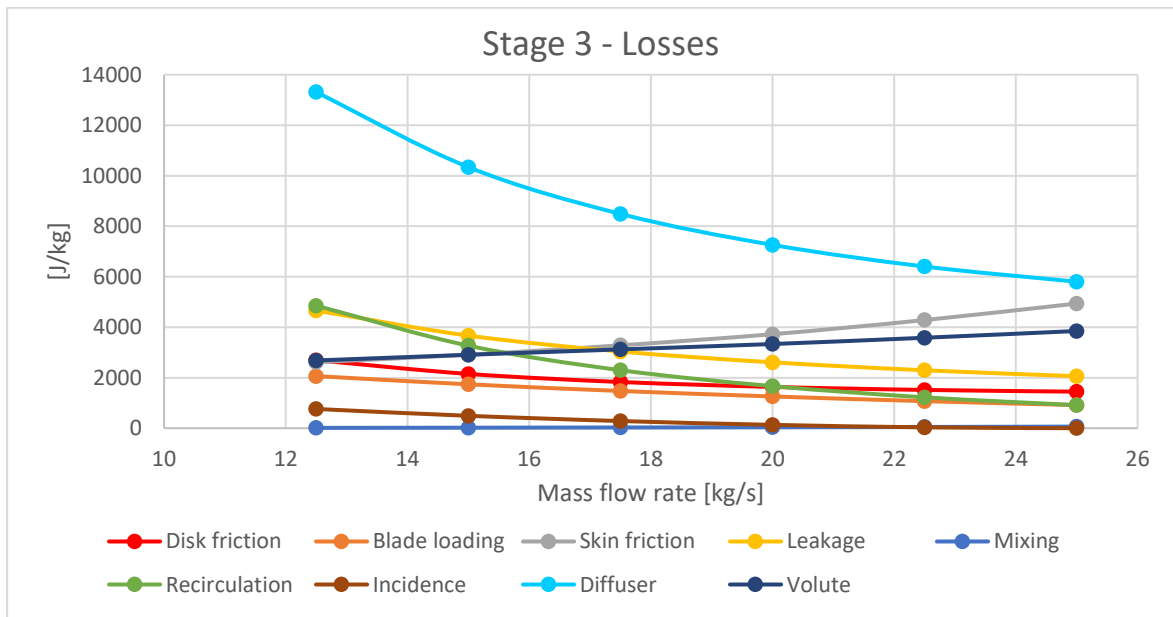


Figure 5.30 – Loss distribution for stage 3 in off-design operation.

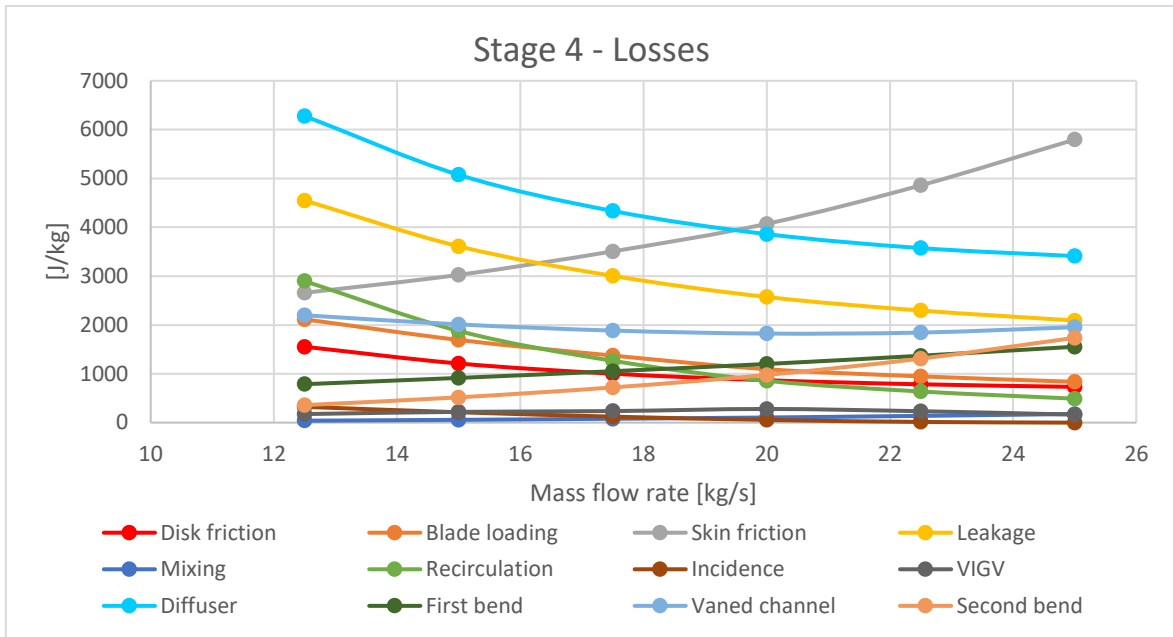


Figure 5.31 – Loss distribution for stage 4 in off-design operation.

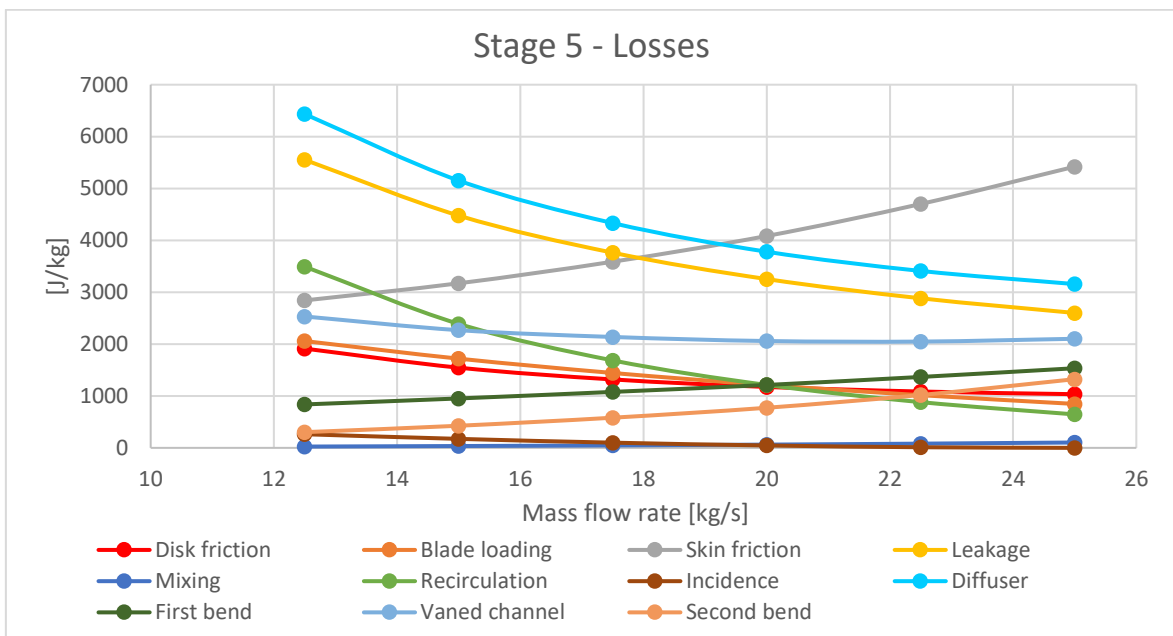


Figure 5.32 – Loss distribution for stage 5 in off-design operation.

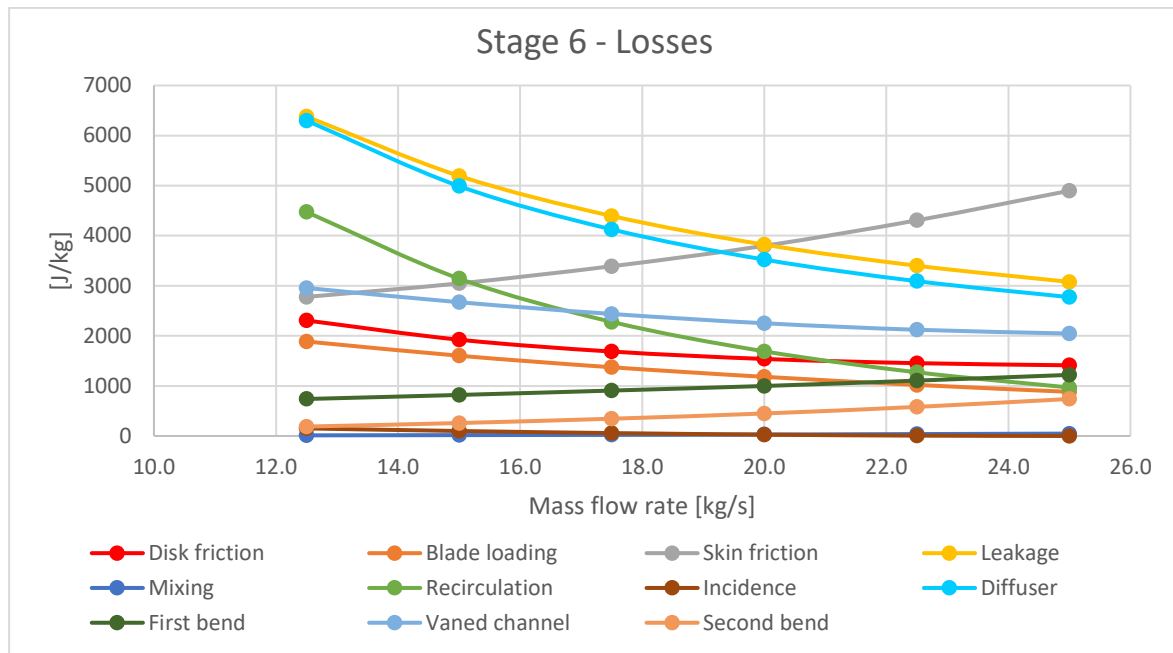


Figure 5.33 – Loss distribution for stage 6 in off-design operation.

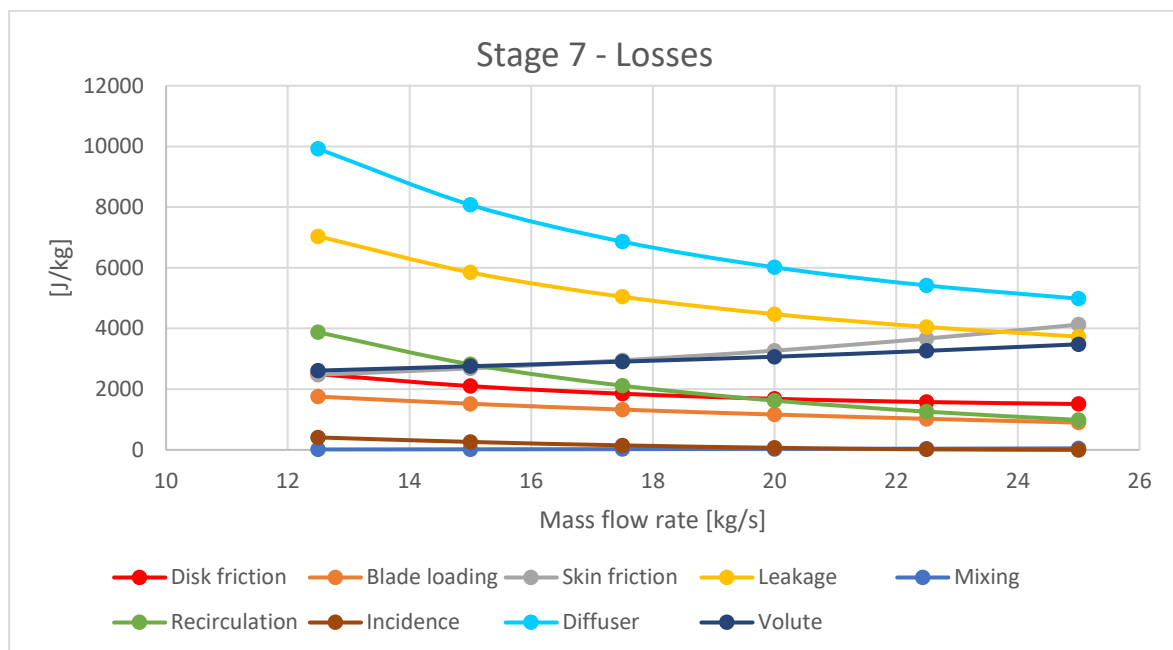


Figure 5.34 – Loss distribution for stage 7 in off-design operation.

The skin friction loss decreases in all the stages as the mass flow rate decreases because the average flow velocity in the machine is lower if the flow rate and the rotational speed are lower. With a lower flow velocity, the losses due to fluid friction inside the impeller are reduced.

The recirculation loss and the vaneless diffuser loss, instead, always increase as the mass flow rate decreases. In fact, as the mass flow rate decreases, the impeller outlet angle α_2 increases (the outlet flow becomes more tangential), as shown in Figure 5.35. This causes

the recirculation of a higher portion of the flow back into the impeller (higher recirculation loss) and a longer flow path inside the diffuser (higher friction loss in the diffuser).

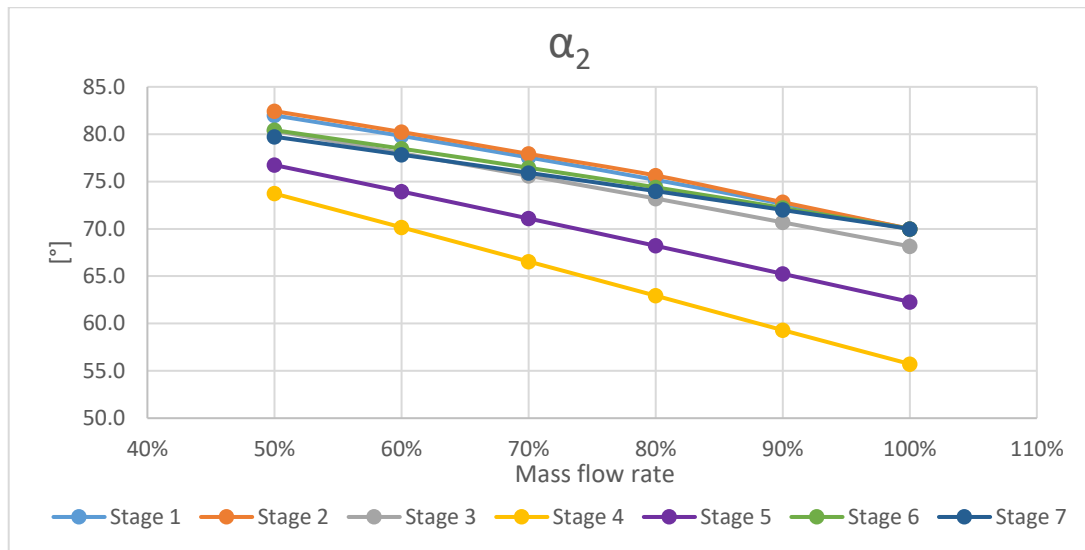


Figure 5.35 – Impeller outlet absolute flow angle for each stage in off-design operation.

The leakage loss always increases as the mass flow rate decreases. This happens because the compression ratio of the stages does not change drastically, so the mass flow rate that leaks between the outlet and the inlet of the impeller remains approximately the same as the design one. However, its impact on the performances of the stages increases because the overall mass flow rate is smaller, so the percentage that leaks is higher. As discussed in 5.2.2, the leakage loss is more important for the last stages because they are smaller.

5.4.3 Stall analysis

To verify that the stall phenomenon does not happen in any stage, the De Haller parameter is displayed in Figure 5.36. The De Haller parameter relative to the stage 1 decreases steeply between 100% and 80% of the design mass flow rate and it has a flatter shape for lower mass flow rates. The opposite happens for the De Haller parameter of the stage 4. Both trends are justified by the VIGV angles and their consequent effect on the load of the following stages, which are described in the sub-section 5.4.1. In fact, the De Haller parameter has a steeper decrease the more the stage load is increased.

For values of the De Haller parameter higher than 0.6, the working condition should not present any stall. In Figure 5.36 it can be noticed that the only stage that always respect this constraint is the last one. Between 60% and 50% of the design mass flow rate, most of the stages do not respect the constraint, so a stall could happen. The design value of the De Haller parameter is 0.8 for all the stages, as shown in Figure 5.36.

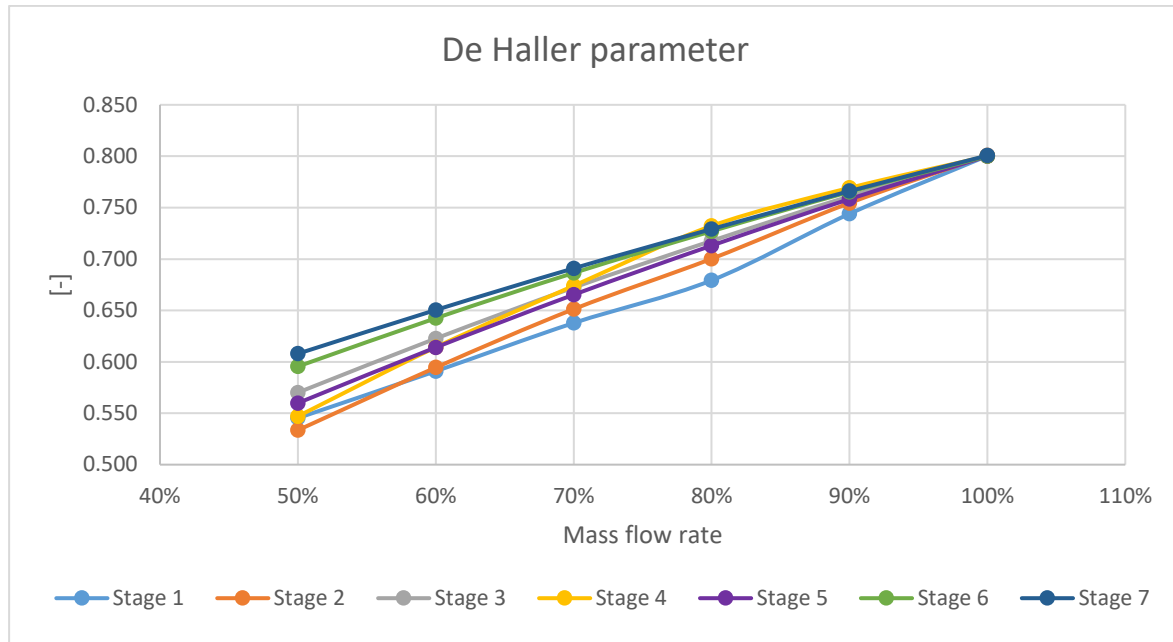


Figure 5.36 – De Haller parameter for each stage in off-design operation.

A solution to this problem is to work always above 60% of the design mass rate. However, if each of the four compression trains of the CAES plant can work between 50% and 100% of the design power (which is equal to 18.761 MW), the entire plant can operate with any power between 12.5% (50% of the design power of one compression train is equivalent to 12.5% of the nominal compression power of the whole plant) and 100% of the nominal one. In fact, it would be possible to regulate continuously the plant turning on and off an appropriate number of parallel trains and any possible power value between 12.5% and 100% could be absorbed regulating the machines in off-design operation. The problem is that to reach 50% of the design power of one train it is necessary to work with a mass flow rate even lower than 50%. Looking at Figure 5.20, it can be approximately extrapolated that a value of around 40% of the design mass flow rate would be needed.

To still have the ability of continuously regulating the plant even without reaching 50% of the design power, it is possible to increase the power of each train above 100%. This analysis is not accomplished in the present work.

5.5 Drivetrain

In this section it is proposed a design for the mechanical and electrical part of the machine. The first aspect to consider when choosing the electrical system is that the compressor needs to have good performances in off-design conditions. To guarantee this, a variable-frequency drive (VFD) needs to be used. A VFD is an inverter that regulates the output frequency of the electricity with a constant input frequency. The regulation of the electrical frequency allows to precisely control the rotational speed of the motor and so the rotational speed of the shafts.

Then, it is important to consider the power requested by the compression system and the rotational speeds of the two shafts of the compressor. In this case, each compression train (there are four compression trains in parallel) is designed to consume 18.761 MW and the two shafts are designed to rotate at 16000 RPM and 28000 RPM.

Assuming a mechanical efficiency (that considers the gearbox loss, the bearings loss and all the other mechanical losses) of 0.95, the design power output requested to the motor is 19.748 MW. So, the electrical machines are selected with a nominal power indicated by the datasheet slightly above 20 MW.

An induction motor is chosen to transform the electric power into mechanical power because it is cheaper than a synchronous motor and it does not presents any problem to regulate its rotational speed close to the design value, which is what is requested by the present scenario.

Since a solution with two shafts has been selected, for the mechanical system is proposed to use an integrally geared compressor (IGC). This solution allows to drive a large low-speed bull gear through the electrical motor and to connect both compressor shafts to it using two high-speed pinions [39]. In this way, the two shafts are mechanically connected in parallel, but from the fluid dynamic prospective they are in series. Moreover, the two shafts can be designed to rotate at any requested rotational speed just by changing the dimension of the two pinion and the one of the bull gear, linking the electric motor rotational speed to the compressor's one with any reasonable gear ratio. A picture showing the mechanical connection between a pinion and the bull gear is reported in Figure 5.37. The whole concept proposed is illustrated in Figure 5.38.

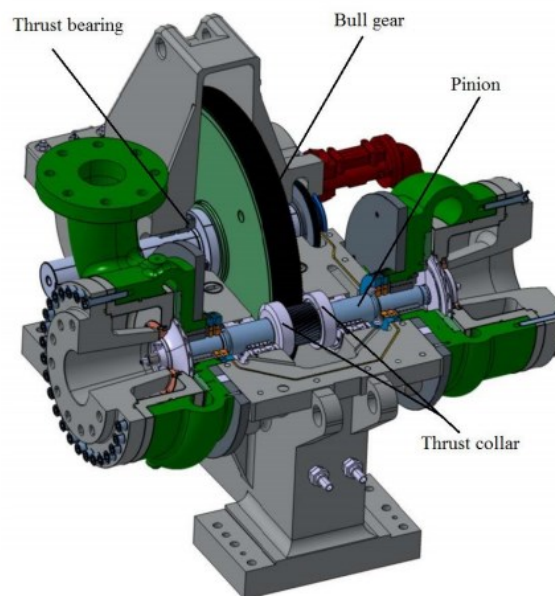


Figure 5.37 – Example of a mechanical system for an IGC. Usually, more than one pinion is connected [39].



Figure 5.38 – Conceptual scheme of the electrical and mechanical system.

An alternative to a geared configuration is a direct-drive solution. This solution is based on the direct connection of the electric motor with the shaft of the compressor, without any gearbox. It has a lot of advantages in terms of maintenance costs, efficiency, emissions and unmanned operations [40]. However, this approach is rejected in the present work for multiple reasons. First, the presence of two shafts implies that a gearbox is needed anyway to have two different rotational speeds, so the advantages of the direct-drive configuration are almost completely cancelled. Then, it is very difficult to find a 20 MW electric motor able to rotate at 16000 RPM, as illustrated in Figure 5.39. This figure shows four different types of induction motor, represented by the vertical lines. The top of these vertical lines represents the most powerful motor running at that speed. Then, it is assumed that this motor is at least able to produce a constant torque at reduced speed. The oblique lines are generated with this assumption [40], so they are just a conservative interpolation and they are not related to real machines.

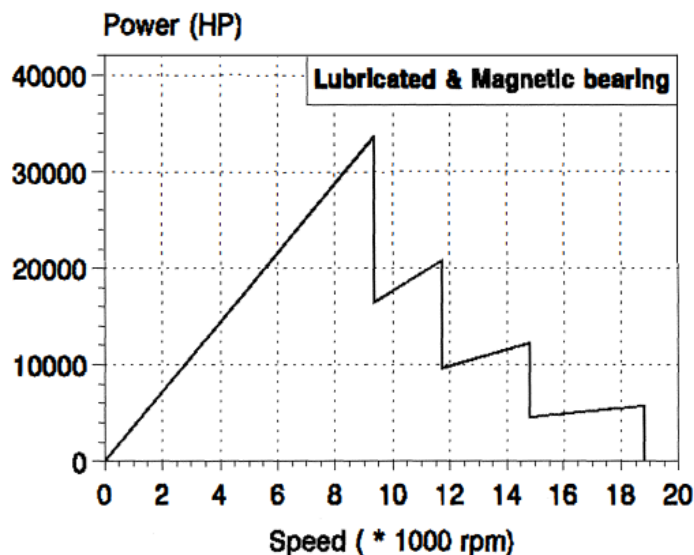


Figure 5.39 – High speed induction motor capability curve (10000 HP = 7.46 MW). The vertical lines represent four different rotor sizes, the oblique lines are just conservative interpolations [40].

The specific machines and their datasheets are now proposed for the VFD and for the induction motor and their choices are justified. In fact, the selection of these two components

is the most delicate one and it can be done for a generic situation. An appropriate selection for the transformer or for the gearbox of the IGC is very case dependent and these components are usually custom made.

The proposed VFD is the “ACS5000” produced by ABB [41]. It is selected the model “ACS5000-069-W03A-E6-010” because it has a power rating of 20.380 MW, which is very appropriate for the present work. The general datasheet and the one specific to that model are reported, respectively, in Figure 5.40 and Figure 5.41.

Input	
Input configuration	36-pulse diode rectifier. Optionally 18-pulse for frames 1 and 2 for liquid-cooled ACS5000.
Input voltage	Input to diode rectifier: 1920 to 1980 V, 3700 to 3960 V Input to integrated transformer: 4.16 to 13.8 kV
Input voltage variation	±10% without derating +20%/-30% with derating
Input frequency	50/60 Hz
Input frequency variation	<5%
Input power factor	>0.96
Input harmonics	IEC 61000-2-4 and IEEE 519 compliant
Auxiliary voltage	Control (optional): 110 V DC, 220 V DC or 110 to 240 V AC 50/60 Hz Auxiliary: 380 to 480 V AC 50/60 Hz, 3-phase 500 to 690 V AC 50/60 Hz, 3-phase (for liquid-cooled only)
Output	
Output power	2000 to 36000 kW (higher on request)
Output voltage	6.0 to 6.9 kV (4.0 to 4.16 kV with derating)
Output frequency	0 to 250 Hz
Motor type	Induction, synchronous and permanent magnet
Efficiency of converter	>98.5%
Mechanical	
Enclosure	Standard air-cooled: IP21 Standard liquid-cooled: IP42 Optional air-cooled: IP42 Optional liquid-cooled: IP54
Cable entry	Top/bottom
Environmental	
Altitude	2000 m.a.s.l. (higher with derating)
Ambient air temperature	+1 to +40 °C (lower and higher with derating)
External cooling liquid temperature	+5 to +32 °C (lower and higher with derating)
Noise	Liquid-cooled: ≤75 dB(A) Air-cooled: ≤85 dB(A)
Cooling type	Air, liquid
Standards	EN, IEC, CE, (optional CSA)

Figure 5.40 – Technical data about the ACS5000 drives produced by ABB [41].

Motor data			Type code	Converter data				
Nominal ratings				Power (kVA)	With external transformer		With combined transformer	
(kW)	(hp)	(A)			Length (mm)	Weight (kg)	Length (mm)	Weight (kg)
6900 V								
20380	27310	1750	ACS5000-069-W03A-E6-010	20900	13430	12200	n.a.	n.a.

Figure 5.41 – Technical data specific for the model ACS5000-069-W03A-E6-010 [41].

It can be noticed that the maximum outlet frequency of this family of inverters is 250 Hz, which corresponds to 15000 RPM. However, this is not a problem since, as already said, an induction motor rated for 20 MW cannot rotate at that speed anyway. For the specific model chosen, the transformer is not combined with the VFD, so an external transformer needs to be used.

The proposed induction motor is the model “MV Motors TM21-G” produced by TMEIC (Toshiba Mitsubishi-Electric Industrial Systems Corporation, a joint venture between Toshiba and Mitsubishi Electric) [42]. Its datasheet is reported in Figure 5.42. The power of 23 MW is appropriate for the present work.


Product	MV Motors TM21-G
Typical View	
Power	Up to 23,000 kW (30,800 hp)
Speed	Up to 3,600 rpm
Voltage	2 – 11 kV
Enclosure	Weather Protected B-WPIWP24W Totally Enclosed Air-to-Air-Cooled – TEAAC/IP54/IP55/IP56 Totally Enclosed Water-to-Air-Cooled – TEWAC/IP54/IP55/IP56
Classified Area	Exn, Exe, Exp
Rotor	Copper rotor bars
Bearing Options	Ball & roller bearings, grease lubrication Sleeve bearings
Available Standards	IEC, NEMA, BS, AS, CSA, IS, JEC
Major App.	Fans, Blowers, Compressors, Mills, Conveyors

Figure 5.42 – Technical data about the MV Motors TM21-G induction motor produced by TMEIC [42].

The maximum rotational speed of this induction motor is 3600 RPM. So, the VFD is set to produce an outlet electric frequency of maximum 60 Hz (during design operation), which is equivalent to 3600 RPM.

Chapter 6

Conclusions

The solution proposed in the present work is a preliminary design of a multistage centrifugal compressor employed in an A-CAES plant. The off-design operation is evaluated for a wide mass flow rate domain (between 50% and 100% of the nominal mass flow rate). The drivetrain is analysed and a combination of electric machines specific for the compressor designed is proposed.

The computational procedure guarantees a significant amount of detail, considering that it is a 0D method. All the points of the stage are evaluated from the thermodynamic and fluid dynamic point of view and very few assumptions are made on these subjects. The geometry contains more simplifications, especially for the return channel, because in a preliminary design it is requested to work on a general machine and some geometric details are very case-dependent. To proceed with a definitive design, a study based on a CFD code or on experimental results is suggested.

The isobaric specific heat c_p and the dynamic viscosity μ are evaluated in function of the temperature at the inlet of each stage. This is very important for a compressor employed in an A-CAES plant because the temperature reaches high values, so c_p and μ are considerably different than the ones evaluated at ambient temperature.

An original set of loss correlations is built, combining the work of different authors and converting all the losses into specific enthalpy changes to achieve a homogeneous set of losses. In this way, a comparison between them is easy and immediate and it is possible to instantly understand which is the most important aspect to be improved. All the components of a centrifugal stage are analysed and their loss correlation are combined to evaluate the overall performances.

The MATLAB code written to study the compressor is very flexible and it can be used to study any type of subsonic centrifugal compressor of any size. Both the covered and the uncovered impeller are analysed with their specific loss mechanisms. The design of the stage is an optimization process able to change 8 design variables and to find the combination that results in the maximum possible efficiency. The design variables are selected to be directly linked to the design criteria, so that it is easy to evaluate their upper and lower bounds, which are necessary to lead the optimization method into a physically viable design. The constraints on the results are necessary to design a reliable and flexible machine, which is consistent

from the mechanical and geometrical point of view. The torque applied to the shaft is evaluated and its mechanical integrity is checked.

The off-design analysis reveals that the compressor could have problems at mass flow rates lower than 60% of the design one. To guarantee that the plant is able to work continuously without any gap in the power absorption, it is suggested to improve the performances in this operating region. In fact, if each compressor train can work between 50% and 100% of its design power (which is equal to 18.761 MW), the plant can absorb any amount of power between 12.5% and 100% of the nominal one (since there are four parallel trains). The operation of the compressor at 50% of the design power corresponds at roughly 40% of the design mass flow rate, executing an approximate extrapolation in Figure 5.20. Moreover, the average efficiency of the stages drops of almost 8% between the design condition and the operating point with 50% of the design mass flow rate, as shown in Figure 5.21. In the end, an improvement on the off-design conditions is important to allow the plant to regulate continuously without any stall issues or big efficiency drops.

If the low mass flow rate region cannot be improved enough, another solution is to design the stages to work with a lower mass flow rate than the one needed to absorb the nominal power of the plant. Doing so, the off-design regulation implies to work both at a power lower and higher than the design one. So, the optimum operating point of the machine is achieved at an intermediate mass flow rate. For example, if the design of the stages is executed at 70% of the mass flow rate needed to consume the nominal power of the plant, the off-design regulation requires to move from 70% to 40% and from 70% to 100% (approximately). This reduces the distance between the mass flow rate in the design point and the minimum one, but the compressor works in off-design conditions also in the high mass flow rate region. In any case, a study on the mass flow rate higher than the design one is necessary to apply this solution because new issues could arise.

The creep phenomenon must be considered for the last stages that work at the highest temperature, both in design conditions and at low mass flow rates. The fact that the rotational velocity decreases at low mass flow rates is not enough to guarantee that the creep phenomenon does not generate problems when the outlet temperature increases.

The heat exchangers must be designed to handle a variable outlet temperature and a variable mass flow rate while maintaining the molten salts temperature almost constant. The molten salts works at the highest possible temperature in design conditions, so an increase in its temperature cannot be sustained.

The pressure losses inside the pipeline that connects the compressor outlet to the CAS (placed on the seabed) depend on the mass flow rate. They must be considered to impose the compressor outlet pressure during off-design operation.

6.1 Future Improvements

In this section some suggestions are proposed to improve the present work.

- **Splitter blades** – An improvement on the impeller performances can be achieved adding the splitter blades. They are partial-length blades between the adjacent full blades. Their purpose is to maintain an acceptable blade solidity while reducing the blade metal blockage at the minimum passage area (throat). In fact, they are especially used in compressor with high Mach numbers to provide a larger throat area. Doing so, a higher mass flow rate can pass through the impeller before a sonic condition occurs [10].
- **Variable vaned diffuser** – In the present work, stages equipped with a vaneless diffuser are chosen. The vaneless diffuser is less efficient than the vaned one, but it allows to improve the off-design performances. Since in a CAES plant the off-design operation is a key aspect, the design efficiency is sacrificed for a higher flexibility. However, there is the possibility of achieving both targets introducing a variable vaned diffuser. This solution allows to increase the working range of the machine compared to a classical vaned diffuser. In addition, the combination of simultaneous adjustment of the VIGV and of the diffuser vanes enables an increase in machine efficiency over the entire operating range, compared with regulation using only the VIGV or only the variable diffuser vanes [14]. This solution could allow to avoid the stall during the operation below 60% of the design mass flow rate and to improve the performances of the entire off-design domain.
- **Pre-swirl in design operation** – It can be interesting to analyse the optimization of the VIGV angle also during the design of the stage. A pre-swirl at the design point can result in a better efficiency of the stage, but a careful analysis on the impact that this solution has on the off-design regulation is necessary.
- **Variable c_p and μ along the stage compression** – A more accurate computational procedure can be achieved if the values of c_p and μ are not constant during the compression process of each stage. However, a faster optimization method or a faster machine is suggested to accomplish this task because the computational cost would increase significantly. Even maintaining these two quantities fixed during the stage compression, it takes up to 2500 seconds to design each stage and up to 1500 seconds for each off-design evaluation with the present processor, so a further increase in the computational time should be carefully assessed.
- **Different optimization method** – In the present work, the *patternsearch* method and the *fmincon* method are used, respectively, for the design and for the off-design analysis. The *fmincon* method is faster, but it is more likely to result in a local minimum. However, also the *patternsearch* method can suffer from this problem,

even if it is less likely. If the local minima problem cannot be accepted and the computational cost is not a big issue, the genetic algorithm *ga* or the *particleswarm* methods can be a solution. They are methods that take more function evaluations (especially *ga*) and they are less likely to have problems of local minima. They are stochastic methods, so their results change with every run [12].

Bibliography

- [1] "Renewables 2020 - Analysis and forecast to 2025," International Energy Agency, [Online]. Available: <https://www.iea.org/reports/renewables-2020/renewable-electricity-2#abstract>. [Accessed 02 2021].
- [2] J. Wang, K. Lu, L. Ma, J. Wang, M. Dooner, S. Miao, J. Li and D. Wang, "Overview of Compressed Air Energy Storage and Technology Development," *Energies*, 2017.
- [3] M. Budt, D. Wolf, R. Span and J. Yan, "A review on compressed air energy storage: Basic principles, past milestones and recent developments," *Elsevier*, 2016.
- [4] M. Belloli and A. Hirn, "Underwater Compressed Air Energy Storage (CAES): system design optimization, economics and simulation," Master's Thesis, 2018.
- [5] K. H. Lüdtke, *Process Centrifugal Compressors: Basics, Function, Operation, Design, Application*, Springer, 2004.
- [6] K. Brun and R. Kurz, *Compression Machinery for Oil and Gas*, Gulf Professional Publishing, 2019.
- [7] M. Coppinger and E. Swain, "Performance prediction of an industrial centrifugal compressor inlet guide vane system," *Journal of Mechanical Engineering Science*, 1999.
- [8] A. Whitfield and N. Baines, *Design of radial turbomachines*, Longman, 1990.
- [9] H. W. Oh, E. S. Yoon and M. K. Chung, "An optimum set of loss models for performance prediction of centrifugal compressors," *Journal of Power and Energy*, 1997.
- [10] R. H. Aungier, *Centrifugal Compressors: A Strategy for Aerodynamic Design and Analysis*, ASME Press, 2000.
- [11] C. Osnaghi, *Teoria delle Turbomacchine*, Esculapio Editore, 2020.
- [12] MATLAB, "MathWorks," [Online]. Available: <https://it.mathworks.com/>. [Accessed February 2021].
- [13] E. A. Baskharone, *Principles of turbomachinery in air-breathing engines*, Cambridge, 2006.

- [14] H. Simon, T. Wallmann and T. Monk, "Improvements in Performance Characteristics of Single-Stage and Multistage Centrifugal Compressors by Simultaneous Adjustments of Inlet Guide Vanes and Diffuser Vanes," *ASME*, 1987.
- [15] J. Houghton, *Global Warming*, Cambridge, 2004.
- [16] W. He, X. Luo, D. Evans, J. Busby, S. Garvey, D. Parkes and J. Wang, "Exergy storage of compressed air in cavern and cavern volume estimation of the large-scale compressed air energy storage system," *Elsevier*, 2017.
- [17] Y. Kim, J. Lee, S. Kim and D. Favrat, "Potential and Evolution of Compressed Air Energy Storage: Energy and Exergy Analyses," *Entropy*, 2012.
- [18] C. Jakiel, S. Zunft and A. Nowi, "Adiabatic compressed air energy storage plants for efficient peak load power supply from wind energy: the European project AA-CAES," *International Journal of Energy Technology and Policy*, 2007.
- [19] S. Zunft, V. Dreissigacker, M. Bieber, A. Banach, C. Klabunde and O. Warweg, "Electricity storage with adiabatic compressed air energy storage: Results of the BMWi-project ADELE-ING," *International ETG Congress 2017*, 2017.
- [20] V. C. Patil and P. I. Ro, "Energy and Exergy Analysis of Ocean Compressed Air Energy Storage Concepts," *Journal of Engineering*, 2017.
- [21] K. Deng, K. Zhang, X. Xue and H. Zhou, "Design of a New Compressed Air Energy Storage System with Constant Gas Pressure and Temperature for Application in Coal Mine Roadways," *Energies*, 2019.
- [22] B. E. Poling, J. M. Prausnitz and J. P. O'Connell, *The Properties of Gases and Liquids*, McGraw-Hill, 2001.
- [23] W. Sutherland, "LII. The viscosity of gases and molecular force," *Philosophical Magazine*, 1893.
- [24] R. I. Lewis, *Turbomachinery Performance Analysis*, Elsevier Science & Technology Books, 1996.
- [25] H. K. Versteeg and W. Malalasekera, *An Introduction to Computational Fluid Dynamics: The Finite Volume Method*, Pearson, 2007.
- [26] F. J. Wiesner, "A Review of Slip Factors for Centrifugal Impellers," *ASME*, 1967.
- [27] S. Parisi, "Modeling and simulation of a centrifugal compressor for automotive fuel cell applications," Master's Thesis, 2020.
- [28] J. v. Baten, "AmsterCHEM - ScanIt," [Online]. Available: <https://www.amsterchem.com/scanit.html>.

-
- [29] P. M. Came, "The Current State of Research and Design in High Pressure Ratio Centrifugal Compressors," 1977.
- [30] E. I. G. Velásquez, "Determination of a suitable set of loss models for centrifugal compressor performance prediction," *Chinese Journal of Aeronautics*, 2016.
- [31] W. Jansen, "A method for calculating the flow in a centrifugal impeller when entropy gradients are present," *Inst. Mech. Eng. Internal Aerodynamics*, 1967.
- [32] C. F. Colebrook, "Turbulent Flow in Pipes, with particular reference to the Transition Region between the Smooth and Rough Pipe Laws," *Journal of the Institution of Civil Engineers*, 1939.
- [33] J. P. Johnston and R. C. Dean, "Losses in Vaneless Diffusers of Centrifugal Compressors and Pumps - Analysis, Experiment, and Design," *ASME*, 1966.
- [34] V. De Bellis, "Simulazione monodimensionale stazionaria e non stazionaria di turbocompressori per la sovralimentazione di MCI," PhD Thesis.
- [35] B. Eckert and E. Schnell, *Axial- und Radialkompressoren*, Springer Verlag, 1961.
- [36] G. Persico, P. Gaetani, A. Romei, L. Toni, E. F. Bellobuono and R. Valente, "Implications of Phase Change on the Aerodynamics of Centrifugal Compressors for Supercritical Carbon Dioxide Applications," *Journal of Engineering for Gas Turbines and Power*, 2021.
- [37] P. Davoli, L. Vergani and S. Beretta, *Costruzioni di macchine 1*, McGraw-Hill, 2017.
- [38] "EuroSiderScalo," [Online]. Available: <https://eurosiderscalo.com/39nicrmo3/>. [Accessed 02 2021].
- [39] K. Wygant, J. Bygrave, W. Bosen and R. Pelton, "Tutorial on the application and design of integrally geared compressors," 2016.
- [40] D. C. Gilon and L. Boutriau, "Experience with high speed induction motors for direct driving of compressors," 1998.
- [41] "Datasheet ACS5000," ABB, [Online]. Available: <https://new.abb.com/drives/medium-voltage-ac-drives/acs5000>. [Accessed 02 2021].
- [42] "Datasheet MV Motors TM21-G," TMEIC, [Online]. Available: <https://www.tmeic.com/sites/default/files/assets/files/library/TMEIC%20Motor%20Overview%20P0023-June2019-web.pdf>. [Accessed 02 2021].